



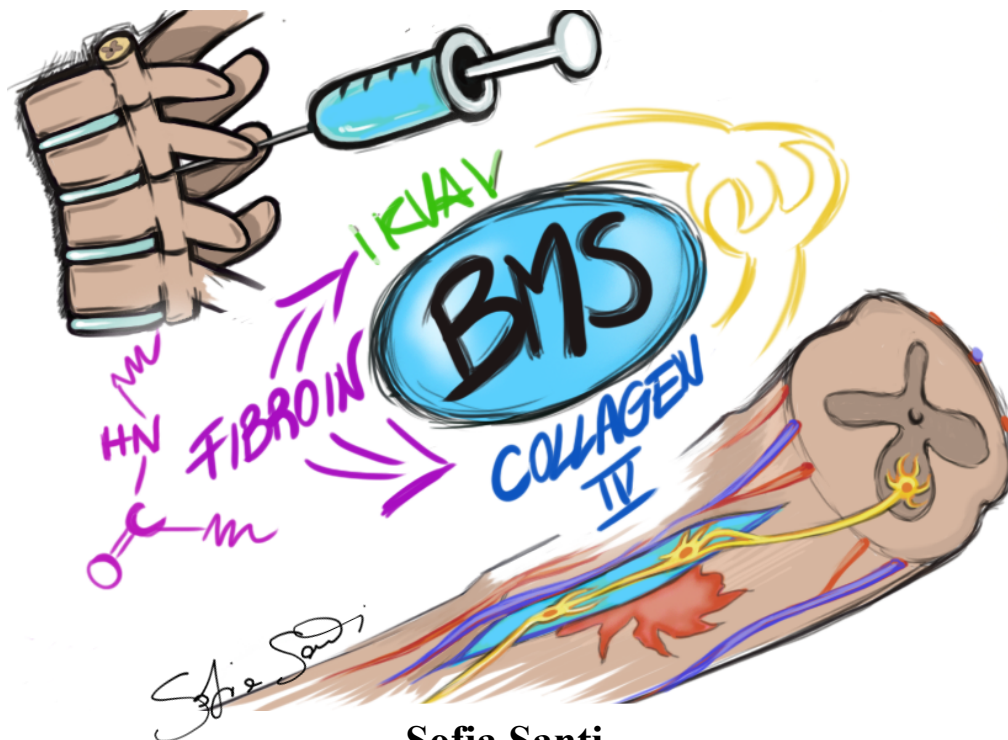
**UNIVERSITÀ
DI TRENTO**

**Department of
Industrial Engineering**

XXXIII cycle

Doctoral School in Materials, Mechatronics
and Systems Engineering

Bio-inspired materials for spinal cord regeneration



Sofia Santi

October 2021

Bio-inspired materials for spinal cord regeneration

Sofia Santi

Email: sofia.santi@unitn.it

Approved by:

Prof. Claudio Migliaresi, Advisor

Prof. Antonella Motta, Advisor

Dept. of Industrial Engineering

University of Trento, Italy

Prof. Nicola Pugno, Advisor

Dept. of Civil, Environmental and

Mechanical Engineering

University of Trento, Italy

PhD commission:

Prof. Daniel Cohn

*The Hebrew University of
Jerusalem, Israel*

Prof Keiji Numata

Kyoto University, Japan

University of Trento

Department of Industrial Engineering

October 2021

University of Trento - Department of Industrial Engineering

Doctoral Thesis

Sofia Santi - October 2021

Published in Trento (Italy) - by University of Trento

ISBN: - - - - -

To all

Abstract

Spinal cord injuries (SCI) following vehicle crashes, falls or cases of violence often lead to permanent functional and sensory loss due to the limited regenerative capacity of the central nervous system (CNS). Currently, most of the clinical trials are based on stem cell therapy or *in situ* pharmacological treatments. The main difficulty of the cell transplantation regards the inhospitality of the environment at and around the damaged tissue: inhibitory molecules and an inflammatory status prevent tissue regeneration, limit the cell survival and the clinical efficiency of cell therapy. This work proposes minimally invasive solutions avoiding further damages to the tissue. In particular, injectable biomaterials can be precisely positioned in the lesion site, and eventually repetitively injected until the complete regeneration of the tissue. Whenever is possible, minimally invasive procedures are preferred to treat spinal cord injuries (SCI), with percutaneous injections or small incisions, that are safer, faster, less traumatic and require less recovery time. Injectable repair systems are based on materials that can be injected in the lesion site, can eventually be loaded with drugs or even cells, and act as scaffolds for the lesion repair. For this application, a silk fibroin functionalized with collagen type IV and laminin-derived peptides, called bio-inspired multifunctionalized silk fibroin (BMS), possessing piezoelectric properties, has been synthesized.

Another approach that avoids damages to the spinal cord is proposed in the thesis as a multilayer hydrogel with piezoelectric properties that acts as a bridge between the healthy parts surrounding the injury. The multilayer hydrogel consists of i) a thin-layer of gelatin and fish collagen functionalized with VEGF for blood vessels formation, which helps the survival of the cells integrating with the pia mater of the spinal cord; ii) a BMS layer, which helps the adhesion, migration of neural stem cells and induces the sprouting of the axons thanks to the presence of Netrin (a chemoattractive protein); and iii) an adhesive layer of

polydopamine (PDA) to fix the patch on the injured site. The adhesive patch exhibits a potential larger than an injectable hydrogel that could guarantee a long-term cell survival and help the axons to move towards a direction.

The adhesive patch will be located on the surface of the spinal cord and the chemoattractive protein will induce the sprouting of the ascendant or descendant axons in the spinal cord to reach the axons present in the patch, restoring a signal connection.

Even if not final, the results indicate that the above strategy could be explored further for the regeneration of the spinal cord.

List of Figures

Figure 1. Neurogenesis (Original figure by Sofia).1

Figure 2. Growth cone regions and distribution of microtubules and actin within the sections (Original figure by Sofia).2

Figure 3. Growth cone behaviour depending on extracellular signals (Original figure by Sofia).....3

Figure 4. Spinal cord organization (Original figure by Sofia).....4

Figure 5. Motor and descending pathways in red, sensory and ascending pathways in blue (From Lateral corticospinal tract - Wikipedia).6

Figure 6. Relation between the central nervous system (CNS) and microvasculature (Original figure by Sofia). ..8

Figure 7. Timeline of the events following a SCI. Four stages characterize the injury progression: immediate, acute (0-7 days), sub-acute (7-14 days), and chronic (months).Figure 1 Timeline of the events following a SCI. Four stages characterize the injury progression: immediate, acute (0-7 days), sub-acute (7-14 days), and chronic (months).....13

Figure 8. Pathophysiology model during the regenerative phase, involving the polarization of the monocytes in anti-inflammatory M2 macrophages to start the healing process.15

Figure 9. Achievements reported in the cited papers.18

Figure 10. Morphology and immunohistochemistry of spinal cord tissue suggests: (1) muscle, (2)26

Figure 11. SHIELD design (left) and a scan fluorescent images (right) of spinal cord sections display cavity areas across all groups: untreated lesion (injury) SHIELD design (left) and a scan fluorescent images (right) of spinal cord sections display cavity areas across all groups: untreated lesion (injury), injury treated with saline medium (saline), injury treated with saline medium (saline) and Schwann cells (SC in saline), injury treated with SHIELD and Schwann cells (SC in SHIELD), Cyan, GFAP (right).....29

Figure 12. Injected drugs such as ChABC delivered by nanoparticles (NPs) showed a local action/extrinsic strategy of CSPGs removal. The remaining inhibitory molecules are not completely removed, and a pathological status is partially present (left), while a regenerative process (plasticity increasing, axonal growth and elongation) can be observed. Luxol fast blue (LFB) (A–D) and Bielschowsky (E–H) staining of longitudinal sections of the injured spinal cord within 8 weeks after treatment (right). The samples observed are (A, E) the sham group, (B, F) untreated spinal cord after injury, (C, G) PLGA NPs injected without ChABC (D, H) the ChABC particle-treated groups. In the Bielschowsky staining, the axons appear brown to black in color. W and G stand for the white and the gray matter of the spinal cord, respectively.31

Figure 13. Injection of I-5 hydrogel stimulates an “intrinsic” mechanism of MMP-9 and M2 macrophages recruitment come from the surrounded tissue. The imidazole rings located in the hydrogel matrix interact with the

histamine receptors on macrophages that linger for a prolonged time enhancing a wound healing mechanism (left). On the right (a-d) the effects of I-5 injection can be evinced: a cystic cavity reduction, ECM remodelling and inflammatory response decrease. Representative images of transverse spinal cord sections stained with eriochrome cyanine and eosin (a, b) or GFAP antibodies (c, d). Spinal cord sections were obtained from animals 4 weeks after PBS (a, c) or I-5 injection (b, d). The sections shown are from the epicenter and 1.2mm rostral (+1.2 mm) or caudal (-1.2 mm) to it. Asterisks indicate cystic, cystic boundary are indicated by black arrows (b). Scale bars represent 200 μm32

Figure 14. Quantification of hematoma. (A) At 3 day after injury (dpi) both SAP-treated groups had a significant lower leakage of red blood cells in comparison with controls. At Quantification of hematoma. (A) At 3 day after injury (dpi) both SAP-treated groups had a significant lower leakage of red blood cells in comparison with controls. At 7 dpi biotin-LDLK12-treated animals showed the lowest content of red blood cells, while B24 the highest one. (B) Longitudinal sections stained with hematoxylin/eosin showed the presence of extravasated red blood cells (red-brownish coloured). Scale bar: 700 μm37

Figure 15. The first day of OTS-SC culture (A) is compared with the slice observed seven days after injury (DPI:7) (B) and its uninjured counterpart (DIV:14) (C). The first day of OTS-SC culture (A) is compared with the slice observed seven days after injury (DPI:7) (B) and its uninjured counterpart (DIV:14) (C). In the diagram (D) is reported the expression of β III Tubulin in spinal cord slices42

Figure 16. Structure design of Azide SF-IK, Col(IV)/DBCO and of the bio-inspired multi-functionalized silk fibroin (BMS). The BMS is formed after the click reaction between the precursors.50

Figure 17. Synthetic sequence to obtain the biomimetic Synthetic sequence to obtain the biomimetic multi-functionalized silk fibroin (BMS): a) conjugation of the Azide terminated SF with IK; b) Formation of the “Col(IV)/DBCO” precursor; c) Reaction between Azide SF-IK and Col(IV)/DBCO to form the multi-functionalized silk fibroin (BMS).....57

Figure 18. ^{13}C CPMAS NMR spectra of silk fibroin and modified fibroin. (A: alanine, G: glycine, S: serine, Y: tyrosine).....59

Figure 19. XPS core lines for Silk fibroin (a and b) and BMS (c and d).....61

Figure 20. ATR-FTIR spectra of lyophilized SF-based solution (a) and hydrogels (b)64

Figure 21. Modulated DSC curves of 4-azidoaniline hydrochloride (4-Az), Col(IV) and lyophilized silk fibroin-based hydrogels.65

Figure 22. Rheological evaluation of the storage and loss modulus in the range of 1-100 Hz of unmodified and modified silk fibroin.67

Figure 23. Early adhesion of MRC5 on modified and unmodified films (a) and hydrogels (b) at different time points (1-3-7 days) (h: hydrogel; f: film).....69

Figure 24. AlamarBlue assay for the evaluation of the cell viability of MRC5 cultured on modified (BMS) and unmodified fibroin (SF) films (f) and hydrogels (h) at day 1-3-7. (*p<.05, **p<.01, ***p<.001, ****p<.0001, ns=not significant). AlamarBlue assay for the evaluation of the cell viability of MRC5 cultured on modified (BMS) and unmodified fibroin (SF) films (f) and hydrogels (h) at day 1-3-7. (*p<.05, **p<.01, ***p<.001, ****p<.0001, ns=not significant).....	70
Figure 25. Set up for the SF solution stimulation at 220 V or 24 V. Geometry A (green box) and geometry B (red box).....	78
Figure 26. Dynamic Mechanical Analyzer combined with a multimeter for the piezoelectric measurements.	79
Figure 27. Electric field lines generated with a potential of 220 V.	81
Figure 28. Dipoles orientation during the electric field application and gel formation (left) and dipoles rotation during the deformation. When the dipoles are oriented along the compression direction a potential generates....	82
Figure 29. Piezoelectricity of the BMS hydrogel. Geometry A (A) and Geometry B (B). (alternating current: AC, direct current: CC).....	83
Figure 30. Summary of the BMS results. Geometry A (green box) and geometry B (red box).....	84
Figure 31. ATR-FTIR deconvoluted peaks of h-BMS treated with 24 V or 220 V in alternating (AC) or direct current (DC).....	85
Figure 32. Dye-netrin diffusion.	94
Figure 33. Anti DCC immunostaining highlights the presence of DCC receptor near the nucleus of undifferentiated hNSCs and a decrease of the signal in the differentiated stage. The staining on MRC5 reveals the absence of DCC receptor.	95
Figure 34. Anti-DCC staining on hNSCs 3 days after the addition of the differentiative medium change. The red signal is due to the presence of DCC receptor near the growth cone, the green staining refers to the Oregon Green staining for the cytoskeleton and the blue one to the DAPI that highlights the nucleus.....	96
Figure 35. Live and Dead staining of hNSCs on TCP, hNSCs encapsulated into the BMS hydrogel with	97
Figure 36. Schematical explanation of two different approaches for SCI repair.	100
Figure 37. Alamar blue staining Cell metabolic activity evaluated by Alamar blue staining assay of a 2D hydrogel of the rabbit CECs after 3-7-14 days after seeding.	110
Figure 38. Cell viability evaluated by MTT staining assay of a 2D hydrogel of the rabbit CECs after 3-7-14 days after seeding.....	110
Figure 39. Live/dead staining of a 2D hydrogel of the rabbit CECs after 3-7-14 days.	112
Figure 40. VEGF release (left) and degradation test (right).	113
Figure 41. Immunohistochemical analysis by using H&E and Anti-vWF staining after 10 days of incubation of Ge/Col-I based material inserted subcutaneously in male rats. Scale bar of 200 um.	114

Figure S. 1. Measured evolution of the SF free amine groups after 7 days of dialysis.	119
Figure S. 2. Silk fibroin FAC evolution after EDC/NHS adding (SF edc), after coupling reaction of IKVAV (SF IK) and after diazonium coupling to form Azide SF (Az-SF).....	121
Figure S. 3. Efficiency of the coupling reaction between Col(IV) and DBCO groups.	122
Figure S. 4. Evaluation of cells number analysing the confocal images of modified (BMS) and unmodified fibroin (SF) films (f) and hydrogels (h) at day 1-3-7. The differences among the cell number of the same sample typology are negligible.	123
Figure S. 5. Cells adhesion of SH-5YSY after 7 days on SF hydrogels treated (24AC or 220 DC) or untreated. Scale bar 50 um inside the red box and 500 um for the low magnification.	125
Figure S. 6. Magnification of the SH-5YSY after 7 days. Scale bar 20 um. Electric field lines direction (white arrow).	126

List of Tables

Table 1. Non-invasive biomaterials-based scaffold for the treatment of SCI. The table highlights many features of the systems: the animal and related SCI model, the material and the shape of the scaffold, eventual signals and cells used. The obtained achievements and the associated observations are also summarized.....	20
Table 2. . a) Components of the SF-Col(IV). The -N=, =N- and =N+= bonds are referred to azide groups. The -N=N- and -N< bonds are referred to triazole compounds.. a) Components of the SF-Col(IV). The -N=, =N- and =N+= bonds are referred to azide groups. The -N=N- and -N< bonds are referred to triazole compounds. b) Components of azide groups. c) Components of triazole compound.....	61
Table 3. Characteristic DSC values of modified and unmodified silk fibroin hydrogels.....	65
Table 4. Values of the selected dielectric materials.	77
Table 5. Summary of the ATR-FTIR results for the amide I (A) and amide II (B) of BMS treated (24 AC/DC, 220 AC/DC) and untreated BMS (C).	86
Table 6. Design of experiment.	107
Table 7. Summary of the results obtained for each natural material of the DOE.....	111
Table S. 1. DLS analysis of SF solution dialyzed from day 3 (D3) up to day 7 (D7). The analysis starts from D3 in accordance with the beginning of the conjugation reactions.....	120
Table S. 2. Piezoelectricity values of treated and untreated SF at different concentrations. The values not reported regards samples that broke during the analysis.	127

List of Abbreviations

- Spinal cord injuries (SCI)
- central nervous system (CNS)
- bio-inspired multifunctionalized silk fibroin (BMS)
- polydopamine (PDA)
- dorsal root ganglia (DRG)
- receptor tyrosine kinases (RTKs)
- extra cellular matrix (ECM)
- cell adhesion molecule (CAM)
- collagen type I (Col-I)
- silk fibroin (SF)
- myelin-associated glycoprotein (MAG)
- chondroitin sulfate proteoglycans (CSPGs)
- oligodendrocyte-myelin glycoprotein (OMgp)
- chondroitinase ABC (ChABC)
- blood-brain barrier or blood spinal cord barrier (BSB)
- self-assembling peptide materials (SAPs)
- amphiphilic diblock copolypeptide hydrogels (DCHs)
- peripheral nervous system (PNS)
- monocyte chemoattractant protein 1 (MCP1)
- brain-ventricular choroid plexus (CP)
- blood-cerebrospinal-fluid (CSF)
- hyaluronan-methylcellulose (HAMC)
- oligodendrocyte progenitor cells (OPCs)
- platelet-derived growth factor receptors (PDGF-R)
- NanoGel (NG)
- Shear-thinning Hydrogel for Injectable Encapsulation and Long-term Delivery (SHIELD)
- mesenchymal stem cells (MSCs)
- bovine serum albumin (BSA)
- magnetic resonance imaging (MRI)
- polycaprolactone (PCL)
- thiolated hyaluronic acid (HA-SH)
- polyethylene glycol diacrylate (PEGDA)
- mouse embryonic stem cell (mESC)
- paclitaxel (PTX)
- minocycline hydrochloride (MH)
- Amphiphile peptides (AP)
- bone marrow homing peptide 1 (BMHP1)
- organotypic slices (OTSS)
- Basso, Beattie, and Bresnahan locomotor score (BBB)
- rate-dependent depression (RDD)

- advanced therapy medical product (ATMP)
- type IV Collagen, Col(IV)
- IKVAV peptide (IK)
- Strain-Promoted Azide-Alkyne Cycloaddition reaction (SPAAC)
- dibenzocyclooctyne-sulfo-N-hydroxysuccinimidyl ester (DBCO-NHS)
- Dynamic light scattering (DLS)
- 2,4,6-trinitrobenzene sulfonic acid (TNBS)
- free-amino groups (FAC)
- thermogravimetric analysis (TGA)
- X-ray photoelectron spectroscopy (XPS)
- Solid-state nuclear magnetic resonance (NMR)
- Differential scanning calorimetry (DSC)
- 4',6-diamidino-2-phenylindole (DAPI)
- alternating current (AC)
- hyperpolarization (AHP)
- human neural stem cells (hNSCs)
- deleted in colorectal cancer (DCC)
- un-coordinated-5 homolog (UNC5B)
- Minimally invasive injectable biomaterials (MIIB)
- ethylene glycol (EG)
- triethylene glycol (TEG)

Contents

Abstract	vi
List of Figures	viii
List of Tables	xii
List of Abbreviations	xiii
Contents	xvi
Preface.....	xx
Chapter 1	1
Introduction.....	1
1.1 Spinal cord origins.....	1
1.2 Descending and ascending tracts.....	5
1.3 Spinal meninges	7
1.4 Spinal cord injury	8
1.5 Injectable Scaffold-Systems for the Regeneration of Spinal Cord: Advances of the Past Decade (review)	10
1.5.1 Introduction.....	11
1.5.2 Pathophysiology	13
1.5.3 Non-invasive materials for SCI treatment: description and results	17
1.5.4. Spinal cord injury models.....	39
1.5.5. Severe contusion model as the new gold standard: how?.....	40
1.5.6. Conclusions.....	43
Chapter 2	45
Experimental studies	45

2.1 A bio-inspired multi-functionalized silk fibroin (BMS)	45
2.1.1. Introduction.....	47
2.1.2 Materials and Methods	51
2.1.3 Results and Discussion	57
2.1.4 Conclusions.....	70
2.2 Electric field effect on piezoelectric properties of BMS	72
2.2.1 Introduction.....	72
2.2.2 Materials and Methods	76
2.2.3 Results and Discussion	81
2.2.4 Conclusions.....	87
2.3 Biological effect of BMS hydrogel on hNSC	89
2.3.1 Introduction.....	89
2.3.2 Materials and Methods	90
2.3.3 Results and Discussion	93
2.3.4 Conclusions.....	98
Chapter 3	99
BMS-based alternative approaches for spinal cord regeneration.....	99
3.1 Minimal invasive approach by using an injectable BMS hydrogel.....	101
3.2 Adhesive patch	103
3.2.1 A thin layer hydrogel of gelatin and fish collagen functionalized with VEGF for blood vessels formation	105
Chapter 4	116
Future perspectives	116
Supplementary materials.....	119
Bibliography.....	129

Scientific Production.....	154
Participation to congresses and schools	156
Acknowledgements	157

Preface

This thesis reports the research activities conducted during my PhD program, at the BIOtech Research Center and Industrial Engineering Department of the Trento University, under supervision of Professor Antonella Motta, Professor Claudio Migliaresi and Professor Nicola Pugno. Parts of the research were performed in collaboration with the Department of Engineering of Chonbuk National University (Jeonju, South Korea) under the supervision of Professor Gilson Khang. The general aim of this work was to describe two minimal invasive approaches for the spinal cord regeneration. The first one regards injectable materials studied in the last decade and the second one a multilayer hydrogel, which was studied and produced during the doctorate. The thesis illustrates the materials and methods adopted, the experiments performed and the results obtained, following the structured chapters: the Chapter 1 reports the spinal cord development, anatomical structure and pathophysiology after an injury. Moreover, an overview of the minimal invasive systems used for spinal cord repair is also reported (published review). The Chapter 3 describes a minimal invasive system based on an injectable multifunctionalized silk fibroin (BMS) and a multilayer hydrogel, as an alternative approach, consisting in a thin layer hydrogel of gelatin and fish collagen functionalized with VEGF for blood vessels formation and a multifunctionalized silk fibroin (BMS), which was analysed in depth in terms of electrical, biological, chemical and mechanical properties in Chapter 2. The last Chapter reports the future perspectives: *in vitro* and *in vivo* evaluation of the adhesive patch and BMS based injectable hydrogel.

Chapter 1

Introduction

1.1 Spinal cord origins

The spinal cord originates from the neural tube and will represent the central nervous system (CNS); the peripheral ganglion and the dorsal root ganglia (DRG) originate from the neural crest that they will represent the peripheral nervous system (PNS), whereas the external ectoderm generates the epidermis ^{1,2} (Figure 1).

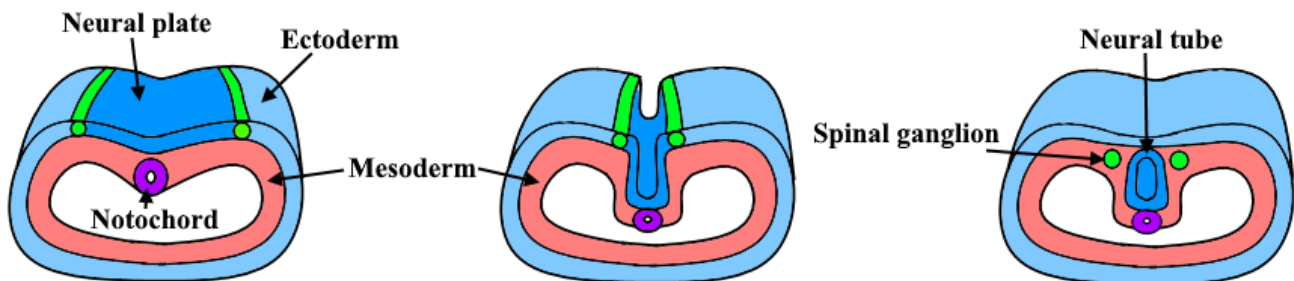


Figure 1. Neurogenesis (Original figure by Sofia).

After the neurogenesis, a neuronal migration is essential for the formation of the embryonic nervous system and for its maintenance during the adulthood ³. During the migration phase, primitive neurons, called neurites, start to elongate and branch from the cell body (soma) under the control of the growth cone.

The growth cone consists in three regions: central domain (C), transition zone (T) and peripheral domain (P) (Figure 2). The central domain contains i) vesicles and ii) microtubules made of tubulin that assembly

in a dynamic way guiding the growth cone. Microtubules penetrate the transition zone to invade the peripheral domain, thus they act as tracks for transportation and deliver both membrane and protein cargos (mitochondria, cytoskeletal polymers, autophagosomes, and synaptic vesicles containing neurotransmitters) to different sites.

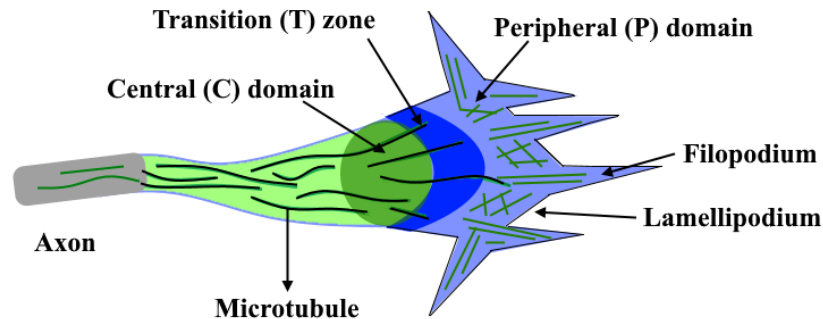


Figure 2. Growth cone regions and distribution of microtubules and actin within the sections (Original figure by Sofia).

The peripheral domain is composed of filopodia and lamellipodia filled with actin bundles, called F-actin. F-actin molecules assembly in these protrusion structures and power the growth cone motility^{4,5}. The growth cone is guided by chemical signals such as Netrin, N-terminal slit guidance ligand 2 (Slit2) and Neurotrophins that regulate positively the axon elongation and branching activity, whereas Semaphorins regulate negatively the axon growth and branching (Figure 3). The transduction pathway coming from Semaphorins (Sema) is linked to cytoskeleton remodelling, downregulating actin and microtubule dynamics and triggering morphological retraction of the motile growth cone structures^{1,4}.

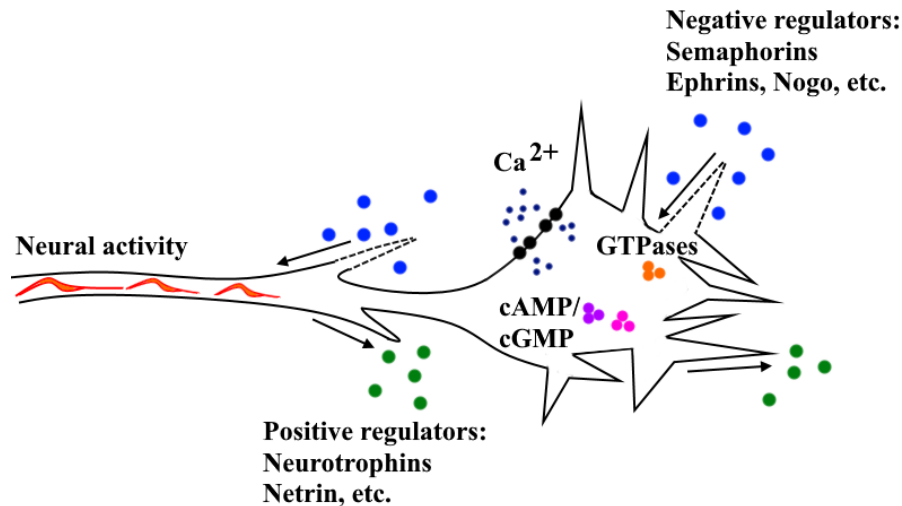


Figure 3. Growth cone behaviour depending on extracellular signals (Original figure by Sofia).

Instead, Ephs, which are receptor tyrosine kinases (RTKs), bind a second group of proteins called ephrins. The Eph–ephrin interaction can promote adhesion or repulsion of the growth cone depending on the precise signalling context.

The axon growth is possible only if growth cones find anchors such as factors associated with the extra cellular matrix (ECM) or if they interact with other cells by homophilic binding.

The factors associated with the ECM, such as collagen, laminin, fibronectin, interact with cell adhesion molecule (CAM) integrins to allow the cell adhesion and migration. In 1987 Duband and Thiery observed that collagen type I (Col-I) was involved during the neural crest cell migration (first stage) and disappeared when the cells aggregated into ganglia (second stage). In contrast, Col-IV and laminin appeared to remodel the tissue during the second stage and the nerve formation ⁶.

A structural variation of the nervous system during the postnatal ages is the development of the gray and white matter, that start a complex organization in nuclei and funiculi respectively.

Nuclei are a cluster of neurons such as motor neurons or somatosensory neurons localized in the ventral and dorsal horn of the gray matter respectively (Figure 4)⁴. Funiculi are, instead, bundles of axons that can transmit signals from the brain to the periphery (descendant fibers) or viceversa (ascendant fibers)⁷.

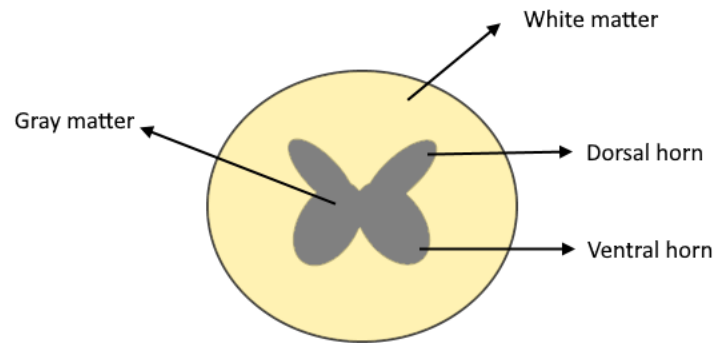


Figure 4. Spinal cord organization (Original figure by Sofia).

1.2 Descending and ascending tracts

The information can be sent to the brain or to the periphery, following the ascending or descending pathways respectively (Figure 5). The descending pathway includes:

- i) Lateral corticospinal tracts control distal limb movements and coordinate distal and proximal muscle, whereas the anterior corticospinal tracts control the movements of axial muscles (of the trunk).
- ii) Vestibulospinal tracts mediate reflexes that maintain balance and posture, changing in the centre of mass due to movement of the trunk, head, and limbs.
- iii) Rubrospinal tracts regulate the tone of limb flexor muscles and inhibitory to extension during the gait cycle.
- iv) Olivospinal tracts are thought to be also involved with motor control.
- v) Tectospinal tracts facilitate accurate head and eye movements in response to sound and light stimuli.
- vi) Reticulospinal tracts regulate the extension of the legs, to maintain postural support and to stimulate patterned movements (e.g. stepping). It is also responsible for flexor motor neurons thus inhibits the medial reticulospinal tract for the modulation of the stretch reflex. The loss of inhibitory projections to the spinal cord from the cortex has been thought to play an important role in spasticity observed in lesions of the cord, brainstem, or cortex.

The main ascending pathway includes:

- i) The gracile and cuneate fusciculus (posterior column) are heavily myelinated primary sensory fibers that convey proprioceptive, tactile, and vibratory information from the ipsilateral side of the body. Injury to the posterior columns on one side results in a loss of proprioception, discriminative touch, and vibratory sense below the level of the lesion on the same side.

- ii) Posterior and anterior spinocerebellar tracts influence the efficiency of motor activity.
- iii) Lateral and anterior spinothalamic tracts (ALS fibers) convey nociceptive, thermal, and touch information to higher levels of the neuraxis. Consequently, injury to the spinal cord that involves ALS fibers will result in a loss of pain, temperature, and crude touch sensations (poorly localized) on the contralateral side of the body, beginning about two segments below the level of the lesion.
- iv) Spino-olivary tracts convey unconscious proprioception from muscles and tendons as well as cutaneous impulses to the olivary bodies⁸.

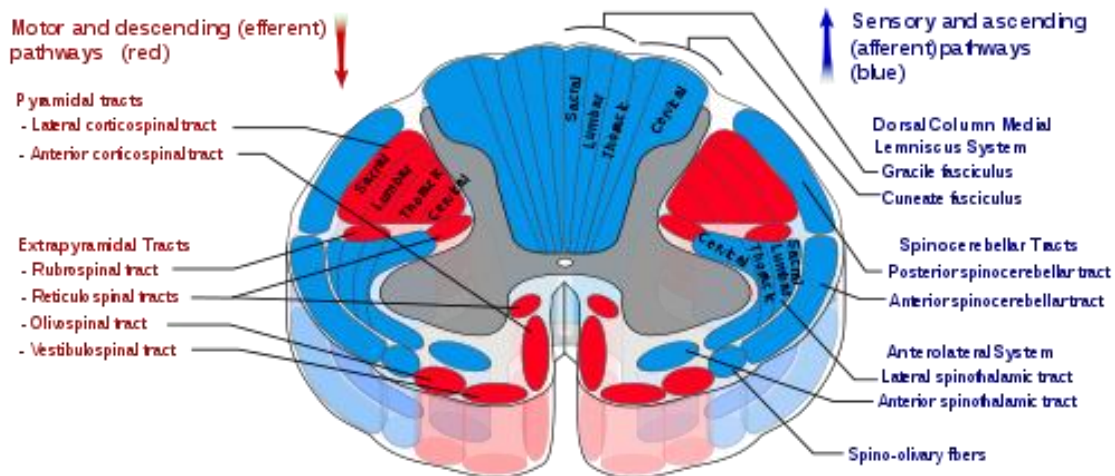


Figure 5. Motor and descending pathways in red, sensory and ascending pathways in blue (From Lateral corticospinal tract - Wikipedia).

1.3 Spinal meninges

The thecal sac or dural sac is a layer of dura mater that surrounds the spinal cord and the cauda equina. The thecal sac contains the cerebrospinal fluid which provides nutrients and upthrusts to the spinal cord. This dural sac is separated from the vertebrae by the epidural space, typically occupied by adipose tissue. The dura mater is the outset meninge and adheres on the surface of arachnoid mater, whereas the pia mater is intimately attached to the surface of the spinal cord. Pia mater is separated from the arachnoid matter through the subarachnoid space filled with the cerebrospinal fluid ^{2,9}. In particular, pia mater consists of layers of leptomenigeal cells, which have long and thin processes (protrusion). This layer can reach about 60 um at the optic nerve and 200 um at the thoracic and lumbar regions. The pia mater cells connect to each other by desmosomes and gap junctions and can be divided into parts: the **intimal** and the **epipial layer** ^{10,11}. The avascular **intimal layer** surrounds closely the spinal cord and the brain, it is composed of reticular and elastic fibers. The intimal layer rests on the basement membrane of the glial limitans (mainly astrocytes), from which it is separated by subpial space. The external, epipial, layer is mainly present in the spinal cord and only around the medulla oblongata of the brain. It consists of a vascular layer and a uniform network of collagenous fibers. The vascular layer supplies oxygen and nutrients to neural tissue by means of the glial limitans. The subpial space, previous cited, containing collagen bundles, fibroblast like cells and blood vessels that come from the epipial layer. The pia mater follows the small arteries and arterioles, which entry to the neural tissue and also within the subarachnoid space, and create a pial barrier between the subarachnoid space and a perivascular space ([Figure 6](#)). Indeed, the arterioles and capillaries that enter through the neural tissue are surrounded by a perivascular space, where the endothelial cells fuse with glial cells and seal the spaces.

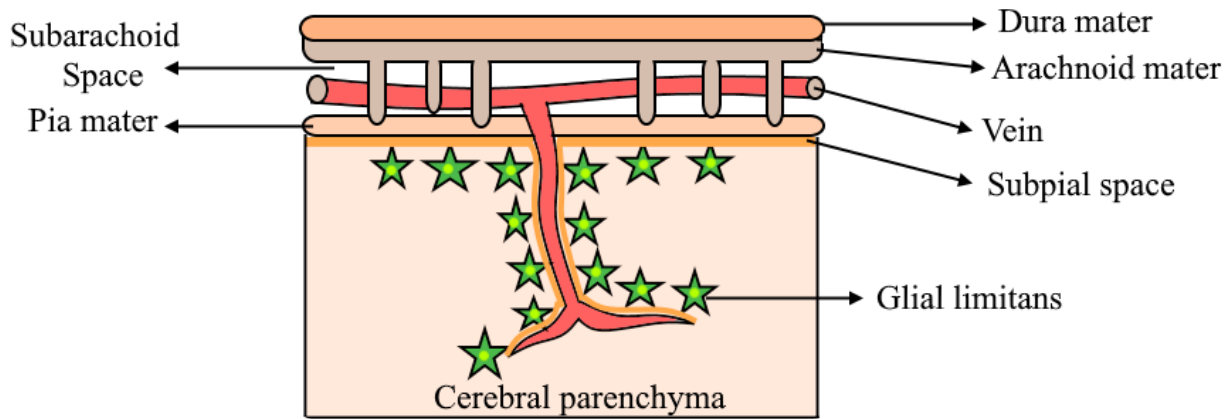


Figure 6. Relation between the central nervous system (CNS) and microvasculature (Original figure by Sofia).

1.4 Spinal cord injury

The incidence of spinal cord injury (SCI) is approximately 17,730 new cases each year in the United States¹². The leading causes of injury are vehicle crashes, followed by falls and the case of violence. Damages of the spinal cord often led to permanent functional and sensory loss due to the limited regenerative capacity of the central nervous system (CNS).

The clinical therapeutic guidelines of neurorestoration in the case of SCI are focused on alleviating secondary injury. They consist of restricting active and passive movement, early fixation, combined extramedullary and intramedullary decompression, suitable cell therapies, early rehabilitation, or electric stimulation therapy¹³. In particular, repetitive and rhythmical movements during early rehabilitation activate the spinal networks thanks to the sensorimotor information, which allows functional recovery and remodels the function of the cerebral cortex¹⁴. The neuroprotection aims to minimize secondary injuries by pharmacological therapy (i.e. erythropoietin, ibuprofen, indomethacin, anti-oxidants)¹⁵ to avoid cellular apoptosis or necrosis and promoting neuronal survival. These clinical guidelines are very

important to facilitate treatments by using prostheses or scaffolds to promote the regeneration of neural cells. The neuroregenerative therapies, instead, differ from the neuroprotective ones since they aim to create the best conditions for the neural tissue to maximally express its regenerative potential. The neuroregenerative approach is a younger discipline and thus few clinical trials have been performed. However, neuroregenerative methods seem to have less side effects than neuroprotective techniques. Given the advantages of both methodologies, the research is going toward combinatorial and interdisciplinary approach^{16,17}.

Currently, most of the clinical trials are based on stem cell therapy or *in situ* pharmacological treatments. The main difficulty of the cell transplantation regards the inhospitality of the environment at and around the damaged tissue: inhibitory molecules and an inflammatory status prevent tissue regeneration, limit the cell survival, and the clinical efficiency of cell therapy. Instead, pharmacological treatments such as i) neuroprotective agents¹⁸ (i.e. sodium salicylate, polyphenols, aspirin), ii) growth factors as well as iii) suppressors of inhibitory molecules of the inflammatory response (i.e. suppressors of NOGO-A, myelin-associated glycoprotein (MAG), oligodendrocyte-myelin glycoprotein (OMgp), and chondroitin sulfate proteoglycans (CSPGs) digestion with the administration of chondroitinase ABC (ChABC) or hyaluronidase)¹⁹⁻²² are hindered by the blood-brain barrier or blood spinal cord barrier (BSB) that limit their diffusion. Furthermore, high systemic doses to reach a therapeutic concentration at the site of the injury could induce tumor formation, fibrosis or other negative effects caused by the off-target of the molecules injected²³.

The following paragraph reviews the past decade literature on the scaffold systems proposed for the spinal cord regeneration. Published in ACS Biomaterials Science and Engineering, 2021, 7, 3, 983-999.

1.5 Injectable Scaffold-Systems for the Regeneration of Spinal Cord: Advances of the Past Decade (review)

Sofia Santi^{‡,§,*}, Ilaria Corridori^{‡,†,*}, Nicola M. Pugno^{†,‡}, Antonella Motta^{‡,§}, Claudio Migliaresi^{‡,§}

[‡]BIOTech Research Center and European Institute of Excellence on Tissue Engineering and Regenerative Medicine, University of Trento, Via delle Regole 101, 38123 Trento, Italy

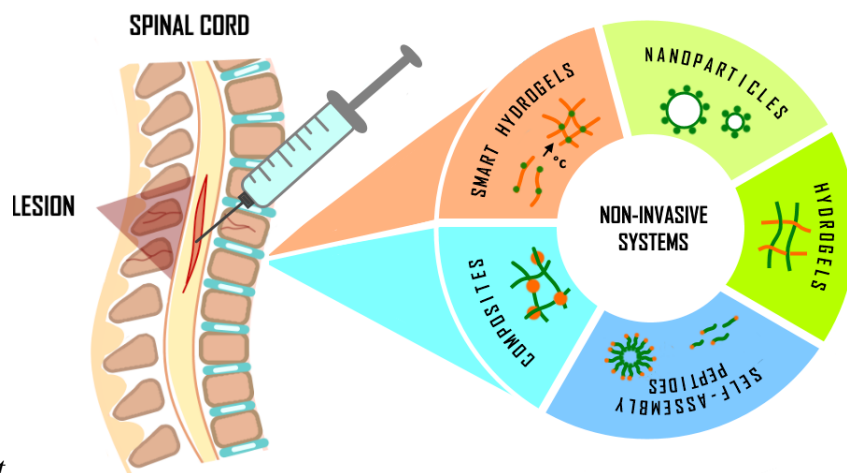
[§]Department of Industrial Engineering, University of Trento, Via Sommarive 9, 38123 Trento, Italy

[†]Laboratory of Bio-inspired, Bionic, Nano, Meta Materials & Mechanics, Department of Civil, Environmental and Mechanical Engineering, University of Trento, Via Mesiano 77, 38123 Trento, Italy

[‡]School of Engineering and Material Science, Queen Mary University of London, Mile End Road, E1 4NS London, United Kingdom

^{*}equally contributed

Abstract. Nowadays, whenever is possible and as alternative to open spine surgery, minimally invasive procedures are preferred to treat spinal cord injuries (SCI), with percutaneous injections or small incisions, that are faster, less traumatic and require less recovery time. Injectable repair systems are based on materials that can be injected in the lesion site, can eventually be loaded with drugs or even cells, and act as scaffolds for the lesion repair. The review analyzed papers written from 2010 onwards on injectable materials/systems used/proposed for the regenerative and combinatorial therapies of SCI, and discusses the *in vivo* models that have been used to validate them.



Graphical Abstract.

Keywords. Injectable hydrogel, smart hydrogel, injectable composite, injectable nanoparticles, injectable self-assembling peptides. All the listed keywords were linked to the spinal cord injury topic.

1.5.1 Introduction

The incidence of spinal cord injury (SCI) is approximately 17,730 new cases each year in the United States ¹². The leading causes of injury are vehicle crashes, followed by falls and the case of violence. Damages of the spinal cord often lead to permanent functional and sensory loss due to the limited regenerative capacity of the central nervous system (CNS).

The clinical therapeutic guidelines of neurorestoration in the case of SCI are focused on alleviating secondary injury. They consist of restricting active and passive movement, early fixation, combined extramedullary and intramedullary decompression, suitable cell therapies, early rehabilitation, or electric stimulation therapy ¹³. In particular, repetitive and rhythmical movements during early rehabilitation activate the spinal networks thanks to the sensorimotor information, which allows functional recovery and remodels the function of the cerebral cortex ¹⁴. The neuroprotection aims to minimize secondary injuries by pharmacological therapy (i.e. erythropoietin, ibuprofen, indomethacin, anti-oxidants) ¹⁵ to

avoid cellular apoptosis or necrosis and promoting neuronal survival. These clinical guidelines are very important to facilitate treatments by using prostheses or scaffolds to promote the regeneration of neural cells. The neuroregenerative therapies, instead, differ from the neuroprotective ones since they aim to create the best conditions for the neural tissue to maximally express its regenerative potential. The neuroregenerative approach is a younger discipline and thus few clinical trials have been performed. However, neuroregenerative methods seem to have less side effects than neuroprotective techniques. Given the advantages of both methodologies, the research is going toward combinatorial and interdisciplinary approach²⁴⁻²⁶.

Currently, most of the clinical trials are based on stem cell therapy²⁵ or *in situ* pharmacological treatments. The main difficulty of the cell transplantation regards the inhospitality of the environment at and around the damaged tissue: inhibitory molecules and an inflammatory status prevent tissue regeneration, limit the cell survival, and the clinical efficiency of cell therapy. Instead, pharmacological treatments such as i) neuroprotective agents¹⁸ (i.e. sodium salicylate, polyphenols, aspirin), ii) growth factors as well as iii) suppressors of inhibitory molecules of the inflammatory response (i.e. suppressors of NOGO-A, myelin-associated glycoprotein (MAG), oligodendrocyte-myelin glycoprotein (OMgp), and chondroitin sulfate proteoglycans (CSPGs) digestion with the administration of chondroitinase ABC (ChABC) or hyaluronidase)¹⁹⁻²² are hindered by the blood-brain barrier or blood spinal cord barrier (BSB) that limit their diffusion. Furthermore, high systemic doses to reach a therapeutic concentration at the site of the injury could induce tumor formation, fibrosis or other negative effects caused by the off-target of the molecules injected²³.

Researchers are pushing towards solutions avoiding further damages to the tissue. Non-invasive injectable biomaterials can be precisely positioned in the lesion site, and eventually repetitively injected to obtain the complete regeneration of the tissue. Moreover, the therapeutic advantages of directly

injecting therapies in the parenchyma of the spinal cord were proven superior concerning the systemic delivery of materials. ²⁷.

Some examples of injectable systems are i) self-assembling peptide materials (SAPs), whose gelation process is charge dependent; ii) amphiphilic diblock copolypeptide hydrogels (DCHs), which have a shear-thinning property, allowing the injection; iii) gel containing multiple tryptophans and proline-rich peptide domains, which undergo a sol-gel phase transition upon mixing or iv) injectable thermosensitive hydrogel of PEG–PLGA–PEG triblock copolymers ^{28,29}. The aim of this review is to provide an overview on the *in situ* injectable scaffold-systems. The possible injectable solutions analysed belong to four categories: hydrogels, nanoparticles, self-assembly peptides, and composites.

1.5.2 Pathophysiology

The SCI following trauma is characterized by four subsequent stages: immediate, acute (0-7 days), sub-acute (7-14 days), and chronic (months) (Figure 7).

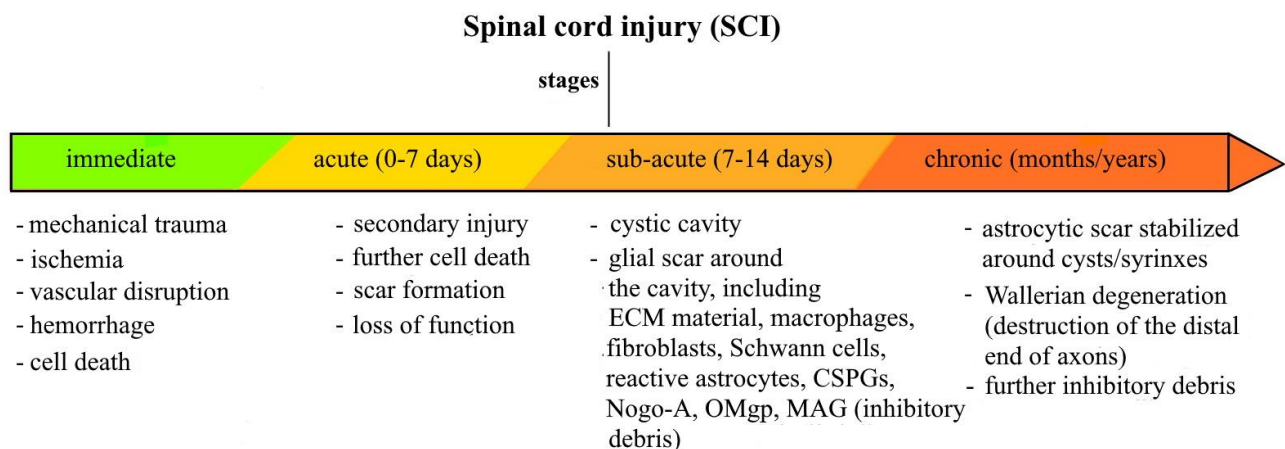


Figure 7. Timeline of the events following a SCI. Four stages characterize the injury progression: immediate, acute (0-7 days), sub-acute (7-14 days), and chronic (months). Figure 1 Timeline of the events

following a SCI. Four stages characterize the injury progression: immediate, acute (0-7 days), sub-acute (7-14 days), and chronic (months).

In particular, a spinal cord contusion leads to an inflammatory reaction at the lesion site with the infiltration of leukocytes and activation of glial cells which limit the damage by reestablishing blood brain barrier and ionic homeostasis ³⁰. However, the dense scar and inhibitory molecules such as chondroitin sulphate proteoglycans (CSPGs), Nogo-A, OMgp, MAG, which appear at later stages, are detrimental towards regeneration ³¹⁻³³. In particular, CSPGs interact with proteins in the extracellular matrix due to its negative charges and these interactions could inhibit the neurite outgrowth following CNS injury ³³. Thus, the inhibition of CSPGs by using the bacterial enzyme ChABC seems to be very promising for enhancing axonal regeneration ³⁴.

In the CNS, microglial cells are much slower compared to the peripheral nervous system (PNS) in clearing this debris, which may be present as long as three years post-injury ²⁸.

External the CNS, macrophages derived from circulating monocytes reach injured tissues and some of them seem to represent controlled recruitment needed for repair ³⁵ (Figure 8).

M1 monocyte macrophages were found to derive from monocytes that entered the injured spinal cord (SC) via monocyte chemoattractant protein 1 (MCP1) through the adjacent SC leptomeninges ³⁵. M1s possess proinflammatory, phagocytic, and proteolytic functions, essential for damaged tissue digestion and debris removal. M2 macrophages instead, came from monocytes that transit through the brain-ventricular choroid plexus (CP), via VCAM-1-VLA-4 adhesion molecules and epithelial CD73 enzyme ^{35,36}. Along with the CP, leukocytes extravasate across the endothelium, interact with the tightly connected epithelial cells, and enter the blood-cerebrospinal-fluid (CSF), facilitating the CNS immunosurveillance ^{35,37}. M2 possess anti-inflammatory functions and are involved in tissue regeneration, growth, angiogenesis, and matrix deposition, supporting tissue remodeling ^{35,38}.

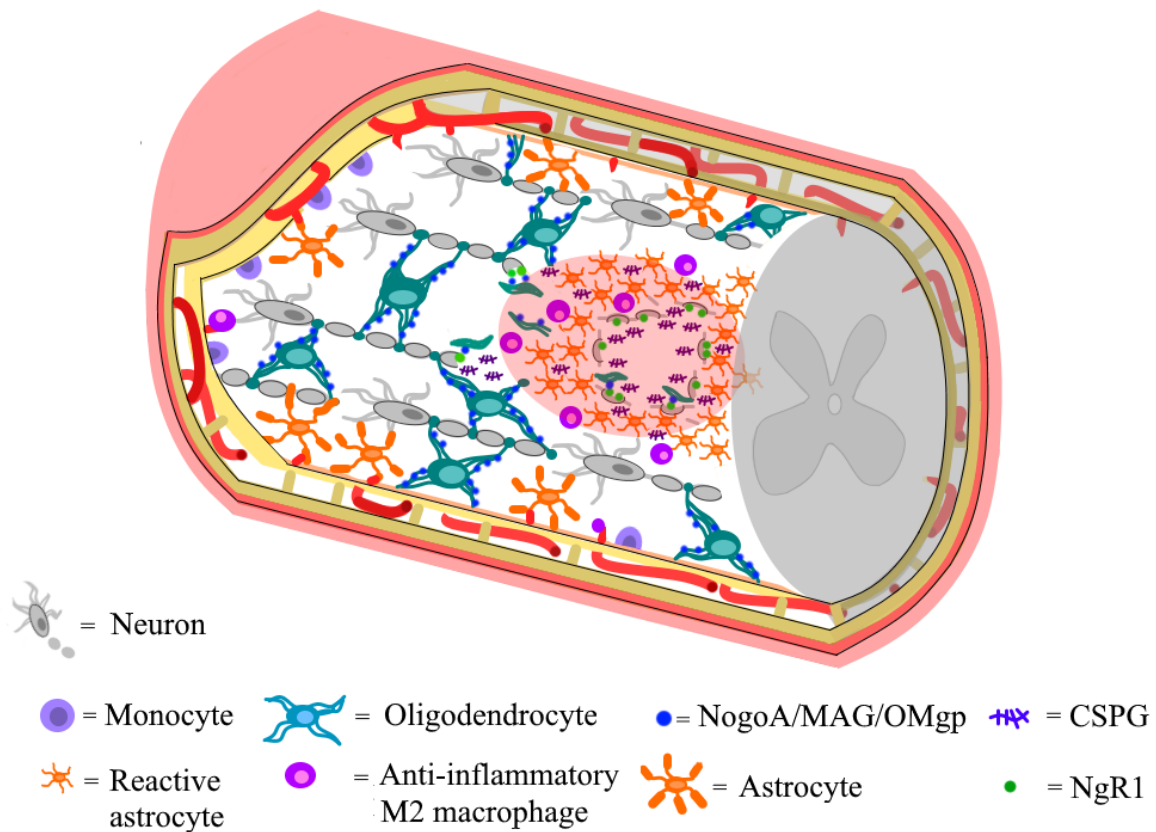


Figure 8. Pathophysiology model during the regenerative phase, involving the polarization of the monocytes in anti-inflammatory M2 macrophages to start the healing process.

During these detrimental phenomena, the neuroplasticity of the SC promoted in some cases spontaneous recovery of locomotor function after SC contusion³.

The reasons could be the variation of existing neuronal pathways, the formation of new connections, dendritic arborization remodeling, and axonal sprouting, regulating the expression of neurotrophin-3/4 (NT-3, NT-4), brain-derived neurotrophic factor (BDNF), and the glial cell-derived neurotrophic factor (GDNF)³⁹. The spontaneous recovery also involves the presence of proliferating ependymal cells at early

postinjury times, which later may have contributed to the expansion of the ependymal zone and the formation of cellular trabeculae within the lesion cavity ⁴⁰. The cellular trabeculae may serve to guide fibers from the CNS (like the corticospinal tract) into the center of the lesion. The dorsal roots likely represent the main source for axons and Schwann cells which provide most of the myelin ⁴⁰.

The presence of several regenerating axons within the lesion matrix after severe contusion injuries strongly suggests that under some conditions, the tissue repair response in the adult provides a substrate for growth.

1.5.3 Non-invasive materials for SCI treatment: description and results

A traditional surgery often requires a large incision with intrinsic risks, pain for the patient, perduring functional mobility, long hospital stay, long time of recovery and large costs for the healthcare system. Minimally invasive surgical procedures have root in the middle of last century, with the experimental use of arthroscopy, but only in the 80's minimally invasive surgery emerged as preferred alternative to open surgery procedures, to reduce trauma, surgery associated risks, pain for the patient and also treatment cost. Nowadays, the use of minimally invasive surgical procedures is considered of paramount importance as also evidenced in international research and innovation roadmaps and programs. For the spinal cord minimally invasive treatments, *in situ* injectable materials such as nanoparticles³⁴, smart hydrogels^{14,41}, injectable lipid microtubes⁴², self-assembling peptides⁴³, and self-assembling nanofibers⁴⁴⁻⁴⁶ have been widely investigated and proposed. Injectable materials allow minimally invasive implantation procedures and present shape versatility; some of them can have stiffness comparable to the human spinal cord and possess water retention²⁸. Moreover, they can be injected repeatedly until the complete functional tissue formation. Many of them can be functionalized or combined with adhesion ligands (i.e., IKVAV, RGD, CQAASIKVAV), growth factors (ex. fibroblast growth factor-2, FGF2, Neurotrophin-3, NT3), enzymes (es. chABC), and anti-inflammatory molecules (i.e. minocycline) to allow cell attachment, renewal, sprouting and extra cellular matrix (ECM) regeneration. However several problems have been reported with the use of injectable materials: for instance, the injected materials could form aggregates, creating barriers to the tissue regeneration, as observed for collagen gels stabilized by carbodiimide that causes endogenous collagen deposition; an excessive swelling of the material could increase the local pressure causing secondary damages to the parenchyma^{14,47}. The electrical stimulation of neuronal cells^{48,49}, and the formation of a controlled 3D structure along the longitudinal axis of the spine seem to be important requirements for i) surviving and maintaining the

cells active ^{50,51}, ii) promoting long-distance axonal elongation ⁵², and iii) achieving oriented axons regeneration ⁵³ for a natural tissue structure. It is still a challenge for injectable materials.

Non-invasive biomaterials-based systems that have been used for SCI therapies can be classified in hydrogels, smart hydrogels, nanoparticles, composites, and self-assembling peptides often combined with cells and specific signals. These systems are discussed below, summarized in Table 1 and the achievements obtained are represented in Figure 9.

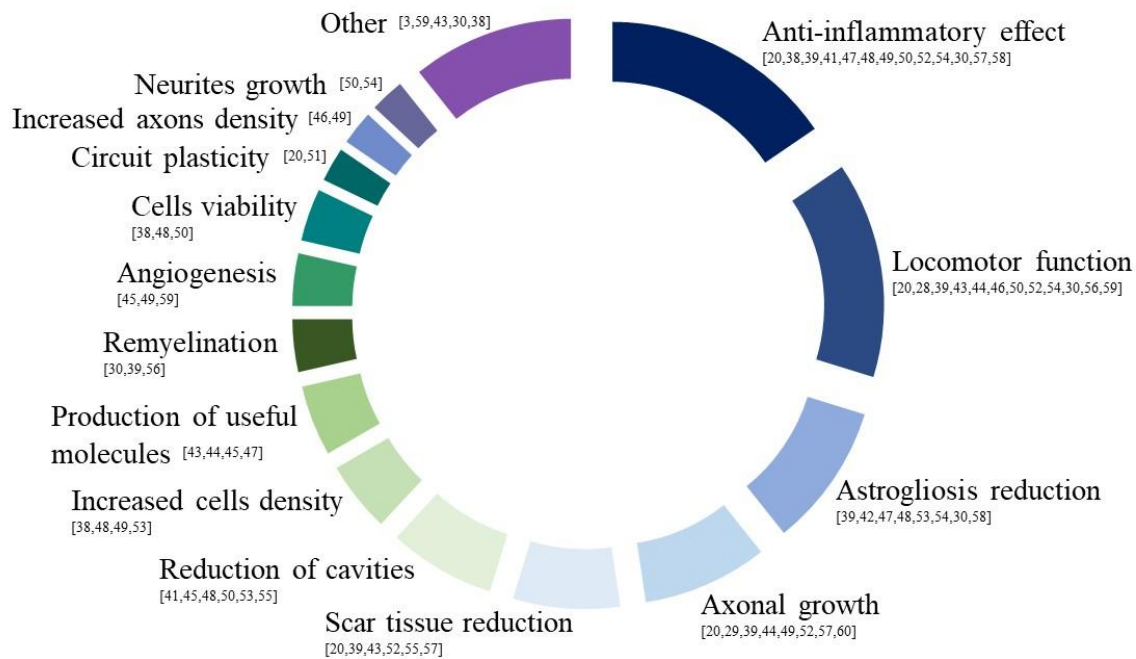


Figure 9. Achievements reported in the cited papers.

Table 1. Non-invasive biomaterials-based scaffold for the treatment of SCI. The table highlights many features of the systems: the animal and related SCI model, the material and the shape of the scaffold, eventual signals and cells used. The obtained achievements and the associated observations are also summarized

Reference	Animal model	SCI model/location	Material	Shape	Cells	Signals	Achievements	Observations
Azizi, M., et al. (2020) ³⁴	Rat	Contusion, T10	PLGA	Nano-particles		chABC	↑ Anti-inflammatory M2 macrophages ↑ Axonal growth scar digestion in the injured site ↑ Locomotor function ↑ Circuit plasticity	Failure of extensive axonal regeneration Incomplete cleavage of the CSPG, MAG, OMgp and Nogo
Bonnet, M, et al. (2020) ¹⁴	Rat	Contusion, T10	PNIPAAm-g-PEG	Thermo-responsive hydrogel			Unmodified inflammatory reaction ↓ Spasticity	No sensorimotor benefits after PNIPAAm-g-PEG combined with training Control+training and PNIPAAm-g-PEG+training had similar locomotor and ladder climbing test results.
Führmann, T., et al. (2016) ⁵⁴	Rat	Compression, T2	HA + MC	Hydrogel	OPCs	PDGF-A RGD	Cell survival, integration, and differentiation (glial phenotype) ↓ Teratoma	Teratoma formation not avoided Teratoma caused no improvements in motor function
Vismara, I., et al. (2020) ⁵⁵	Mice	Compression, T12	PEG + PEI	Nano-structured gel	iPs human-derived	Rolipam	NG internalisation in 24 hours Selective internalisation in pro-inflammatory phenotypes (in vitro) ↓ Pro-inflammatory response	The motor improvement observed at early stages after injury NG was not internalised in microglia and neurons

							NG internalisation in activated astrocytes, few in microglia none in neurons ↓ Production of inflammatory molecules by astrocytes (in vivo) Neuroprotective effect (in vivo)	
Wang, C., et al. (2019) ⁵⁶	Rat	Compression, T9	Laponite + heparin hydrogel	Hydrogel		FGF4	↑ Axonal regrowth ↑ Remyelination ↓ Astroglyosis ↓ Glial fibrotic scar ↓ Inflammatory response Motor functional recovery	
Hong, L.T.A., et al. (2017) ⁵⁷	Rat	Contusion, T10-11	imidazole-poly (organophosphazenes) (I-5)	Thermo-responsive hydrogel			↓ Cavity spaces Structural stabilisation ↑ Macrophages in the lesion for wound healing processes and ECM remodelling	
Boido, M., et al. (2019) ⁵⁸	Mice	transection	Chitosan+ β GP	Thermo-responsive hydrogel		MSCs	Fast gelation ↓ Reactive astrocytes in the injury site ↑ MSCs survival in the injury site	Preliminary in vivo tests Locomotor recovery not evaluated
Li, X., et al. (2019) ⁵⁹	Rat	Hemisectomy, T9	P10R5-LA	Thermo-responsive hydrogel		Cabazitaxel	↑ Bladder functions ↓ Fibrotic scarring ↓ Axons growth inhibitory molecules ↓ Demyelination adjacent to the injury site Locomotor recovery	
Donaghue, I.E., et al. (2015) ⁶⁰	Rat	Impact/compression, T1-2	HA + MC + PLGA nanoparticles	Composite		NT-3 Anti-NogoA	Sustained release of NT-3 ↑ Axon density Unmodified inflammatory response ↑ Anti-NogoA with the addition of NT-3 ↑ Locomotor function	Unmodified inflammatory response

Kang, C.E., et al. (2012) ⁶¹	Rat	Compression, T2	HA + MC + PLGA nanoparticles	Composite	FGF2	<p>↑ Angiogenesis, ↓ cavity</p> <p>No proliferative lesion</p> <p>Sustained and long-term release of FGF2</p>	No functional improvements
Ansorena, E., et al. (2013) ⁶²	Rat	Hemisection	Alginate + fibrinogen + (PLGA microspheres)	Composite	GDFN	<p>↑ Number of neurofilaments</p> <p>Functional recovery</p> <p>Slow release of GDFN</p> <p>Homogeneous and dense regenerated tissues</p>	<p>Fast release kinetics</p> <p>Growing neurites absent within the lesion</p> <p>Free-GDNF hydrogels induced superior functional recovery compared to GDNF-microspheres hydrogel</p>
Jain, A., et al. (2011) ⁶³	Rat	Hemisection, T8-10	Agarose + lipid microtubes	Composite	BDNF, CA-Cdc42, or CA-Rac1	<p>↓ Number of astrocytes</p> <p>↓ CSPG deposition</p> <p>presence of neurofilaments across the lesion, ↑ Axons in the CSPG-rich regions</p>	<p>↑ immune/inflammatory response</p> <p>Dosage of the three proteins not optimized</p>
Chen, S., et al. (2020) ⁶⁴	Rat	Hemisection, T9-10	Silk fibroin + PDA			<p>↑ Axons length</p> <p>↑ Cell density</p> <p>↑ Cell viability</p> <p>↓ Glial cells</p> <p>High porosity</p> <p>Lesion cavity filled</p> <p>Fibrous distribution of neurons</p>	<p>Further in vivo studies needed</p> <p>Mechanical and morphological properties depend on PDA</p>
Li, X., et al. (2020) ⁶⁵	Rat	Contusion, T9	PCL + MAL (fibres) + HA-SH + PEGDA	Composite		<p>Limit spinal cord thinning</p> <p>↑ Cells infiltration and interaction</p> <p>Suitable porosity</p> <p>Shift of macrophages from M1 to M2</p> <p>↑ Neovascularisation</p> <p>↑ Differentiation of endogenous stem cells in immature neurons</p> <p>↑ Number of axons</p>	Role of nanofibers not fully known
Wang, C., et al. (2018) ⁶⁶	Mouse	Tissue removal, T12	[P(DLLA-co-TMC)] (fibres) + GCP	Composite	MN-ESC	<p>Cell survival and engraftment in vivo</p> <p>NF inducedr ESC differentiation</p> <p>Neurite grew parallel to the axia direction</p>	Slow degrading dynamic

							Lesion cavity totally filled ↓ Tissue loss ↓ Inflammatory response Motor function recovery	
Khaing, Z.Z. et al. (2016) ⁶⁷	Rat	Transection, T2	PLGA (nanoparticles)+ HA +MC	Composite		BDNF	Efficient delivery platform of bioactive molecules Material with tunable properties based on the molecular weight of HA Promotion of adaptive plasticity	Inflammatory response not investigated
Nazemi, Z., et al. (2020) ⁶⁸	Rat	Hemisection, T8-10	PLGA microspheres + Alginate	Composite		MH PTX	Prolonged release of the drugs (2 months) ↑ Inflammation, ↓ Scar tissue (ECM deposition) ↑ Axonal regeneration and protection reconnection of neural network Functional improvement	No therapeutic effect on cell death, no alteration of reactive astrocytes
Marquardt, L.M., (2020) ⁶⁹	Rat	Contusion, C5	C7 recombinant engineered peptide + PEG modified with proline-rich peptides + PNIPAM	Thermo-responsive polymer	SC		↓ Secondary injury ↓ Cystic cavitation ↓ Astroglyosis in the perilesion space ↑ Cell retention ↑ Neurons and axonal sparing	Unavoidable cell loss Ligands might be necessary Further full dynamic response of immune cells infiltration is necessary
Hu, H.Z., et al. (2018) ⁴²	Dog	chronic severe SCI, L3-4 L4-5	Lipid microtubes + agarose	Composite		chABC-trehalose	↑ Locomotor function No long-term adverse effects	No improvements in detection of sensory evoked potentials
Tavakol, S., et al. (2015) ⁷⁰	Rat	Chronic SCI, T10	(RADA)4-GG-BMHP1	SAP	hEnSCs	BMHP1	↑ Neural differentiation Functional recovery ↓ Reactive astrocytes ↓ Inflammatory response	Axon regeneration and myelination limited to the area around the cavity ↓ cell proliferation in more concentrated gels
Cicognini, D. et al. (2014) ⁴⁴	Rat	Contusion, T9-10	B24 and biotin-LDLK12	SAP			Haemostatic effect ↑ Axon sprouting/regeneration	SAP caused compression of the surrounding tissue
Zweckberger, K., et al.	Rat	Compression/contusion,	K2(QL)6K2 (QL6)	SAP	NPC	BDGF EGF	Cavity is bridged ↓ Scar tissue	Osmotic micro-pump necessary

(2015) ⁷¹		C5-6				FGF	↑ NPCs survival and migration	
Tysseling, V.M., et al. (2010) ⁴⁵	Mouse/rat	Compression, T10/ Compression, T13	Peptide amphiphile	SAP		IKVAV	Axon elongation Functional recovery Suppressed progression of astrogliosis ↑ Remyelination of axons inside the lesion Regeneration of corticospinal motor fibers and sensory fibers ↑ Number of serotonergic fibers caudal to the lesion significantly ↓ Cells undergoing apoptosis	Behavioural results depending on the compression Small number of regenerating dorsal column fibers
Ye, J.C., et al. (2016) ⁷²	Rat	Compression, T10	RADA16 (polypeptide)	SAP	NSC from primates		In vitro differentiation in neurons, oligodendrocytes and glial cells ↑ Myelin production ↑ Motor function recovery	Primate NSCs not easily available
Tran, K.A., et al. (2020) ⁷³	Rat	Contusion, C5	RADA16I	SAP	Human cerebral microvascular or endothelial cells		↓ Inflammatory response ↓ Glial scar Axon growth across the lesion	Not oriented structure New axons could origin from sprouting Perfusion in the microvessel not tested
Hassanejad, Z., et al. (2019) ⁴³	Rat	Compression, T7-8	CH ₃ (CH ₂) ₁₄ CO-AAAAGGGEIKVAV	SAP		IKVAV BDNF	No inflammatory reaction ↓ Astroglyosis ↑ Migration of astrocytes and oligodendrocytes in the injury Sustained release of BDNF for 21 days	Functional recovery was not statistically significant
Cicognini, D., et al. (2011) ⁷⁴	Rat	Contusion, T9-10	RADA16-4G	SAP		BMHP1	Remodelling of ECM Basement membrane deposition ↑ Angiogenesis ↑ Migration of neurons, microglia cells and oligodendrocytes precursors ↑ Locomotor functions recovery	Inflammatory response No cyst and cavities ↓ Partial filling of the injury cavity New axons could origin from sprouting

Sun, Y., et al. (2016) ⁷⁵	Rat	Transection, T	(Ac-(RADA)4-CONH ₂)	SAP	NSC/NPC	IKVAV RGD	↑ Cell viability and survival Differentiation of stem cells into neural and glial phenotypes in vitro Mild assembling process that preserve the environment	Slow in vivo gelation Axons growth along the graft and not across it
Sever-Bahcekapili, M, et al. (2020) ⁴⁶	Rat	Hemisection, T9-10	Peptide amphiphile	SAP		IKVAV heparan sulfate-mimetic epitope	↑ Tissue integrity ↓ Cell loss Neurons toward injection site ↑ Locomotor functions recovery	

1.5.3.1 Hydrogels. They are materials characterised by a three-dimensional network with a hydrophilic structure that holds large amounts of water. Hydrogels can be injected before crosslinking with it happening *in situ* in some seconds/minutes. Some hydrogels can display the so called “smart” behaviour, with a non-reversible or reversible transition from the state of sol to the state of gel following the application of external stimuli. The main component of the extracellular matrix of the spinal cord is hyaluronic acid (or hyaluronan HA) ⁷⁶, thus this natural polymer is widely used in SCI regenerative medicine. For example, hyaluronan-methylcellulose (HAMC) hydrogels, first studied by Gupta et al. ⁷⁷, loaded with oligodendrocyte progenitor cells (OPCs), platelet-derived growth factor receptors (PDGF-R), and RGD promoted the survival, integration, and differentiation of cells ⁵⁴. However, teratoma formation was not avoided but attenuated concerning the cell-therapy (Figure 10).

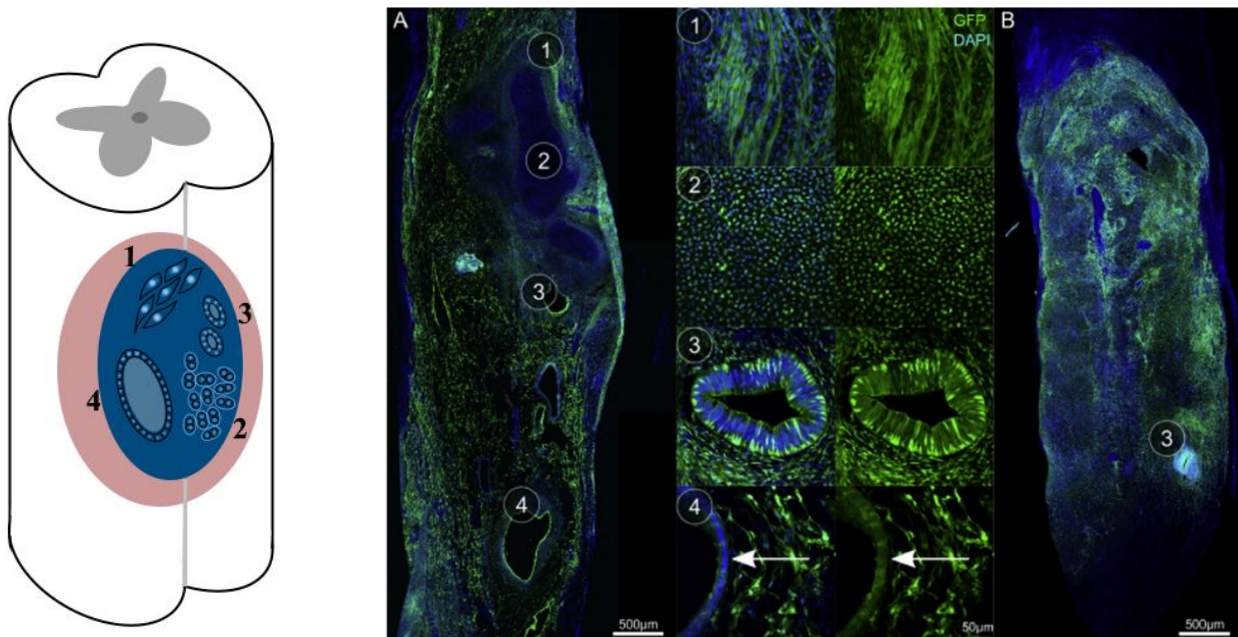


Figure 10. Morphology and immunohistochemistry of spinal cord tissue suggests: (1) muscle, (2)

cartilage, (3) intestinal-like, epithelium, and (4) epithelium (arrow) within the teratoma

Figure 10 (right, A-B) reproduced with permission from ref 54. Copyright 2016 Elsevier.

Other problems could also derive from a “not well cleaned” (full of debris) lesion site, which may impede the gelation of the material ⁴⁷. Moreover, considering some injectable hydrogels such as gelling agents (ex. β -glycerophosphate disodium salt hydrate, β -GP) ⁵⁸ blended with chitosan, imidazole-poly (organophosphazenes) (I-5) ^{57,78}, or poly-N-isopropyl acrylamide-based thermoresponsive hydrogels, the sol-gel transition could be preferentially promoted by physical factors (ex. temperature, physiological pH). to avoid inflammatory response, generally caused by chemical crosslinkers ¹⁴.

To avoid the harmful mechanisms activated by reactive astrocytes after SCI, a PEG (polyethylene glycol)-PEI (poly(ethylene imine)) NanoGel (NG) delivering Rolipram (antidepressant drug) was injected in a mice compression model ⁵⁵. The results showed a selective internalization of NG in activated astrocytes, few in microglia, and none in neurons. Motor functional improvement was possibly caused by a reduced production of inflammatory molecules by astrocytes and its consequent neuroprotective effect. This result was observed in the early stage after injury ⁵⁵.

A biopolymer largely proposed in regenerative therapy strategies is silk fibroin. Chen et al. ⁶⁴ produced a material coupling the silk fibroin with the quinone structure of oxidized dopamine (DA). DA is a mussel adhesion protein recently studied as a cross-linking medium to obtain injectable hydrogels ⁷⁹. Indeed, DA goes towards a self-polymerization of free DA generating an injectable silk fibroin/polydopamine (SF/PDA) hydrogel. This material has favoured neurite growth and neuronal differentiation. This scaffold presents tunable properties by varying the concentration of DA. *In vivo* tests showed repair of SC tissue after hemisection in rats but further investigation is needed to evaluate possible clinical studies. Recently, a synthetic smectite clay (Laponite XLG, $\text{Na}_{+0.7}[(\text{Si}_8\text{Mg}_{5.5}\text{Li}_{0.3})\text{O}_{20}(\text{OH})_4]^{-0.7}$) was also used

for SCI repair due to its capacity to aggregate in solution. Laponite XLG consists of interlayer cations (Na^+) that balance the net negative charge of a single crystal of Laponite. Its ability in binding heparin is exploited in regenerative medicine applications. Indeed, Wang C., et al. ⁵⁶ produced an injectable heparin-Laponite hydrogel loaded with a novel neuroprotective factor, the fibroblast growth factor 4 (FGF4). The results showed a motor functional recovery, reduced fibrotic scar tissue, and the inflammatory response with consequent remyelination.

Smart hydrogel polymers present a sol-gel transition responsive to different external stimuli: temperature, light, pH, ionic concentration, magnetic and electrical fields, and chemicals ⁸⁰. For thermo-responsive polymers, the transition occurs at specific threshold points: above the critical solution temperature (ex. LCST polymers) or below (ex. UCST polymers). The most common smart hydrogels used in SCI repair are thermoresponsive, such as poly(N-isopropyl acrylamide) (PNIPAAm) ¹⁴ or triblock copolymers based on polyethylene oxide, polyethylene glycol, polypropylene glycol, or polylactic acid (ex. PEO-PEG-PEO or PLA grafted on PPG-PEG-PPG) ⁸¹.

PNIPAAm-g-PEG (poly(N-isopropyl acrylamide-g-polyethylene glycol), introduced by Comolli et al. ⁸², was investigated in contusion SCI cases and results showed an unvaried inflammatory response ¹⁴. The locomotor recovery improved when PNIPAAm-g-PEG was combined with an exercise training program. The electrophysiological recordings indicated reduced spasticity of treated animals, but this benefit was not recorded when the polymer treatment was coupled with exercise.

PPG(polypropylene glycol)-PEG-PPG (P10R5) has been used to deliver a chemotherapeutic agent (Cabazitaxel) to the injured area ⁵⁹. Besides the inhibiting role of Cabazitaxel on prostate cancer, this chemotherapeutic drug was proven to be capable of supporting the neurite extension of cortical neurons *in vitro*. The treatment creates a protective environment leading to an improvement of bladder and locomotor functions.

Different delivery systems based on PNIPAM are produced to allow cells to reach the target site. Marquardt et al. ⁶⁹ synthesized an engineered protein (C7), composed by repetitive motives CC₄₃WW (Figure 11, left). The motives were separated by a multi-arm of 8-armed PEG tethered with proline-rich peptides, PNIPAMs, and cell-adhesive peptides (IKVAV, RGD, YIGSR). The system, called SHIELD (Shear-thinning Hydrogel for Injectable Encapsulation and Long-term Delivery) ⁸³, represents an example of injectable hydrogel for autologous human Schwann cells (SCs) transplantation. The cell membrane protection promoted by the SHIELD encouraged a decrease of the cystic cavity and an increase of the functional recovery (Figure 11, right).

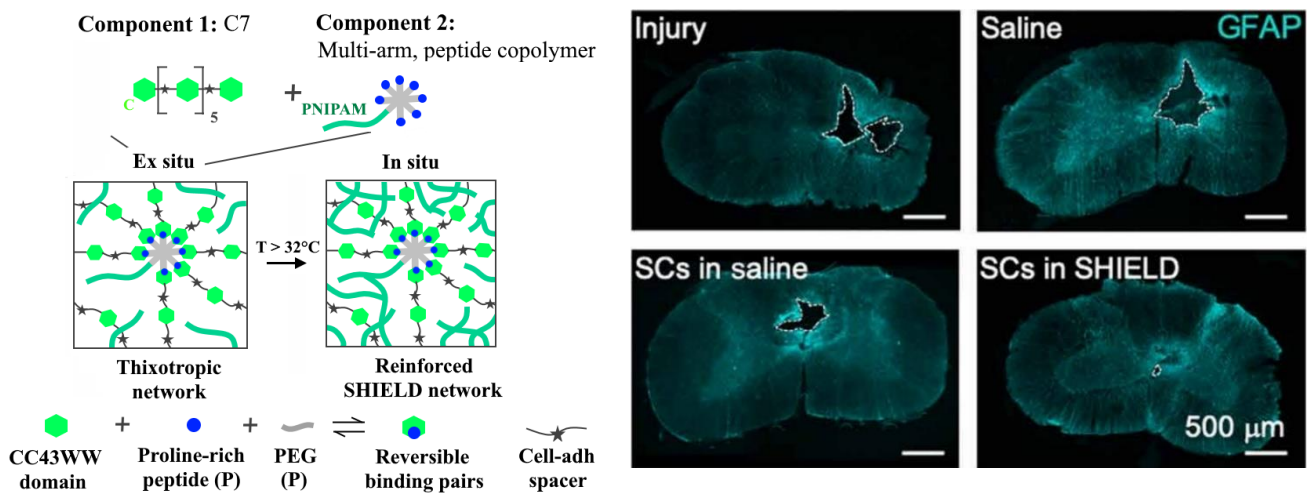


Figure 11. SHIELD design (left) and a scan fluorescent images (right) of spinal cord sections display cavity areas across all groups: untreated lesion (injury) SHIELD design (left) and a scan fluorescent images (right) of spinal cord sections display cavity areas across all groups: untreated lesion (injury), injury treated with saline medium (saline), injury treated with saline medium (saline) and Schwann cells (SC in saline), injury treated with SHIELD and Schwann cells (SC in SHIELD), Cyan, GFAP (right).

Figure 11 reproduced with permission from ref 69. Copyright 2020 American Association for the Advancement of Science.

1.5.3.2 Nanoparticles. Given the small dimensions, nanoparticles can be injected in the affected area through the needle of a syringe. The fabrication methods (ex. double emulsion/solvent evaporation technique, thermal decomposition) used to produce these particles give the opportunity of embedding specific signals or cells. Azizi et al.³⁴ studied the use of poly(lactic-co-glycolic acid) PLGA nanoparticles (273.5 ± 36.4 nm) embedding chABC in a rat contusion model. The anti-inflammatory response was promoted by the enhancement of regenerative M2 macrophages (in a process described above) and caused axonal regrowth (Figure 12). The improvement of locomotor functions and the enhancement of circuit plasticity were also observed. However, the PLGA nanoparticles failed in obtaining an extensive axonal regeneration and the complete cleavage of the CSPG, MAG, OMgp, and Nogo. These results were obtained through an "extrinsic" approach, different from the "intrinsic" one⁵⁷ described in Figure 7. Additionally, Zhang et al.⁸⁴ used nanoparticles to track the position of mesenchymal stem cells (MSCs), investigating their optimal number to transplant in the post-traumatic syrinx caused by SCI. Nanoparticles of 53 ± 9 nm made of ferric oxide (Fe_3O_4) cores were coated with bovine serum albumin (BSA) covalently conjugated with monoclonal antibodies against vascular endothelial growth factor (mAbVEGF). The results showed a precise transplantation strategy of MSCs thanks to the magnetic resonance imaging (MRI) visualization of magnetic nanoparticles.

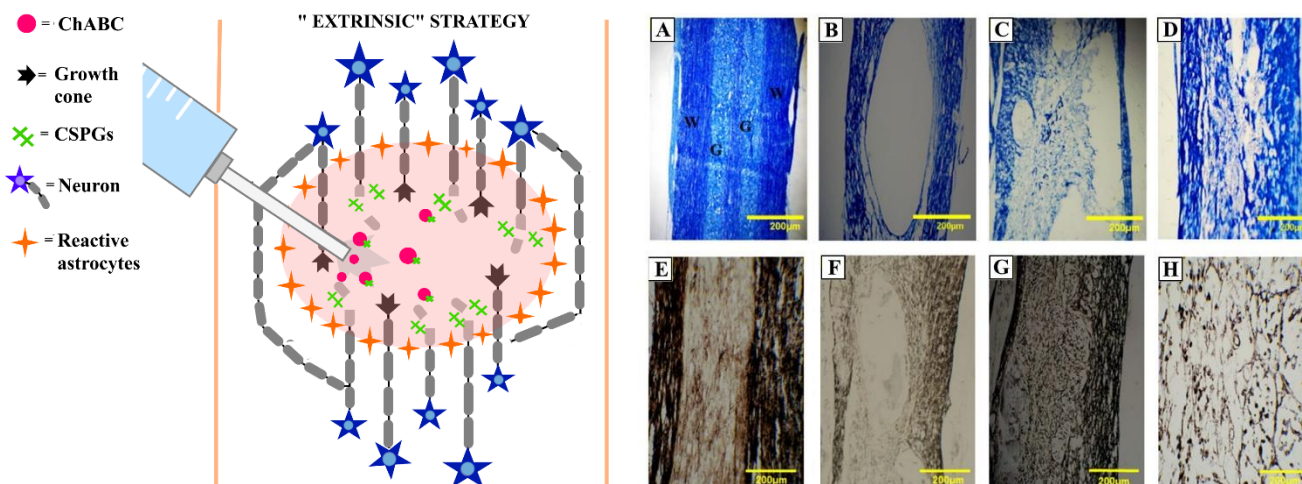


Figure 12. Injected drugs such as ChABC delivered by nanoparticles (NPs) showed a local action/extrinsic strategy of CSPGs removal. The remaining inhibitory molecules are not completely removed, and a pathological status is partially present (left), while a regenerative process (plasticity increasing, axonal growth and elongation) can be observed. Luxol fast blue (LFB) (A–D) and Bielschowsky (E–H) staining of longitudinal sections of the injured spinal cord within 8 weeks after treatment (right). The samples observed are (A, E) the sham group, (B, F) untreated spinal cord after injury, (C, G) PLGA NPs injected without ChABC (D, H) the ChABC particle-treated groups. In the Bielschowsky staining, the axons appear brown to black in color. W and G stand for the white and the gray matter of the spinal cord, respectively.

Figure 12 (right, A-H) reproduced with permission from ref 34. Copyright 2020 Elsevier.

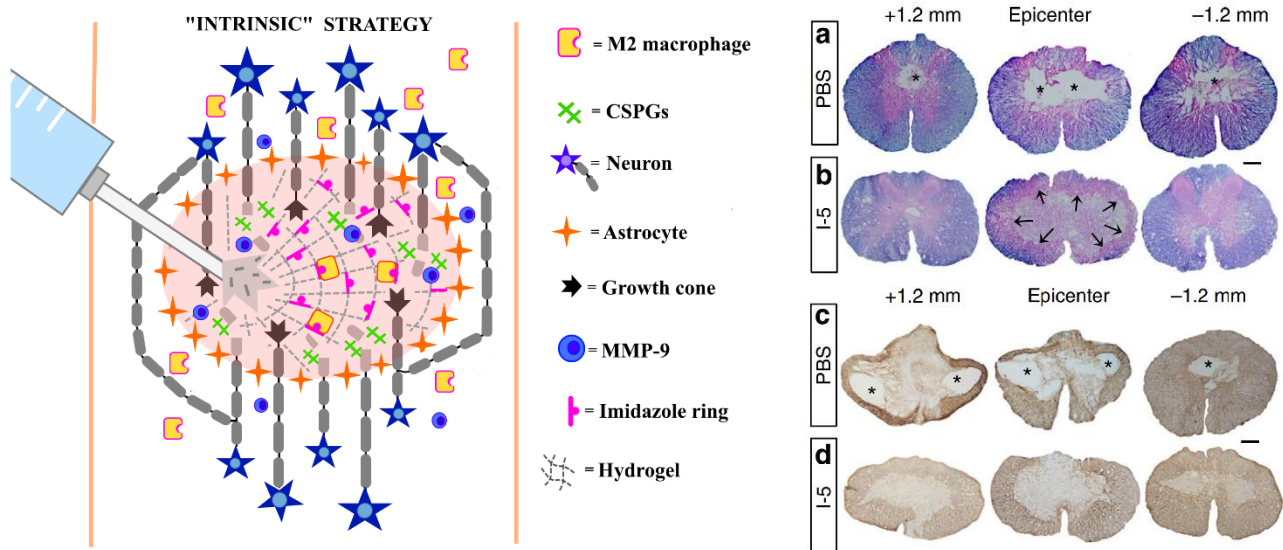


Figure 13. Injection of I-5 hydrogel stimulates an “intrinsic” mechanism of MMP-9 and M2 macrophages recruitment come from the surrounded tissue. The imidazole rings located in the hydrogel matrix interact with the histamine receptors on macrophages that linger for a prolonged time enhancing a wound healing mechanism (left). On the right (a-d) the effects of I-5 injection can be evinced: a cystic cavity reduction, ECM remodelling and inflammatory response decrease. Representative images of transverse spinal cord sections stained with eriochrome cyanine and eosin (a, b) or GFAP antibodies (c, d). Spinal cord sections were obtained from animals 4 weeks after PBS (a, c) or I-5 injection (b, d). The sections shown are from the epicenter and 1.2mm rostral (+1.2 mm) or caudal (−1.2 mm) to it. Asterisks indicate cystic, cystic boundary are indicated by black arrows (b). Scale bars represent 200 μm.

Figure 13 (right, a-d) reproduced with permission from ref 57. Copyright 2017 Springer Nature.

1.5.3.3 Composites. The term refers to the combination of two or more materials with different physical properties resulting in a new material with improved tailored characteristics. Injectable composites for

SCI repair are generally made of nanotubes/nanoparticles/nanofibers/microtubes embedded in hydrogels. In particular, microtubes are generated by self-assembly of glycolipids, phospholipids, and other amphiphilic molecules. Variation in concentration, pH, or temperature influences the supramolecular assembly, which is driven by van Der Waals, electrostatic forces, or hydrogen bonding. Microtubes embedded in hydrogels are investigated as drug carriers for SCI repair applications. For example, hemisectioned chronic severe SCI in dogs was treated with a hydrogel-lipid microtube based delivery system of chABC combined with trehalose⁴², TS-ChABC. Trehalose was found to stabilize chABC activity at 37 °C but the mechanisms are not well known³². The thermal stabilization of chABC demonstrated: sustained drug delivery, CSPG inhibition, improvements in locomotor function in dogs with chronic severe SCI, and some sensory recovery, which increased if chABC and NT3 were combined. The chABC long-distance diffusion required into the injured human spinal cord could be a limitation. Generally, chABC is administrated continuously by invasive pumps implanted *in vivo* but TS-chABC via hydrogel-microtube system could be a less invasive option.

Lipid microtubes associated with different axonal growth cones factors (Cdc42, Rac,1, and BDNF) were also coupled with agarose hydrogel by Jain et al.⁶³. In a dorsal over-hemisection lesion, the treated rats showed a reduced number of reactive astrocytes in the injured area, a reduced CSPG deposition, the presence of neurofilaments across the lesion, and a higher percentage of axons in the CSPG-rich regions. The dosage of the three growth factors was not optimal for stimulating the axonal growth in the CST. Specific molecules proven to be useful in healing and regenerating the spinal cord can also be loaded in nanoparticles, which are eventually embedded in hydrogels to allow a sustained release of drugs or factors. A composite of HA and methylcellulose (MC) hydrogel with PLGA nanoparticles was used to localise the nanoparticles in the specific site of injection and for the sustained release of neurotrophic factors and inflammatory molecules suppressors (embedded in the nanoparticles).⁶⁰ The BBB score of

treated rats with a compression injury increased with respect to controls, but the inflammatory response was notable. The same composite structure was also coupled with FGF2⁶¹. Thanks to the degradation kinetics of the materials, a sustained and long-term release of FGF2 was obtained. Results showed improved angiogenesis, a decrease of the cavity volume, and proliferative lesion, but functional improvements were not recorded.

Ansorena et al.⁶² demonstrated that a composite scaffold made of alginate, fibrinogen, and PLGA microspheres increased the number of neurofilaments, gained functional recovery, and more homogeneous and dense regenerated tissues through the slow release of GDFN. However, the functional recovery in hemisectioned rats was higher with free-microsphere hydrogels.

Instead, a nanofibre-hydrogel composite was produced by mixing fragments of polycaprolactone (PCL) fibers with surface grafted maleimide (MAL) groups, and a gel of thiolated hyaluronic acid (HA-SH) and polyethylene glycol diacrylate (PEGDA)^{65,85}. The material provided mechanical support for spinal cord regeneration and a suitable porosity for cell infiltration. The spinal cord thinning because of the progressive loss of neural tissue following contusion was controlled by the presence of the composite. The authors reported a shift of M1 macrophages to M2, limited to the lesion site, possibly linked to the presence of the PCL fibres. The role of fibres needs to be further investigated, but their presence seemed to encourage neo-vascularisation and differentiation of endogenous stem cells in immature neurons.

A minimally invasive method to deliver mouse embryonic stem cell (mESC) in the injury site was studied by Wang et al.⁶⁶. They embedded an aligned electrospun nanomesh of poly (D,L-lactic acid-co-trimethyl carbonate (P(DLLA-co-TMC))) in gelatin-acrylated β -cyclodextrin (β -CD) polyethylene glycol (GCP) hydrogel, which was formed by the photo-crosslinking process. The high stretchability of this material allows it to be injected. Motor neurons derived from embryonic stem cells (MN-ESC) were also embedded in the composite. Results showed an oriented neurite growth, a dendritic development, a

decreased loss of tissue and inflammatory response, synapses formation, and motor function recovery. The material filled the injury cavity, but the degradation kinetics was not optimal.

A hydrogel of hyaluronic acid and methylcellulose enriched with PLGA microparticles and BDNF was tested in a rat transection model ⁶⁷. This material had tunable mechanical properties, gelation, and biological activity by changing the molecular weight of HA. The inflammatory response was not investigated but the scaffold improved the adaptive plasticity.

Nazemi et al. ⁶⁸ used microspheres of PLGA for the delivery of hydrophobic drugs such as the paclitaxel (PTX). PTX is an anti-cancer drug that leads to axonal growth, functional outcomes, and a reduction of the fibrotic scar when injected at the lesion site of rat's spinal cord. The microspheres loaded with PTX were included in an alginate hydrogel that interacted electrostatically and by metal-ion chelation with minocycline hydrochloride (MH). This composite showed a prolonged drug release (2 months), a decrease of the inflammation response and scar tissue, an increase of axonal regeneration, protection, and functional improvement.

1.5.3.4 Self-assembling peptides (SAP). Amphiphilic molecules can show self-assembly capacity through noncovalent interactions forming 3D structures. Amphiphile peptides (AP) can be designed alternating hydrophilic and hydrophobic amino acids or positively and negatively charged amino acids that can undergo to self-complementary assembly. For example, Yuqiao Sun et al. ⁷⁵ presented a strategy to create nanofiber hydrogels using two oppositely charged SAPs conjugated with bioactive peptides motifs such as IKVAV ⁸⁶ or RDG. The use of peptide amphiphile coupled with IKVAV in rat spinal cord transection gave many beneficial results: axon elongation, functional recovery, suppressed the progression of astrogliosis, facilitated remyelination of axons inside the lesion, regeneration of corticospinal motor and sensory fibers, increasing the number of serotonergic fibers caudal to the lesion, and decreased cells apoptosis. Unfortunately, there was a small number of regenerating dorsal column

fibers. Tysseling et al. ^{45,87} verified also the effect of IKVAV peptide conjugated with amphiphile peptide (PA) on rat spinal cord compression model with similar results. This SAP-based scaffold was first studied by Silva et al. ⁸⁶, obtaining an efficient differentiation of stem cells into neurons. PA nanofibers were also studied when displaying the heparan sulfate mimetic and laminin mimetic epitopes ⁴⁶. The *in vivo* studies showed this injectable scaffold as a valid ECM substitute after SCI. Indeed, an overall tissue integrity was obtained and the locomotor functions of the treated animals improved.

Cicognini et al. ⁴⁴ investigated the use of two SAPs B24 and biotin-LDLK12 for the treatment of a contusion injury in rats. The SAP B24 is derived from the functional motif of the bone marrow homing peptide 1 (BMHP1), whereas biotin-LDLK12 is an ionic SAP (motif: biotin-LDLKLDLKLDLK-CONH₂). At the same concentration (1.12 mM), B24 resulted in less viscous than the biotin-LDLK12, which was less permissive to water, free radicals, and immune cell infiltration than B24. Thus, Biotin-LDLK12 formed a dense scaffold after injection without diffusing within the injured tissue as opposed to B24 and showed a slower degradation rate. For these reasons, the hematoma reabsorption was faster where biotin-LDLK12 was injected (Figure 14). However, SAPs swelling caused the compression of the surrounding tissue.

Self-assembling peptide (RADA16) nanofiber containing IKVAV motif were also studied for central nervous system applications ^{88,89}. Cicognini et al. functionalized RADA 16-I to BMHP1 by using a 4-glycine bridge and observed an increase of vascularization and migration of glial precursor cells, a remodelling of the ECM with consequent decrease of cyst area ⁷⁴.

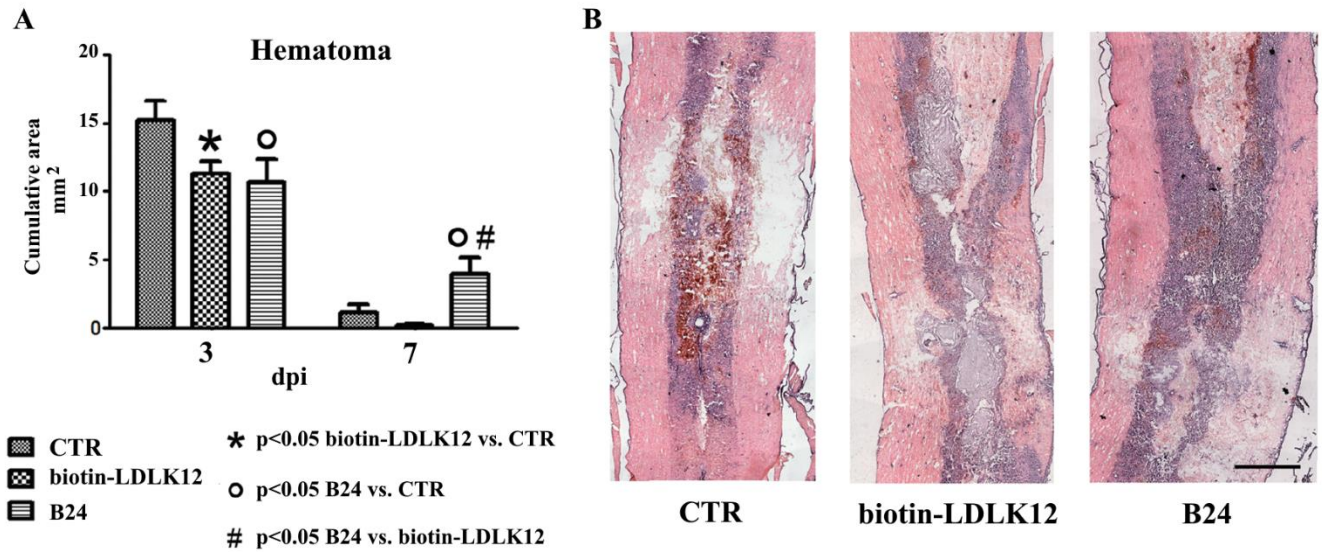


Figure 14. Quantification of hematoma. (A) At 3 day after injury (dpi) both SAP-treated groups had a significant lower leakage of red blood cells in comparison with controls. At 7 dpi biotin-LDLK12-treated animals showed the lowest content of red blood cells, while B24 the highest one. (B) Longitudinal sections stained with hematoxylin/eosin showed the presence of extravasated red blood cells (red-brownish coloured). Scale bar: 700 μ m.

Figure 14 reproduced with permission from ref 74. Copyright 2014 American Scientific Publishers.

Tran et al.⁷³, investigated instead the use of pH-responsive self-assembly hydrogel, RADA-16I (Ac-RADA₄-CONH₂), to primarily provide a favourable environment for capillary formation. Indeed, the damage of the blood spinal barrier (BSCB) causes inflammation and glial scar formation that inhibit tissue regeneration. The results showed the presence of microvessels from $9.0 \pm 3.1 \mu$ m to $100 \pm 46 \mu$ m within the RADA-161 hydrogel, depending on the cell density condition. The formation of the BSCB within the RADA-161 hydrogel reduced inflammatory response and scar formation and increased axon

infiltration into the SCI site. An improvement of this system could be the control of microvessels orientation because the axon growth specifically in the rostral-caudal direction could be essential for SCI treatment. Arginine-alanine-acid aspartic-alanine (RADA)4 SAP was also used by Tavakol et al. ⁷⁰ in combination with IKVAV or with a longer laminin motif (CQAASIKVAV (CQIK)) ⁷⁰ to form a hydrogel-based material with nanofiber structure. CQIK resulted in improved cellular response compared to IKVAV peptide due to the greater similarity to the laminin active site. In both cases, it was observed neurite outgrowth, myelination, and inhibited astrogliosis. The locomotor recovery was significantly less than (RADA)4 combined with bone marrow homing peptides (BMHP).

Ye et al. ⁷² cultured isolated primate NSCs in polypeptide RADA16 (AcN-RADARADARADARADA-CN₂) that can be assembled at physiological pH. The *in vivo* tests on the rat compression model showed differentiation of NSCs to neurons, oligodendrocytes and astrocytes, myelin production, and motor function recovery.

A type of SAP used to minimize SCI damages is also represented by K2(QL)6K2 or QL6 ⁷¹. It is characterized by alternating ionic hydrophilic and hydrophobic amino acids that self-assembly into beta-sheet at physiological pH. After the acute stage, QL6 was injected into the center of the lesion, whereas the neural precursor cells (NPC) into adjacent dorsal columns. The cell survival is promoted by continuous subdural administration of growth factors through an osmotic micropump for 7 days. The presence of the scaffold improved the inhibitory environment, reducing the scar tissue and the inflammation with consequent cell survival and differentiation up to functional recovery.

Amphiphilic peptides (CH₃(CH₂)₁₄CO-AAAAGGGEIKVAVPA) functionalized with the laminin motif IKVAV were investigated by Hassannejad et al. ⁴³ in order to produce an injectable hydrogel for a sustained release (21 days) of brain-derived neurotrophic factor (BDNF). This latter neuroprotective protein-enhanced neurite outgrowth from the dorsal root ganglion (DRG) explants and the presence of

the hydrogel resulted in considerable axon preservation at 6 weeks post-injury. The functional recovery was not statistically significant between IKVAV-PA hydrogel injected and saline-injected animals.

1.5.4. Spinal cord injury models

Different types of trauma can be simulated *in vivo*, generally on the spinal cord of adult rats. These injuries are contusions, compressions, hemisections, or complete sections of the spinal cord and they are performed following standard protocols to obtain reproducible results.

1.5.4.1 Severe and moderate contusion model. A reproducible contusion model on rat spinal cord via the weight-dropping method could be performed by using a stereotactic frame and computer-controlled impactor. A severe contusion is, generally, caused by an impactor tip of 3.0 mm at a speed of 4 cm/s with a depth of 2 mm and a dwell time of 0.3 sec towards an exposed and well stabilized spinal cord surface⁹⁰⁻⁹². A severe contusion induce the highest gray matter losing, few white matter sparing, and biochemical changes such as free radicals, prostaglandins, calcium-activated proteases, loss of myelin proteins⁹³, extracellular potassium and calcium concentrations changes. Blight and Decrescito (1986)⁹⁴ had observed that large myelinated axons are more damaged at the nodes of Ranvier than the axons closest to the pial surface. Damaged axons caused calcium entry through tetrodotoxin-sensitive channels and consequent secondary reactions due to the calcium entry^{95, 96}. A moderate contusion model, instead, preserves most of the ventral and ventral-lateral descending pathways that led to post-injury locomotor recovery in both trained and untrained animals¹⁴.

Mechanical disruption via weight-dropping method was universally accepted to be clinically relevant^{90,91}, because it simulates human contusion due to their ability to mimic both primary mechanical damage and secondary reactive phase of injury.

1.5.4.2 Compression model. The compression is generally induced by an aneurysm clip closed around the exposed spinal cord of rats for 1 min until the generation of an extradural compression of 30 xg pressure. This model also simulates clinical conditions observed in several human cases but causes moderately severe acute compression injury ⁹⁷.

1.5.4.3 Unilateral and hemisection model. The unilateral and hemisection of the spinal cord simulate an injury clinically observed in human cases and allow to compare injured and healthy fibers in the same animal ⁹⁰ but shows disadvantages concerning model uniformity ⁹⁸.

1.5.4.4 Complete model. The complete spinal cord injury model is generally performed at the T9-T10 segment and a gap of 2 or 4 mm allows the insertion of the scaffold ⁷⁶. The complete transection interrupts axon fibers and propriospinal neurons resulting in permanent paralysis. This model is considered by many researchers as the gold standard for validating axonal regeneration but it is not clinically relevant and it shows high variability in the results ^{98,91}.

1.5.5. Severe contusion model as the new gold standard: how?

During the past decade, the complete transection SCI model has been used for validating axonal regeneration but this model is far from a real case of human spinal cord injury ^{99,90,95}. A contusion model, instead, reflects a traumatic human SCI but it is unsuitable for validating axonal regeneration because it is difficult to discriminate the contribution of the scaffold to the axonal regeneration from the spontaneous regeneration of the tissue ^{90,98}. Thus, matching a reproducible and reliable axonal regeneration with the use of a realistic SCI model is still a challenge. Some researchers proposed studies based on the contusion model to have clinical relevance (as described above) and *in vitro* models to obtain reliable results on the neuronal regeneration.

The commonly used *in vitro* cell culture models of SCI include i) primary isolated neurons, oligodendrocytes, astrocytes, or microglia cells; ii) co-culture of neuronal cells with different cell types, which are present in the glial scar; iii) co-cultivation with meningeal cells in *in vitro* scar formation model, called scratch model; iv) rat spinal cord cells onto a confluent monolayer of neurosphere derived astrocytes for investigating the CNS axonal myelination; v) neurite outgrowth assays for the phenotypic expression of regeneration progress ¹⁰⁰.

However, the *in vitro* evaluation lacks the complexity and physiological relevance of *in vivo* system but the results are reliable and reproducible. Unfortunately, animal studies offer complexity, which is very difficult to model *in vitro*, and high variability, which prevents reproducible studies ^{101,102}. For this reason, organotypic cultures of spinal cord explants could be an option to obtain reproducible results after a contusion injury ^{100,103}. The spinal cord explants are cut to obtain slices, called organotypic slices (OTSs), that preserve the basic structural and connective organization of their original tissue (organotypic). OTSs represent an interim system sharing the properties of the cell culture *in vitro* and an animal *in vivo* model. Organotypic spinal cord slice (OTS-SC) are generally cultivated on a semi-porous membrane at the air-medium interface to allow nutrition and gas exchanges, under appropriate conditions the slices can survive for a week to months ¹⁰⁰.

The OTS-SC model is suitable for axonal growth evaluation because the typical ventrodorsal polarity of the SC is maintained after a culture period of 2 weeks, and intrinsic spinal cord axons formed a strong fiber tract extending along the longitudinal axis of the slice ^{100,103} (Figure 15).

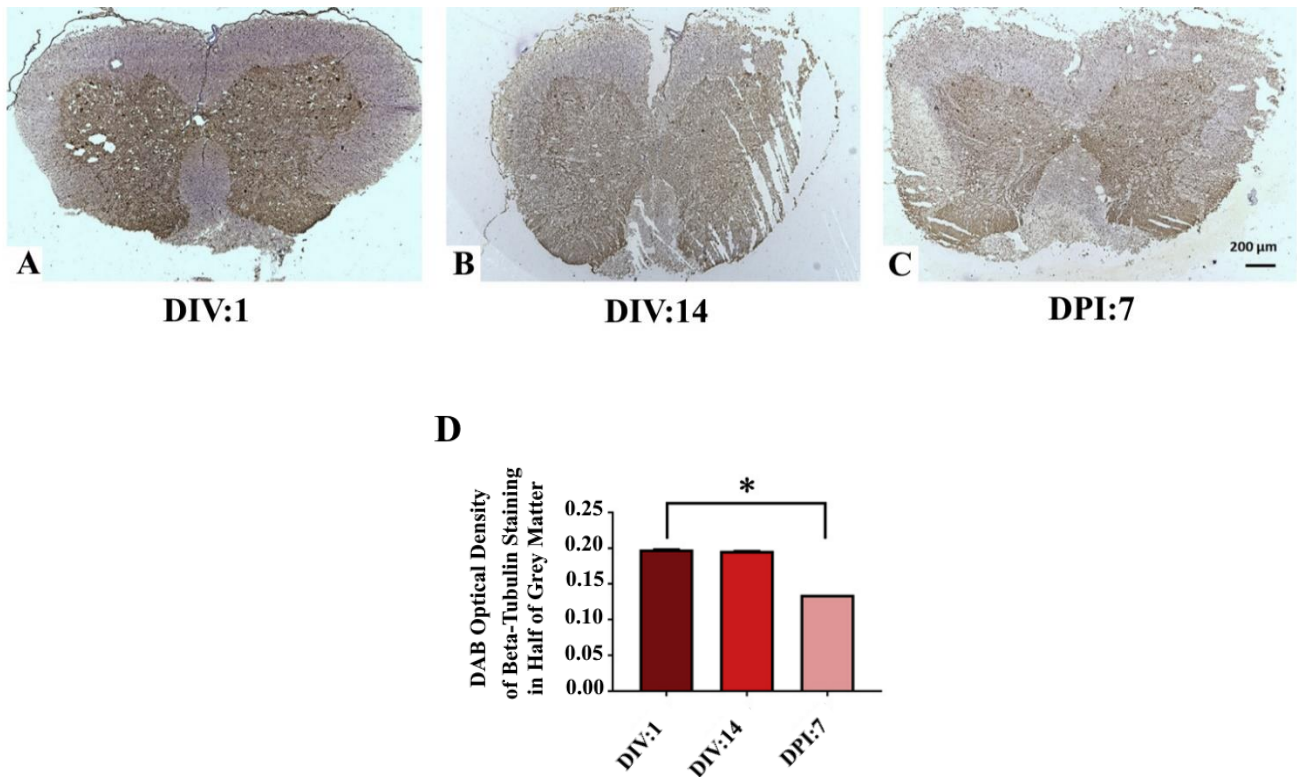


Figure 15. The first day of OTS-SC culture (A) is compared with the slice observed seven days after injury (DPI:7) (B) and its uninjured counterpart (DIV:14) (C). The first day of OTS-SC culture (A) is compared with the slice observed seven days after injury (DPI:7) (B) and its uninjured counterpart (DIV:14) (C). In the diagram (D) is reported the expression of β III Tubulin in spinal cord slices

Figure 15 reproduced with permission from ref 103. Copyright 2019 Elsevier.

A well defined *in vitro* evaluation could contribute to understanding the results of *in vivo* analysis, for example, Basso, Beattie, and Bresnahan locomotor score (BBB), ladder climbing test, electrophysiological recordings such as the rate-dependent depression (RDD) of the Hoffmann's reflex (H-reflex), defined as “the decrease in reflex magnitude relative to repetition rate”¹⁴, suitable for evaluating sensorimotor improvements and spasticity. Moreover, this model could highlight the real

contribution to the neuroregeneration of the material implanted, because the mechanism leading to post-lesional adaptive plasticity might be avoided^{14,63,103}. Mechanical disruption via weight-dropping was also tested on OTSs¹⁰³. The results confirmed the use of this model as a simulation of a human contusion due to their ability to mimic both primary mechanical damage and the pathophysiological mechanisms after SCI. However, OTSs are harvested from animals and their treatment is expensive and time consuming^{100,105}. These few limitations allow the use of OTS as a relevant platform before *in-vivo* testing^{103,106}.

The validation of injectable biomaterials for an eventual advanced therapy medical product (ATMP) or medical device passes through different levels, including a period of nonclinical and pre-clinical research studies, involving parametric data collection and analysis in well-defined systems¹⁰⁷. In the future, we will need to establish high throughput test platforms for biomaterials, that comprise standardised testing protocols for *ex vivo*, *in vivo*, pre-clinical, and clinical testing. In the case of the SCI contusion model, there is a standardised method to elicit the lesion^{90,91,95,108} but the effects of biomaterials are not completely understood once tested *in vivo* due to the high neural tissue complexity. To reach the application of biomaterials on patients, OTC-SC or 3D neural cell culture models could be used to validate the results obtained from BBB locomotor score, ladder climbing test, electrophysiological recordings and acquire reliable data in well-defined system.

1.5.6. Conclusions

Non-invasive materials for SCI treatments have gained interest due to their in situ safe procedure of administration, which might be done more than once until the complete ECM formation. Repetitive injections, still now, are expected just for cell therapy, failing the cooperation with supporting materials.

Future studies might be focused on the optimization of injectable material production such as i) swelling control, which may cause secondary damages, ii) use of non-toxic crosslinkers, iii) gradients applied on the deposited scaffold to induce a growth directionality, iv) more precise mimicking of the ECM composition and mechanical properties; v) combination of multiple fabrication methods, vi) control of the 3 D structure, vii) non-invasive electrical stimulation.

These non-invasive systems are generally injected during the sub-acute stage, when the injured site is characterized by a cystic cavity surrounded by a glial scar of ECM material, macrophages, cell, and inhibitory debris and a spontaneous regeneration process begins. *In vivo* models show the variability of outcomes even if the defects are standardized. Moreover, the SCI pathology in this model is sensibly different from humans, and the regeneration shows distinct differences in terms of axon elongation and mechanisms of sprouting ⁴⁷. Thus, *in vivo* results could be accompanied by *ex vivo* validation such as OTC-SC after compression model or 3D neural cell culture models that might give more reliable data. Clinical trials are difficult to reach mainly due to the high cost and variability of *in vivo* testing and the complexity of the biological environment where materials are tested.

Chapter 2

Experimental studies

In the following paragraph the synthesis and characterization of a bioinspired multifunctionalized silk fibroin (BMS), is described (Published in ACS Biomaterials Science and Engineering, 2021, 7, 2, 507–516).

2.1 A bio-inspired multi-functionalized silk fibroin (BMS)

Sofia Santi^{# +}, Ines Mancini[§], Sandra Dirè^{# ‡}, Emanuela Callone^{# ‡}, Giorgio Speranza^{# & †}, Nicola

Pugno^{§ ¶}, Claudio Migliaresi^{# +}, Antonella Motta^{# +}*

Department of Industrial Engineering, University of Trento, via Sommarive 9, Trento, Italy

+ BIOTech Research Center, University of Trento, via delle Regole 101, Trento, Italy

§ Laboratory of Bioorganic Chemistry, Department of Physics, University of Trento, via Sommarive
14, 38123 Trento, Italy

‡ “Klaus Mueller” Magnetic Resonance Laboratory, Department of Industrial Engineering,

University of Trento, Via Sommarive 9, 38123 Trento, Italy

& FBK-irst, Via Sommarive 18, 38123 Povo-Trento, Italy

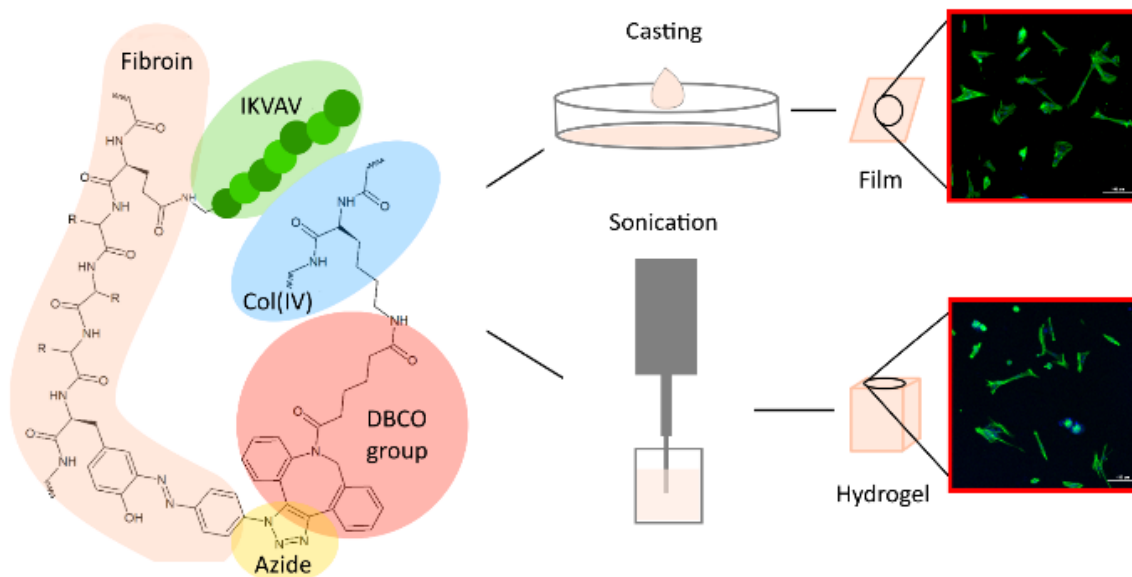
† IFN - CNR, CSMFO Lab. & FBK CMM, via alla Cascata 56/C Povo, 38123 Trento, Italy

[§] Laboratory of Bio-Inspired, Bionic, Nano, Meta Materials & Mechanics, Department of Civil,
Environmental and Mechanical Engineering, University of Trento, 38123 Trento, Italy

[✉] School of Engineering and Materials Science, Queen Mary University of London, Mile End Road,
E1-4NS London, United Kingdom

*Corresponding author: antonella.motta@unitn.it

Graphical abstract



KEYWORDS: silk fibroin, laminin peptide, chemical modification, tissue regeneration, biomimetic.

ABSTRACT

A bio-inspired multi-functionalized silk fibroin (BMS) was synthesized in order to mimic the interaction of Nidogen with type IV Collagen and Laminin of basement membranes. The designed BMS consists of a motif of Laminin α -chain derived, called IK peptide, and type IV Collagen covalently bound to the silk fibroin by using EDC/NHS coupling and a Cu-free click chemistry reaction respectively. Silk fibroin was chosen as the main component of the BMS because it is versatile and biocompatible, induces an *in vivo* favorable bioresponse and moreover can be functionalized with different methods. The chemical structure of BMS was analyzed by using XPS, ATR-FTIR, CP MAS NMR techniques, and colorimetric assay. The SF and BMS solution were crosslinked by sonication to form hydrogels or casted to make films, in order to evaluate and compare the effectiveness of adhesion similarly to the basement membrane seeding fibroblast cell line (MRC5). BMS hydrogels were also characterized by rheological and thermal analyses. This component will be very important for the production of the adhesive patch described in the previous section and later in the thesis will be discussed the biological effect of BMS hydrogel on human neural stem cells (hNSC) and its piezoelectric properties compared with the unmodified SF.

2.1.1. Introduction

The use of silk fibroin for the fabrication of biomedical prostheses and tissue engineering scaffolds has been widely investigated in the last years. The molecular structure of the silk fibroin, i.e. the protein composing the core part of the silkworm filament, consists of a light chain ($M_w \sim 26$ kDa) and a heavy chain ($M_w \sim 350$ kDa) linked together by a disulphide bond. The hydrophilic groups are mainly present in the light chain, whereas the heavy chain has a primary structure formed by repetitive sequences of

GAGAGS, GAGAGY and GAGAGVGY mainly hydrophobic that interact with each other ¹⁰⁹. The aminoacidic sequence of fibroin, and the presence along the chain of RGD-like sequences, are considered the main reasons for the favourable interactions that fibroin materials possess with cells and biological environment ^{110–113}. Moreover, fibroin can be chemically conjugated with active peptides in order to achieve specific biological performances for selected applications.

Tissue engineering fixes the objective to produce cells supportive matrices in order to induce the regeneration of damaged tissues and organs. In general, the closer the scaffold is in terms of composition, morphology and properties to the extracellular matrix (ECM), the faster and more effective the regeneration process will be.

The basement membrane (BM) is a sheet-like thin extracellular matrix that is essential for animal development. BM mainly consists of laminin and type IV Collagen, Col(IV), interrelated with nidogen, perlecan and other molecules. It has several actions providing biochemical and mechanical signalling to cells and facilitating intercellular and intracellular interactions, modulating cell behaviour and regulating tissue development, function and repair ^{114, 115}.

The BM marks the paths for cells migration and works as a charge-selective filtration barrier due to its net negative charge, regulating the passage of negative molecules from the blood stream to tissues ^{116, 117}. It is also a structural support for tissue, body cavity walls development and performs an important role during the neural tissue remodelling promoting synaptogenesis and myelination of nerves ^{118, 119}.

The mimesis of the composition, structure and functionality of BM is still a challenge.

Previous studies reported the conjugation of laminin in different hydrogels based on collagen type I, hyaluronic acid, alginate or polyacrylamide gels (PA), failing in inducing the cooperation with Col(IV) ^{120–122}. In other cases ^{23, 123}, blends of laminin and Col(IV) have been made. Worth nothing is the fact that

changes in the hydrogel's composition could negatively affect the cell behaviour. For example, the loss of Col(IV) that is associated to the breakdown of the BM, can start tumour invasion and metastases¹²⁴.

In this work silk fibroin was functionalized with IKVAV peptide (IK), belonging to the α -chain of laminin that is involved in cell adhesion, migration and differentiation, and covalently bound to Col(IV), in order to mimic the composition of the BM¹¹⁵.

The laminin peptide and the Col(IV) were attached on the same silk fibroin molecule to allow the interaction of the main components of BM, otherwise auto-assembly phenomena could be preferentially promoted¹¹⁷.

The synthesis was conducted by using the 1-Ethyl-3-(3-Dimethylaminopropyl) Carbodiimide in combination with N-hydroxysuccinimide (EDC/NHS method) and a Strain-Promoted Azide-Alkyne Cycloaddition reaction (SPAAC), also termed as the Cu-free click reaction, that occurs spontaneously in water. In particular, the EDC/NHS reaction was used to bind IK to the glutamic and aspartic acid residues, which represent the 3.3% mol of SF¹²⁵. The Col(IV), instead, was bound to the silk fibroin chain by the Cu-free click reaction producing a triazole ring by cycloaddition. For this conjugation, the tyrosine groups (which represent the 5.2-5.5% mol of SF)¹²⁶ were functionalized with a diazonium coupling reaction that produced the Azide SF precursor. On the other hand, the Col(IV) was modified by adding an alkyne-derived, namely dibenzocyclooctyne-sulfo-N-hydroxysuccinimidyl ester (DBCO-NHS), producing the Col(IV)/DBCO precursor.

The synthetic sequence to produce BMS can be summarized in three steps: i) production of the Azide SF and Col(IV)/DBCO precursors, ii) coupling reaction of the Azide SF with IK by EDC/NHS method to form the precursor "Azide SF-IK" and finally iii) conjugation of Azide SF-IK with Col(IV)/DBCO by using the SPAAC reaction to form the target BMS (Figure 16). All the reactions occur in aqueous solution.

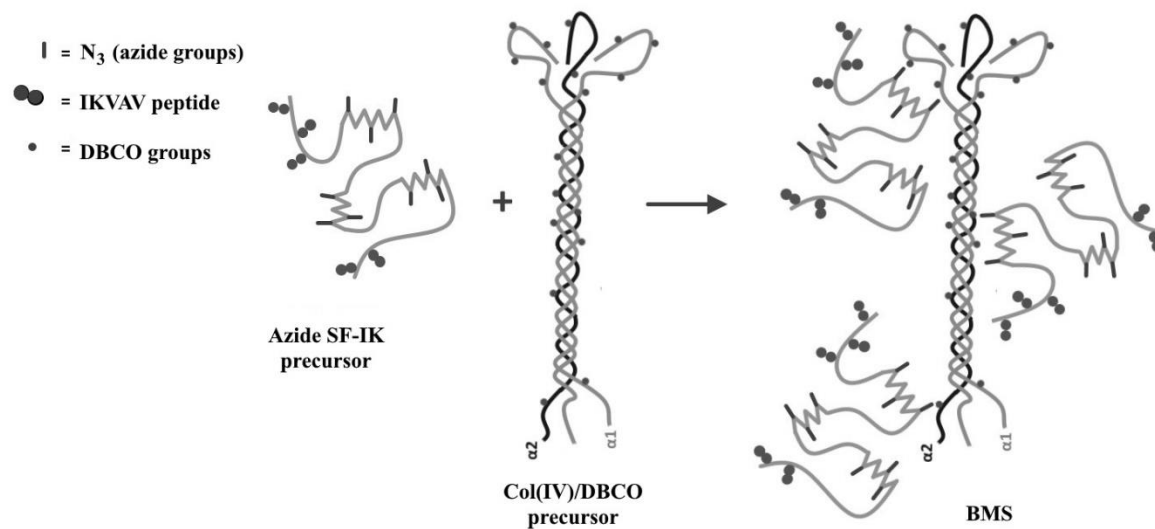


Figure 16. Structure design of Azide SF-IK, Col(IV)/DBCO and of the bio-inspired multi-functionalized silk fibroin (BMS). The BMS is formed after the click reaction between the precursors.

The conversion of the reactions was verified by using qualitative and quantitative analyses. The BMS solution was gelled by sonication and the hydrogel properties were characterized by thermal analysis and rheological measurements in comparison with a silk fibroin hydrogel. The SF and BMS solution were also casted to make films that underwent to biological analyses to determine the effect of the functionalization on the early adhesion and viability of human embryonic lung fibroblast cell line (MRC5).

2.1.2 Materials and Methods

The following chemical have been used: N-(3-dimethylaminopropyl)-N'-ethylcarbodiimide hydrochloride (EDC), N-hydroxy-sulfosuccinimide sodium salt (NHS), 4-azidoaniline hydrochloride, p-toluenesulfonic acid mono-hydrate, collagen from human placenta (collagen IV), dibenzocyclooctyne-sulfo-N-hydroxysuccinimidyl ester (DBCO-NHS), sodium nitrite, acetonitrile, 2,4,6-trinitrobenzene sulfonic acid (TNBS) (Sigma Aldrich), laminin A chain (CliniSciences), MRC5 (human embryonic lung fibroblast cell line, ATCC-CCL-171), MEM (Minimum essential medium), fetal bovine serum (FBS), sodium pyruvate, L-glutamine 2 mM, antibiotic/antimycotic, non-essential amino acids, rhodamine-phalloidin and 4' 6-diamidino-2-phenylindole (DAPI) (Thermo Fisher Scientific).

The multi-functionalization of silk fibroin was performed through the following consecutive steps:

- i) Preparation of a SF solution in water
- ii) Functionalization of the SF with azide groups by a diazonium coupling reaction (Azide SF)
- iii) Coupling of the Azide SF with the IK peptide (Azide SF-IK)
- iv) Production of the Col(IV)/DBCO precursor
- v) Synthesis of the bio-inspired multi-functionalized silk fibroin (BMS)

The single steps are described in the following.

- i) **Silk fibroin solution preparation.** *Bombyx mori* cocoons (purchased from Chul Thai SilkCo., Phetchabun, Thailand)¹²⁷ were degummed by treating twice with Na₂CO₃ aqueous solution (1.1g/L) at 98 °C (one hour and a half for each treatment) and rinsed with distilled water. The degummed silk fibroin was dissolved in 9.3M LiBr solution (1g/10 mL) at 65 °C for 4 h. The solution was dialyzed in a Slide-A-Lyzer Cassette (ThermoScientific), MWCO 3500 Da, against distilled water for 3 days.

- ii) Diazonium coupling reaction.** The functionalization of silk fibroin with azide groups (Azide SF) was performed as follows. Solutions of 4-azidoaniline hydrochloride (0.35 μmol) in 0.5 mL of a 1:1 acetonitrile/water solution, of p-toluenesulfonic acid monohydrate (1.2 μmol) in 0.25 mL of water, and of sodium nitrite (0.7 μmol) in 0.25 mL of water were initially prepared in an ice bath. At this stage, a nitrosation of primary aromatic amines occurs with nitrous acid, which is generated in situ from sodium nitrite and the strong acid. The diazonium salts solution was added to 2 mL of 3% SF borate solution buffered pH 9.2 (100 mM sodium tetraborate and 150 mM NaCl dissolved in deionized water)¹²⁶. The reaction was carried out under stirring for 30 min at room temperature, and the resulting yellowish solution was finally dialyzed against phosphate buffer saline at pH 6 for 1 day by using a SPECTRA/POR dialysis tubing, cut off 12/14 KDa. The final concentration of Azide/SF resulted to be 3% w/v, as estimated by Thermo ScientificTM NanodropTM 1000 spectrophotometer (ND-1000).
- iii) Azide SF with IK peptide functionalization (Azide SF-IK).** The above indicated solution (2 mL) was mixed with 12 mg of EDC and 7.2 mg of NHS for 20 min at room temperature (RT) under gentle stirring. After 20 min the activated protein was purified by gel filtration using a desalting resin (ZebaTM Desalting Chromatography Cartridges)¹²⁸. After purification, the activated protein solution was added drop by drop to a phosphate solution buffered at pH 7.4 containing 50 μL of IK peptide (2 mg/mL) and left to react for 2 h under stirring at RT. The excess reactants were removed by desalting with a MWCO 7 KDa column.
- iv) Col(IV)/DBCO precursor production.** The Col(IV)/DBCO precursor was prepared by reacting 2 μL of DBCO-NHS ester /PBS solution (50 mg/mL, pH 7.4) with 0.2 mL of Col(IV) (2.0 mg/mL, pH 7.4) for 2h at 4°C. The resulting solution was purified by overnight dialysis at

4 °C versus deionized water (ddw) by using a Slide-A-Lyzer Cassette (ThermoScientific) dialysis cassette MWCO 3.5 kDa.

- v) **Synthesis of the biomimetic multi-functionalized silk fibroin (BMS).** The BMS was obtained combining 1 mL of 3% Azide SF-IK solution with 50 µg of Col(IV)/DBCO precursor. Thus, the weight ratio between Azide SF-IK and Col(IV)/DBCO precursor was 600:1. The reaction occurred in 30 min at RT through a SPAAC reaction to obtain a final solution of 2% of BMS in water. For further steps the solution has been concentrated by dialysis against polyethylene glycol to 3% w/v. The efficiency of the Col(IV) reaction has been evaluated by spectroscopic analysis.

Hydrogel preparation. BMS and SF water solutions, both at 3% w/v concentrations were sonicated by using the Hielscher Ultrasound UP400S for 1'30'' at 50% of amplitude. Gelation occurred approximately after 1 h at 37°C.

Films preparation. BMS and SF water solutions, both at 3% w/v concentrations were casted in a 24 well-dish. After drying, the films were stabilized by methanol 80% for 10 min and washed with water three times.

Determination of free-amino groups. Free-amino groups have been evaluated by using 2,4,6-trinitrobenzene sulfonic acid (TNBS) method. Dynamic light scattering (DLS) measurements were also performed to verify the formation of aggregates, mainly in SF solutions, that prevent from exposing the free amino groups. The content of free-amino groups (FAC) in Col(IV) and Col(IV)/DBCO was determined by using the TNBS method^{129,130} as follows: 150 µL of 0.02% (w/v) TNBS solution, prepared in a buffer of 0.1 M of sodium bicarbonate (NaHCO₃) pH 8.5, was mixed with 300 µL of each sample (0.2 mg/mL) also buffered at pH 8.5 by dialysis and heated at 40°C for 2h. The protein concentration

was confirmed by thermogravimetric analysis (TGA). After 2 h, 150 μL of 10% of SDS and 75 μL of 1N HCl was added to block the reaction. Instead, the SF and its derivatives FAC content were determined with slight changes from the above procedure to avoid gelation of fibroin. Each sample (100 μL) was poured in a 96 well plate and the absorbance measured at 418 nm by using a microplate reader (Tecan Infinite M200). The FAC of each sample was estimated from a calibration curve of β -alanine (MW: 89.09 Da) solution in 0.1M sodium bicarbonate in the range $0.5 \cdot 10^{-3} \text{ M} - 1.7 \cdot 10^{-5} \text{ M}$.

Evolution in time of SF aggregates in solution. DLS analysis was used in order to evaluate possible aggregations phenomena in the SF solution, that could affect the absorption data acquired during the TNBS detection¹³¹, by using a Zetasizer, Malvern Nano series. The setting parameters were fixed as follows: 15 runs of 10 s each sample, equilibration time of 120 s at RT, Silk Fibroin RI=1,543; Ab=0,01 dispersed in water.

Chemical composition characterization by X-ray photoelectron spectroscopy (XPS). A drop of SF and another one of BMS solutions were left to dry separately on a glass support and analyzed by using an Axis DLD Ultra analyzer from Kratos (UK-Manchester). The core lines of interest were acquired at a higher energy resolution using a pass energy of 20 eV with a charge compensation, being the samples non-conductive. Data reduction was performed using a made in house software¹³² based on the R platform software.

Secondary structure characterization by ATR-FTIR spectroscopy. All SF-based compounds solutions and their respective hydrogels were freeze-dried and the secondary structures were analyzed by infrared spectroscopy using an instrument working in attenuated total internal reflection mode equipped with a zinc selenide crystal (ATR-FTIR, Bruker Tensor 27). Each spectrum was the mean of 128 acquisitions (in the region 4000 and 400 cm^{-1}) with a 4 cm^{-1} spectral resolution. Spectral analysis was performed using OriginPro 2017.

Solid-state nuclear magnetic resonance (NMR) spectroscopy. Nuclear magnetic resonance spectroscopy was conducted on SF, Azide SF, Azide SF-IK, BMS lyophilized solutions. The test analyses were performed on ^{13}C nuclei by using a Bruker 400WB spectrometer (Bruker Corporation, Billerica, MA USA) with a proton frequency of 400.13 MHz. The spectra were acquired with cross-polarization sequence under the following conditions: ^{13}C frequency: 100.48 MHz, contact time 2000 μs , decoupling length 6.3 μs , recycle delay 5 s, 41k scans. Samples were packed in 4 mm zirconia rotors, which were spun at 7 kHz under air flow. Adamantane CH_2 resonance at 38.5 ppm was used as external secondary reference¹³³. All the spectra were normalized on the $\text{C}\beta$ resonance of SF Ala (δ around 17.3 ppm) because the Ala amino acids of IK peptide and Col(IV) contribute negligibly to the signal.

Differential scanning calorimetry (DSC). Differential scanning calorimetry (DSC) was performed on about 1 mg of SF, Azide SF, Azide SF-IK, BMS (SF IK/Col(IV)) lyophilized hydrogels, and Col(IV) and 0.2 mg 4-azidoaniline hydrochloride (source of azide groups introduced in the SF). Samples were analyzed in punched crucible in a temperature modulated DSC Q20 calorimeter (TA Instrument), from 20 to 320°C at 3 °C/min, under fluxing nitrogen, with a modulation period of 40 s and a modulation amplitude of $\pm 0.5^\circ\text{C}$. Glass transition (T_g), degradation temperatures (T_d) and specific endothermic heat (ΔH) of each sample were determined.

Thermogravimetric analysis (TGA). TGA analysis was conducted in a Mettler TG50 thermobalance, on about 100 mg of water equilibrated BMS hydrogels in comparison to SF, with nitrogen flowing at 100 mL \cdot min⁻¹, at a heating rate of 10 K \cdot min⁻¹, in the range 30–250 °C.

Rheology. The rheological characterization of SF and BMS hydrogels was done with a Discovery HR-2 hybrid rheometer, in dynamic mode, on disc samples in triplicate (diameter 3 cm, height 3.1 mm). The strain sweep was set in the range of 1-100 Hz, with a strain of 5%.

Biological evaluation. MRC5 were cultured in the following medium composition: MEM (Minimum essential medium) 87%, fetal bovine serum 10%, sodium pyruvate 1%, L-glutamine 2 mM 1%, antibiotic/antimycotic 1%, non-essential amino acids 1%. The cells were cultured in T-75 cell culture flasks (Corning, New York) at standard culture conditions of 37°C, and 5% carbon dioxide. Cell adhesion and spreading were studied on hydrogels and films of modified and unmodified silk fibroin. The films were sterilized by using 70% ethanol for 30 min and washed three times with sterilized water, whereas hydrogels were produced sterilizing the solutions by using a 0.22 µm filter and sonicating to induce gelation into a 24 well dish. The samples were produced in triplicate for the adhesion test and in quadruplicate for evaluating the cell viability.

- **Adhesion test.** The samples were incubated at 37°C, 5% CO₂ for three time points (1-3-7 days). After each time point, the samples were washed with PBS and the cells were fixed with 4% paraformaldehyde in PBS for 30 minutes. The samples were washed again with PBS and permeabilized with 0.1% Triton-X100 in PBS for 30 minutes. After a further washing in PBS, the cells were then treated for 30 minutes in a dark environment, firstly, with rhodamine-phalloidin to detect the cytoskeleton, and with DAPI to counterstain the nuclei of the cells. They were imaged using a Nikon TE2000-S fluorescent microscope (Melville, New York). Unmodified SF hydrogel were used as control.
- **Cell viability.** At each time point (day 1-3-7) the culture medium was replaced with medium containing Alamar Blue (10% v/v) and data were recorded after around 3 hours of incubation at 37°C by using a microplate reader setting the absorbance at 535 nm and the emission at 590 nm.
- **Cell counting.** The number of cells was determined by 4',6-diamidino-2-phenylindole (DAPI) fluorescence staining and counted by ImageJ software on different visual fields of (1.5 *1.5 mm) selected randomly.

2.1.3 Results and Discussion

Synthesis of the biomimetic multi-functionalized silk fibroin macromolecules (BMS)

Figure 17 illustrates the synthesis of BMS.

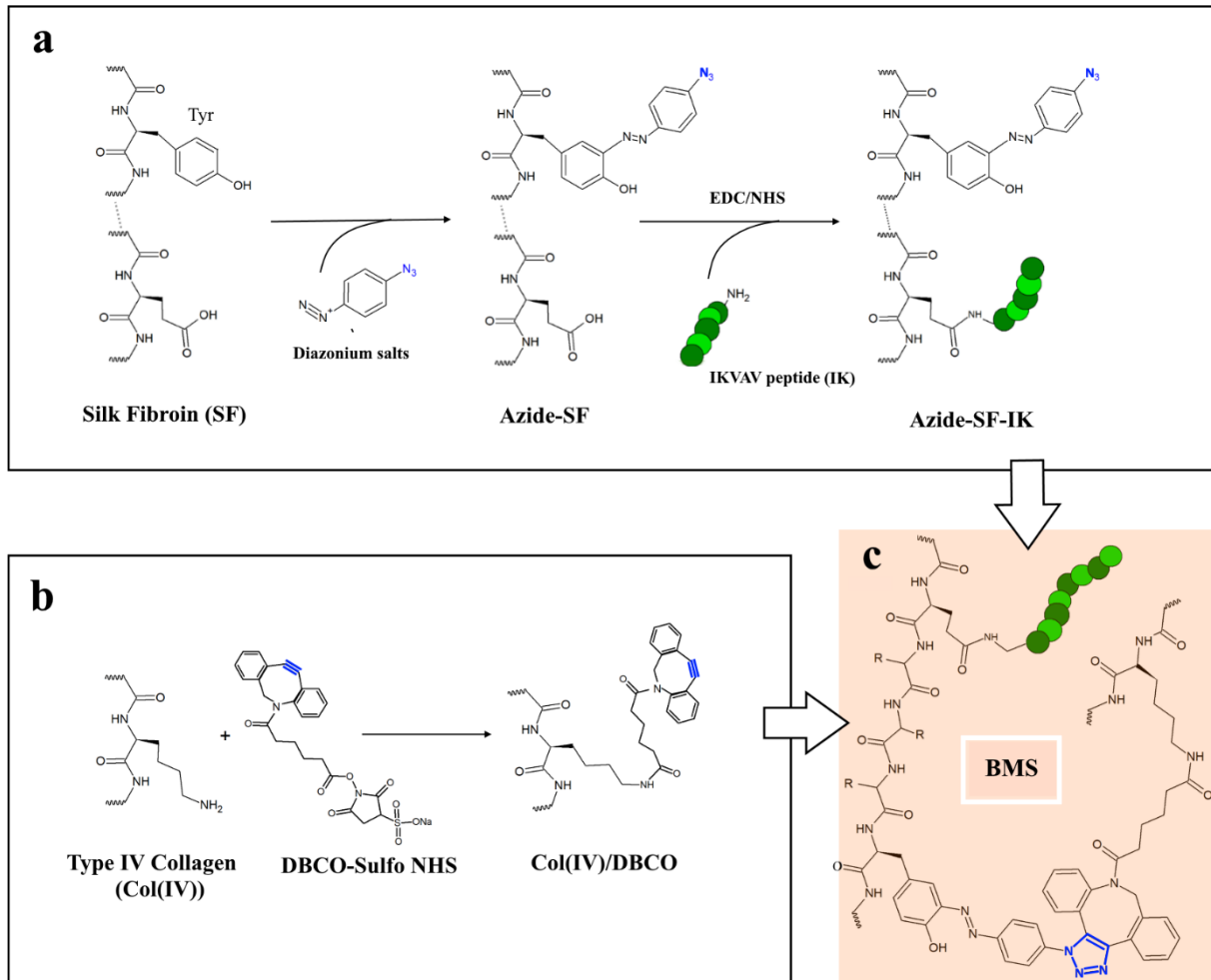


Figure 17. Synthetic sequence to obtain the biomimetic multi-functionalized silk fibroin (BMS): a) conjugation of the Azide terminated SF with IK; b) Formation of the “Col(IV)/DBCO” precursor; c) Reaction between Azide SF-IK and Col(IV)/DBCO to form the multi-functionalized silk fibroin (BMS).

The reactions were monitored by the TNBS assay. The FAC of SF conjugated with IK peptide was compared with SF that follows the same steps of the reaction without adding the peptide (the SF is subject to ageing during the dialysis as confirmed by DLS analysis) (Supporting information). The results show an increase of $0.3 \cdot 10^{-4}$ M of free amines in SF-IK compared to the SF (Supporting information).

Instead, the Col(IV)/DBCO precursor shows a decrease of free-amines of about 52% compared to Col(IV), a value which reveals the efficiency of the reaction (Supporting information).

^{13}C CPMAS NMR was performed to detect chemical shifts, line shapes and any possible structural conformation changes during the functionalization. The spectra showed in [Figure 18](#) reveal a slight increase in the intensity of the carbonyl peak and the methylene resonances of Ala, Ser and Tyr with the peptide addition. In particular, the increase of the carbonyl peak (δ around 172.7 ppm) might refer to Ser/Gln/Asp of the IK peptide added. Instead, the peak of SF carbonyl groups (δ around 56.1 ppm)¹³⁴ results higher than BMS because the presence of Ser/Tyr in SF molecule, whereas, the peak of carbonyl/carboxylic groups (δ around 172.7 ppm)¹³⁵ of BMS is higher than SF because the presence of Asn/Gln/Asp/Glu aminoacids in BMS after the conjugation of the Col(IV).

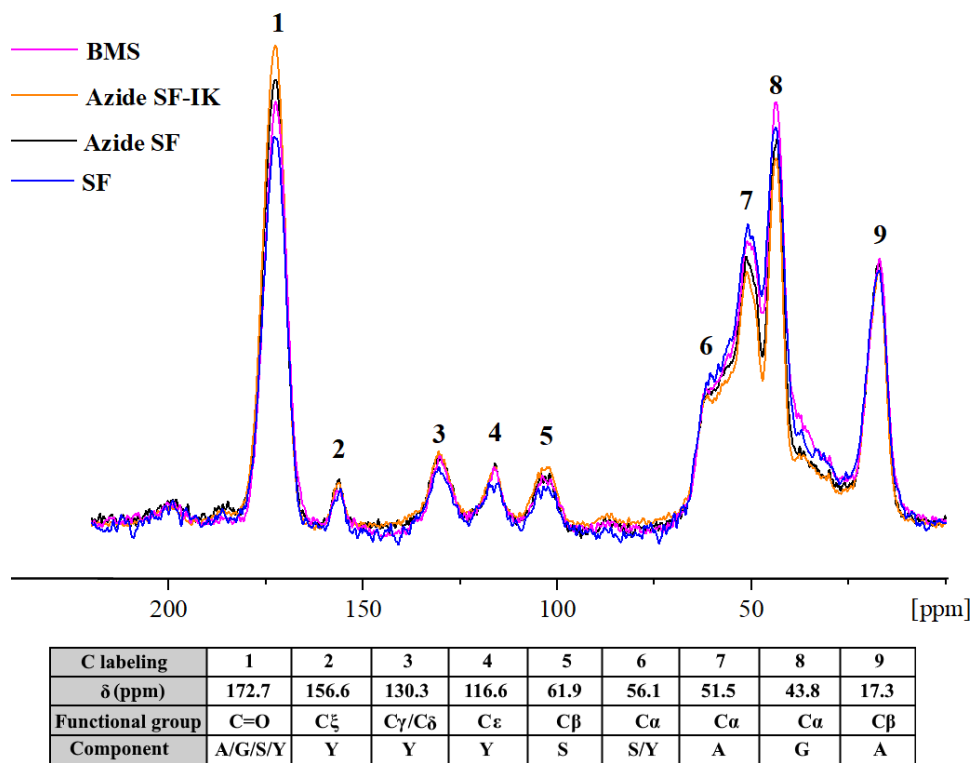
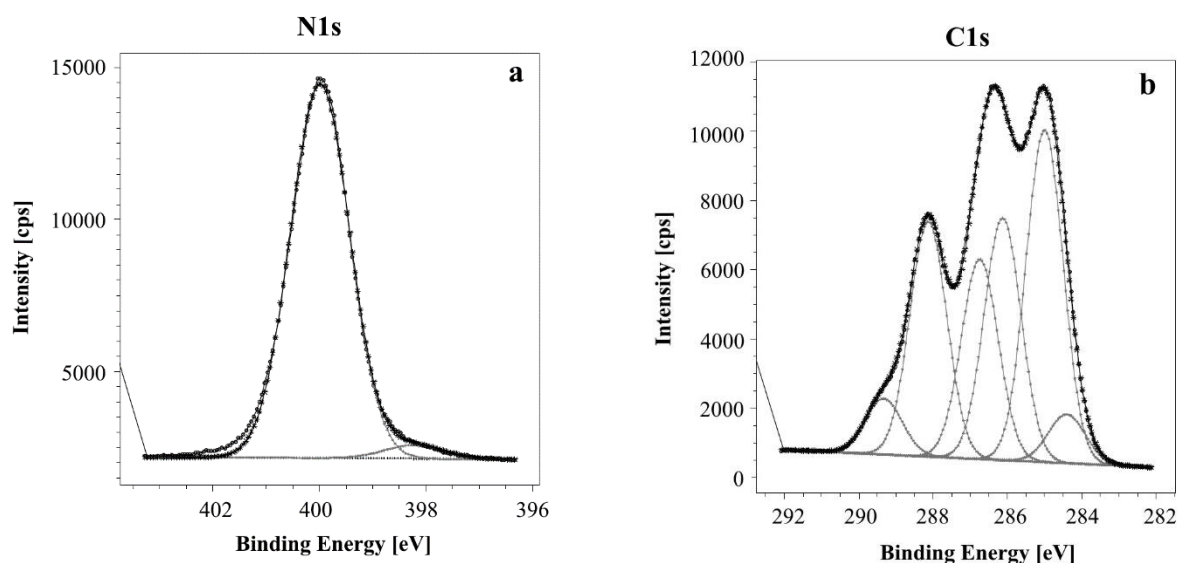


Figure 18. ^{13}C CPMAS NMR spectra of silk fibroin and modified fibroin. (A: alanine, G: glycine, S: serine, Y: tyrosine).

The percentage of Silk II was also evaluated, following the description presented in Callone et al ¹³⁶; it decreases in Azide SF (36.6%) compared to the SF (38.1%), increases with the Azide SF-IK (43.6%) and decreases again after the addition of the Col(IV) (40.9%), which might due to the steric hindrances. XPS analysis was performed on SF and BMS in order to highlight the efficiency of the click reaction.

The N1s core line of the SF shows two peaks at 400 eV and 398.3 eV assigned respectively to O=C-N- and N in the amino acids displaying aromatic rings ^{137,138} (Figure 19a).

The six different peaks of C1s core line of the SF (Figure 19b) can be ascribed to -C=C (284.4 eV), to CH_x (285 eV), to C-N bond (285.9 eV), to -C=O (287.5 eV), to O=C-N- (288 eV) and to -O-C=O (289.5 eV) ¹³⁹⁻¹⁴². Spectral analysis revealed in SF an amount of carboxylic groups equal to 3.2% mol in accordance with the previously cited literature ¹²⁵.



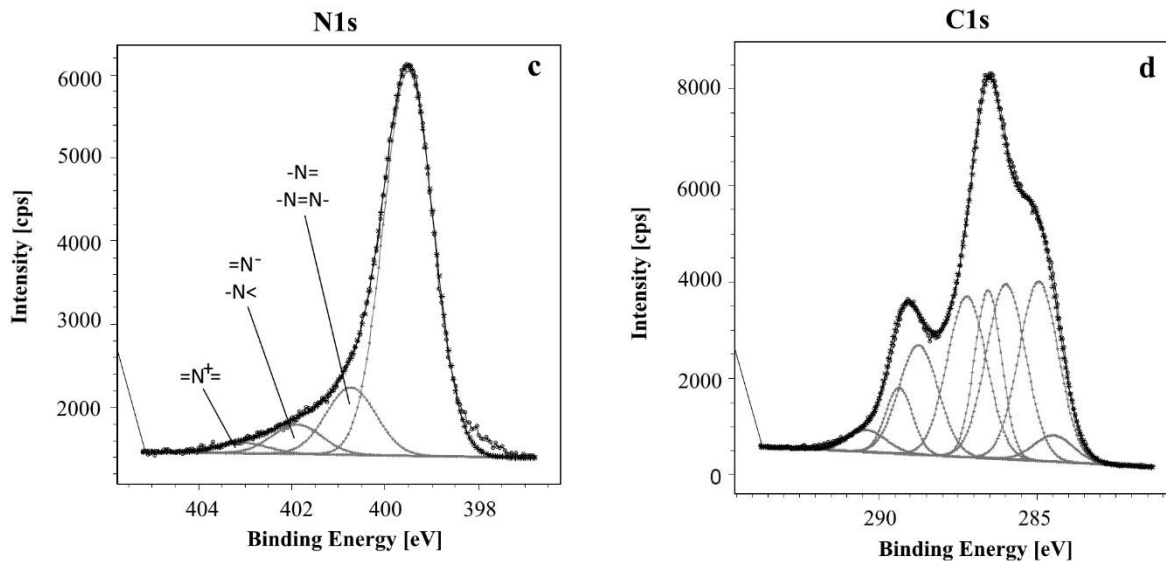


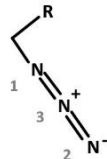
Figure 19. XPS core lines for Silk fibroin (a and b) and BMS (c and d).

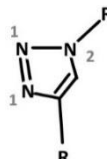
The three components from the N1s core line of BMS are evidenced in Figure 4c and transcribed in Table 1a. The acquired values are compared with the values of Table 1b and 1c where the components of unreacted azide ($-N_3$) and triazole, i.e. the bridge between DBCO-Col(IV) and Azide SF-IK, are respectively reported ^{143, 141}. The presence of the component at 403 eV indicates that in the final BMS compound 37% of azide, i.e. the ratio between the 403eV component in the free (Table 2b) and reacted azide (Table 2a), did not react. The C1s core line (Figure 19 d) of the BMS sample shows, instead, an increase of $-C=O$ and $C-N$ components for the presence of the Col(IV) hydrophilic amino acids.

Table 2. . a) Components of the SF-Col(IV). The $-N=$, $=N-$ and $=N+=$ bonds are referred to azide groups. The $-N=N-$ and $-N<$ bonds are referred to triazole compounds.. a) Components of the SF-Col(IV). The -

$N=$, $=N-$ and $=N+=$ bonds are referred to azide groups. The $-N=N-$ and $-N<$ bonds are referred to triazole compounds. b) Components of azide groups. c) Components of triazole compound.

a	components	$E(eV)$	$FWHM(eV)$	%
	1) $-N=$, $-N=N-$	400.7	0.48	62
	2) $=N^-$, $-N<$	401.8	0.48	28
	3) $=N^+=$	403	0.48	10
	1/2/3 Ratio %		6.2/2.8/1	

b	components	$E(eV)$	$FWHM(eV)$	%	
	1	400.9	1.9	41	
	2	402	1.9	32	
	3	403	2.1	27	
	1/2/3 Ratio %		1.5/1.18/1		

c	components	$E(eV)$	$FWHM(eV)$	%	
	1	400.7	1.9	66	
	2	401.7	2.3	34	
	1/2 Ratio %		1.95/1		

The secondary structure of lyophilized SF, Azide SF, Azide SF-IK and BMS solutions were characterized by ATR-FTIR. This analysis highlights mainly the functionalization of the SF tyrosines by diazonium coupling that change the stability and the conformation of the SF as confirmed by the percentage of Silk II evaluated by CPMAS NMR. The vibrational absorptions spectra are shown in [Figure 20 a](#). The significant bands ^{113,126,144–146} at 1650 cm⁻¹ (Amide I), at 1540 cm⁻¹ (Amide II), at 1236 cm⁻¹ (Amide III) are visible in all spectra. However, the shoulder at 1518 cm⁻¹, corresponding to the β -sheet conformation, decreases in Azide SF, Azide SF-IK and BMS with respect to SF, thus suggesting a reduction of β -sheet content might due to the SF and azide interaction. This seems to be confirmed by the absorbance band at 1412 cm⁻¹ that represents the C-OH bending vibration ^{147, 148}. In fact, the increasing of the C-OH bending vibration after fibroin treatment with azide groups demonstrates a reduction of tyrosine functional groups involved in intra- and intermolecular hydrogen bonds between the hydrophobic side chains.

In the curves related to lyophilized SF, Azide SF, Azide SF-IK and BMS hydrogels no differences can be observed. Instead, as expected, the comparison with the curves of the corresponding solutions clearly shows a shift of the main peaks to lower wavelengths ([Figure 20b](#)), due to the transition to β -sheet structure after sonication. In particular, the shift from 1650 cm⁻¹ to 1622 cm⁻¹, from 1540 cm⁻¹ to 1517 cm⁻¹ and from 1236 cm⁻¹ to 1229 cm⁻¹ related to the β -sheet transitions. The decrease of the band at 1415 cm⁻¹, corresponding to the C-OH bending vibration^{113,145,149,150} is probably also a consequence of the β -sheet transition due to the sonication treatment.

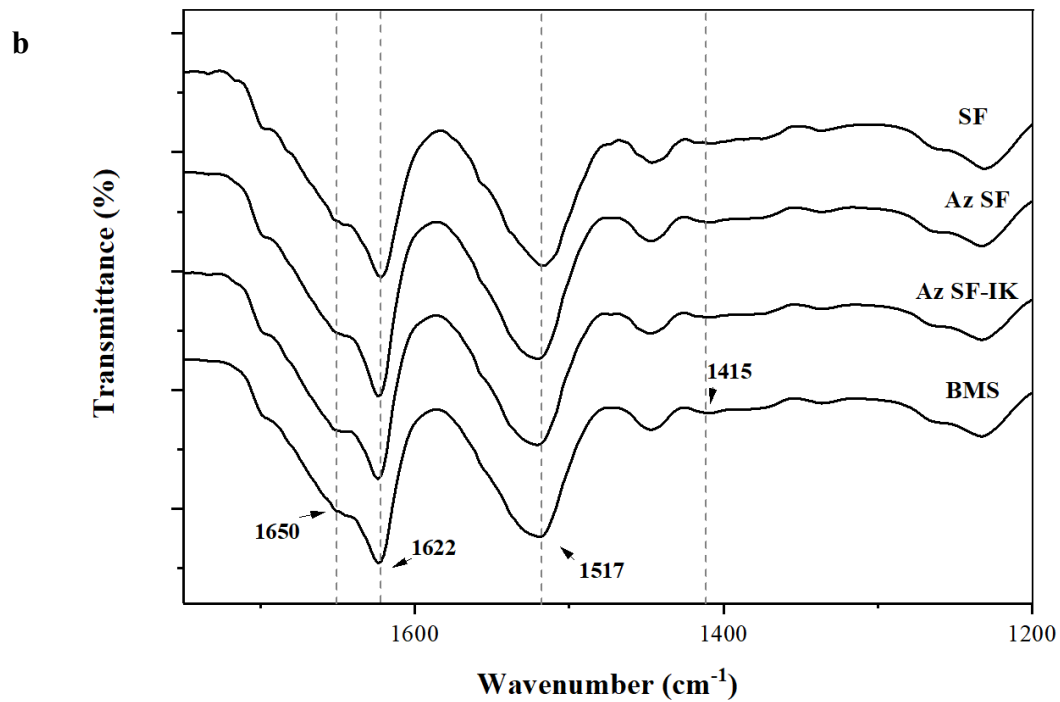
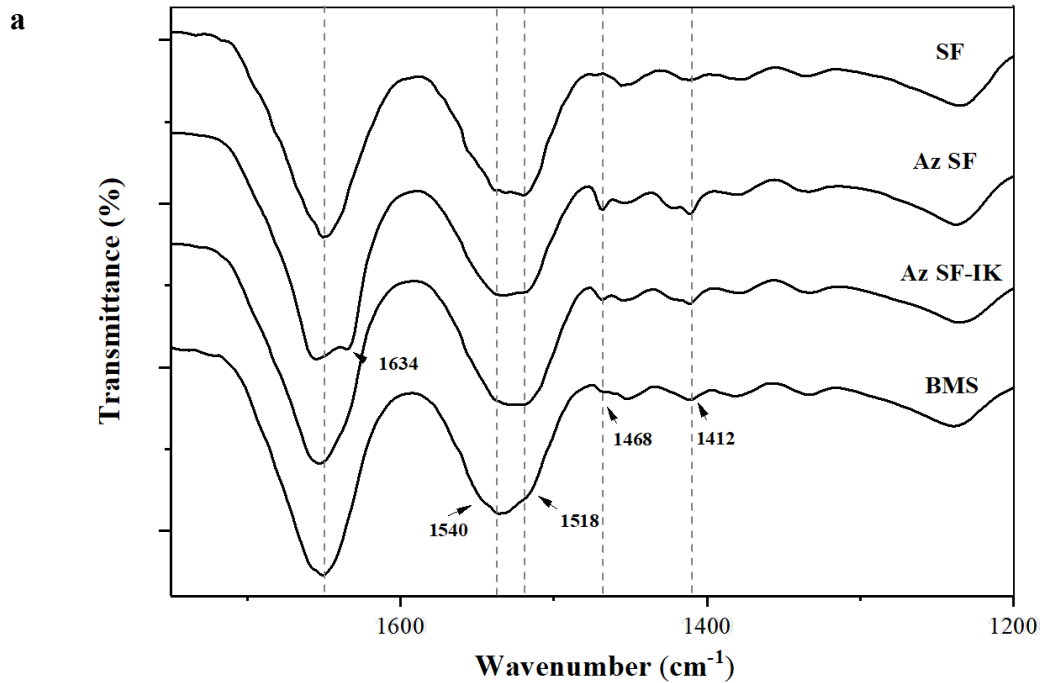


Figure 20. ATR-FTIR spectra of lyophilized SF-based solution (a) and hydrogels (b)

The modulated DSC curves of lyophilized silk fibroin based hydrogels (SF, Azide SF, Azide SF-IK, BMS), of 4-azidoaniline hydrochloride reagent (4-Az) and Col(IV) were acquired to observe the structural changes of SF after each reaction and confirm the data of CPMAS NMR and ATR-FTIR analysis. The Table 3 reports the characteristic thermal values showed in Figure 21.

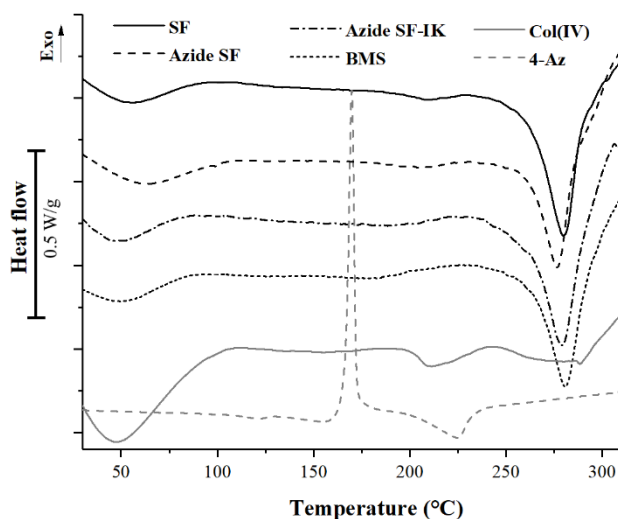


Figure 21. Modulated DSC curves of 4-azidoaniline hydrochloride (4-Az), Col(IV) and lyophilized silk fibroin-based hydrogels.

Table 3. Characteristic DSC values of modified and unmodified silk fibroin hydrogels.

	Texo	Tg	Td
	°C	°C	°C
SF	230	205	279
Azide SF	230	205	277
Azide SF-IK	225	195	279
BMS	226	175	280
Col(IV)	-	-	210

4 Azidoaniline 165 - 225
hydrochloride

T_{exo} = temperature of exothermic peak; T_g = glass transition, T_d = temperature of degradation .

For 4-azidoaniline hydrochloride heat flow curve displays a sharp exothermic peak at around 165 °C followed by a large endothermic peak centered at about 225 °C. This exothermic peak is the sum of the endothermic melting at 165 °C and of a larger exothermic phenomenon well marked in the non-reversible heat flow curve (Figure not reported), probably due to the decomposition of the azide. A further and final degradation occurs at around 225 °C.

In all curves of the SF containing samples and of Col(IV) the wide endothermic irreversible peaks centered at about 50-60 °C are due to the evaporation of water from the freeze-dried materials.

Thermal behavior of SF has been described in many papers, starting from the early work of Magoshi et al.¹⁵¹. More recently, the effect of annealing treatment on SF transition has been investigated by thermal and dynamic mechanical analysis¹⁵². Depending on structure, T_g s ranging from about 170 °C to about 200 °C have been reported. Accordingly, our analyses place the SF glass transition at around 200 °C, that is followed by the exothermic crystallization centered at about 225 °C and a final endothermic degradation at 279°C. Similar values have been detected for the azide conjugated SF.

The introduction of IK in the SF chain causes a slight decrease of the polymer glass transition temperature and correspondingly an earlier crystallization.

More noticeable changes take place in the final BMS, whose T_g values lowers to about 175 °C, with an earlier beginning of the crystallization phenomenon. Worth nothing is the fact that endothermic peak of denaturation that for Col(IV) occurred at about 215 °C is not visible in the final BMS polymer.

Rheological tests made on SF and BMS hydrogels (Figure 22) confirmed the gel-like structure of the materials ($G' > G''$) and reveal a noticeable increase of the elastic modulus of BMS with respect to SF (about 5 KPa vs. 3 KPa), both near the stiffness of the glomerular BM¹⁵³.

The stiffness of hydrogels is an important factor to consider in regulating stem-cell fate. Mimicking the stiffness of a specific tissue, the differentiation fate of stem cells can be regulated and directed toward those tissue-specific cells¹¹².

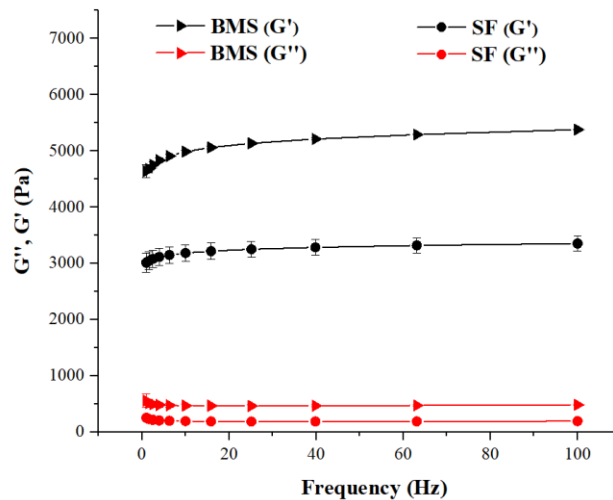


Figure 22. Rheological evaluation of the storage and loss modulus in the range of 1-100 Hz of unmodified and modified silk fibroin.

Thermogravimetric analysis (TGA) indicates that the amount of water in those hydrogels ranges around 95-96 wt%, with a much slower water loss kinetics for SF as a consequence of its tighter crystalline structure and the larger presence of hydrogen bonds.

As preliminary evaluation of cell behavior in response to fibroin functionalization, adhesion, cell morphology and metabolic activity were assessed on MRC5 cultures up to 7 days on films and hydrogels of SF and BMS (Figure 23). The fibroblast cell line is often used for biocompatibility testing and changes in early adhesion can prove the presence of a bioactive surface¹⁵⁴. The results summarized in Figure 8a-b, clearly show the formation of adhered cell spindle-shape typical of fibroblasts activation when cells are cultured on BMS films (BMS-f) already at day 1, whereas a round-shape is mainly observed for SF-film (SF-film) at the first experimental time point as well as for SF and BMS hydrogels (SF-h and BMS-h). At day 3 and 7, the substrates fabricated of BMS seem to sensible increase cell spreading and cell-cell connection notably in BMS-f. Instead, the number of cells determined by 4',6-diamidino-2-phenylindole (DAPI) fluorescence staining (Supporting information) revealed a slight increase of cell growth solely on films and a constant number of cells in hydrogels. AlamarBlue data (Figure 24), show a similar trend on all samples, with an increase in cells metabolic activity from day 1 to day 7. However, despite the low proliferation rate, significantly higher values on sample BMC-f were detected in particular at 3 and 7 days. Results are in well agreement with confocal imaging results, confirming the positive impact of the functionalization on cell adhesion, spreading and, most interestingly, metabolic activity. The highest metabolic activity values observed in BMS-f cell cultures, is mainly due to the higher density of functional groups exposed to cells, if compared with hydrogels. In addition, it should be underlined that the biological impact of the modified SF hydrogels on adhesion of MRC5 can be also due to other factors, such as surface energy, water content and also surface mechanical stiffness.

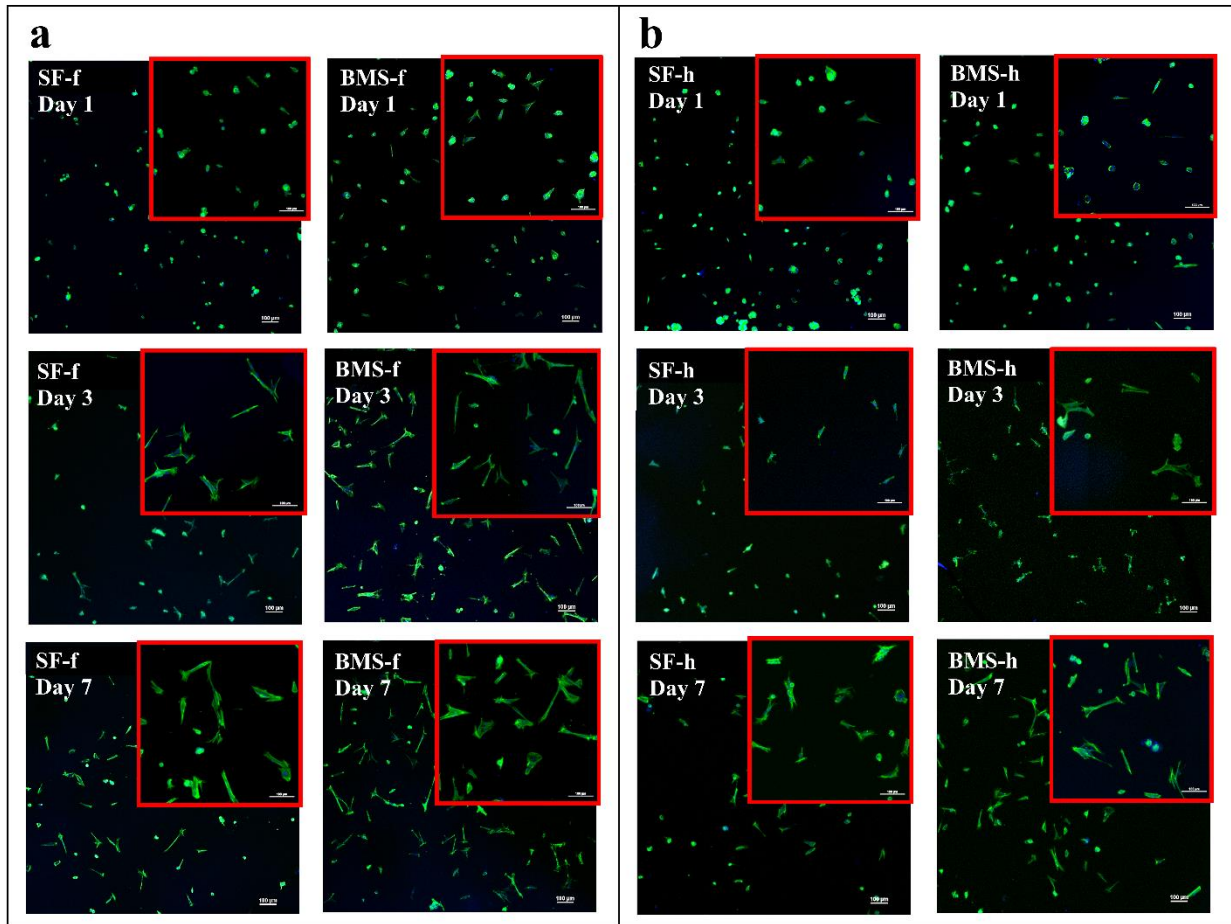


Figure 23. Early adhesion of MRC5 on modified and unmodified films (a) and hydrogels (b) at different time points (1-3-7 days) (h: hydrogel; f: film).

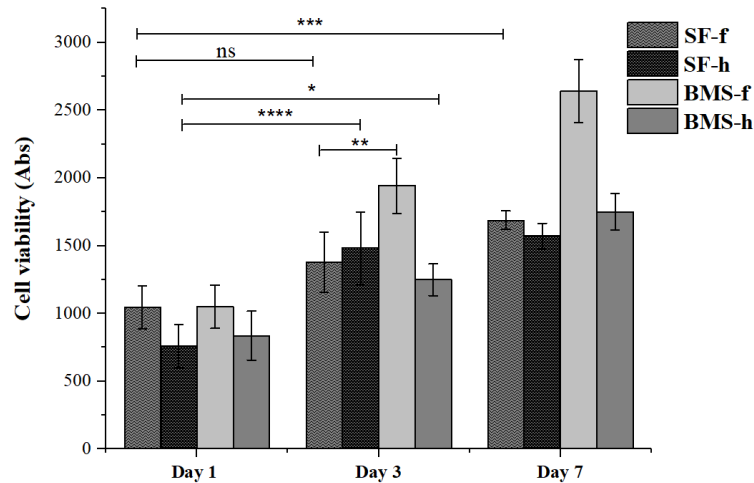


Figure 24. AlamarBlue assay for the evaluation of the cell viability of MRC5 cultured on modified (BMS) and unmodified fibroin (SF) films (f) and hydrogels (h) at day 1-3-7. (* $p < .05$, ** $p < .01$, *** $p < .001$, **** $p < .0001$, ns=not significant). AlamarBlue assay for the evaluation of the cell viability of MRC5 cultured on modified (BMS) and unmodified fibroin (SF) films (f) and hydrogels (h) at day 1-3-7. (* $p < .05$, ** $p < .01$, *** $p < .001$, **** $p < .0001$, ns=not significant).

2.1.4 Conclusions

In this study, a bioinspired multi-functionalized silk fibroin was successfully synthesized and characterized in detail. TNBS test and XPS analysis quantitatively estimated the efficiency of Col(IV) modification with DBCO groups (about 52%) and SPAAC reaction (about 63%). Data about change in fibroin conformation revealed that the presence of IK peptide and Col(IV) in the structure created a less compact crystalline structure, as confirmed by spectroscopic analysis. In contrast the physical crosslinking of the BMS solution by sonication increased the storage modulus of BMS hydrogel of about 2 KPa with respect to the SF hydrogel, in the range of the mechanical properties of the glomerular BM.

Preliminary biological evaluations were performed by culturing MRC5 cells as a cellular model to verify the influence of the fibroin functionalization on early cell bioactivity. Significant increase of cell adhesion, spreading, viability and cell-cell interaction was observed in BMS films compared to the unmodified SF. To further enhance cellular activity within the scaffolds, even mechanical properties and water content will be tuned depending on the intended application^{155,156}.

The following chapter reports the gelation of BMS under an applied electrical field in order to impart its piezoelectric properties that, as previously described, could enhance the repair process of the spinal cord.

2.2 Electric field effect on piezoelectric properties of BMS

In collaboration with Ilaria Corridori* and Isacco Mazo**

**Laboratory of Bio-inspired, Bionic, Nano, Meta Materials & Mechanics, Department of Civil, Environmental and Mechanical Engineering, University of Trento, Italy*

***Department of Industrial Engineering, University of Trento, Italy*

2.2.1 Introduction

An electrical stimulation was demonstrated to help the axon elongation, cell survival and neurons differentiation. An electric field generated intrinsically into a SCI reparative material may avoid external power supply to stimulate the cells and infections.

Biopolymers with crystalline domain, which have a non-centrosymmetric nature, are able to convert mechanical energy into electrical energy or vice versa and show intrinsic shear piezoelectricity, an electrical polarization perpendicularly to the shear deformation. In particular, collagen shows piezoelectric properties. The collagen piezoelectricity allows osteocytes to detect areas with high stress. The application of stresses generates a local potential gradients along the collagen fiber that stimulate the bone generating cells¹⁵⁷.

Instead, also silk fibers are piezoelectric as well. Piezoelectricity of materials plays an important role in harvesting energy from various mechanical and biomechanical activities¹⁵⁸. Fukada et al. evaluated the intrinsic shear piezoelectricity of silk fiber bundles measuring a value of ~ 1 pC/N, near to the quartz crystal (~ 2 pC/N)¹⁵⁹.

As mentioned before, the silk fibroin (SF) is a fibrillar protein composed by a heavy (H) chain, (~ 350 kDa) and a light (L) chain (~ 26 kDa) linked together by a disulphide bond. The heavy chain has highly

ordered hydrophobic areas and repetitive sequences, which can cooperate to form anti parallel β -sheet crystallites. Instead, the light chain is mainly composed by polar hydrophilic amino acids (glutamic and aspartic acid residues) that make the structure more flexible and give the heavy chain a polyelectrolyte nature¹⁵⁹.

In BMS, the polyelectrolyte nature is implemented by the conjugation of the regenerated SF with laminin peptide IKVAV and Col-IV.

The SF as well as the BMS solution are prevalently structured in alfa helix and random coils domains, metastable structures that can change depending on the microenvironment and processing conditions. The metastable structure can be converted into an anti-parallel β -sheet structure interconnected by hydrogen bonds. The β -sheet conformation creates insoluble fibroin films, for example after casting the solution and a treatment with 80% methanol. Silk solutions can be physically crosslinked with the formation of an hydrogel with various methods various, among those ultrasounds.

The presence of hydrated water in the hydrogel makes easier the internal rotation of the dipoles and shortens relaxation time required for the rotation¹⁶⁰. Moreover, a high degree of β -sheet crystallinity and high orientation improve the piezoelectricity of silk. Many techniques have been studied to improve the β -sheet crystallinity of silk. The exposure of silk to hot water vapor¹⁶¹ as well as icing methods¹⁶² were proven efficient in augmenting the degree of β -sheet crystallinity. Yucel et al¹⁵⁹. designed a processing toolkit to maximize silk II crystallinity and crystal alignment with a two-step method: i) air drying of regenerated silk fibroin solutions into films, and then ii) drawing the silk films to a desired draw ratio. Recently, electric fields generating by 24 Volt or 220 Volt in alternating current (AC) were applied during casting fibroin films to manipulate the alignment of molecular dipoles and increase the presence of intermolecular β -sheet¹⁶³. In several paper, the presence of an electric field, generated after stimulation of piezoelectric film with aligned domains based on PVDF (poly(vinylidene fluoride) or polypyrrole, has

been demonstrated to help the neurite growth¹⁶⁴. Moreover, electrical stimulation was proven helpful to increase wound healing, by improving cell migration, the growth of fibroblasts and myofibroblasts, and promoting the production of growth factors¹⁶⁵.

However, in very few cases^{166, 167}, the piezoelectricity of hydrogels was studied and evaluated, mainly, for spinal cord regeneration.

Mousavi et al. used a finite element model to simulate a nonlinear three-dimensional charged matrix with encapsulated piezoelectric spheres. A magnetic force was applied in the longitudinal direction to stimulate the piezoelectric matrix and generate an electric field of maximum ~ 94.9 mV/mm able to induce cell proliferation and differentiation of neural precursor cells¹⁶⁶.

Alternatively, Dadsetan et al proposed a hydrogel of oligo-(polyethylene glycol) fumarate (OPF) with a positively charged monomer that supported the attachment and neurite outgrowth from DRG explants containing Schwann cells¹⁶⁷.

The absence of an action potential that connect the neurons and help their survival in a scaffold seems to be an important factor to improve the regeneration of an injured spinal cord. The presence of an intrinsic current or a voltage produced during small deformations of the hydrogel could be the best solution to avoid external power supply and connected infections.

The shear piezoelectricity coefficient of the silk fibroin films was measured by Yucel et al to be around -1.5 pC/N and they demonstrated also an improvement of the piezoelectric properties increasing the β -sheet crystalline structures of the SF.

The aim of this work has been the study of the effect of the electric field effect generated after a 220 V and 24 V in direct and alternating current on the piezoelectric properties and conformational changes of BMS and SF hydrogels. Small deformations of BMS hydrogels might be used to generate an intrinsic

voltage useful for the cell survival, cell-cell interaction and neural stem cells differentiation into neurons. Indeed, the excitatory postsynaptic potential is around 12 mV, as well as the voltage measured after hyperpolarization (AHP) is around 5.4 mV in native conditions¹⁶⁸. The presence of Col(IV) and laminin conjugated to the silk fibroin could increase the potential of the SF-based hydrogel, mainly, due to the collagen piezoelectricity expressed after shear deformation. The mechanical deformation of the BMS hydrogel to bypass the SCI, could be obtainable by the movement of the neck or the back or eventually by shock wave, so possibly the potential might be generated directly inside the spine without any external supplier.

The electric field effect on SF and BMS hydrogels was modeled by finite element method using COMSOL Multiphysics in order to compare the experimental data with the theoretical ones. The piezoelectricity was evaluated compressing i) a cylinder of SF/BMS hydrogel perpendicularly to the electric field lines (Geometry A) by the set up described in the experimental section or ii) parallel to the electric field lines (Geometry B). Moreover, the secondary change conformation was investigated by ATR-FTIR analysis in order to verify the increase of the beta-sheet structure and correlate these results with the piezoelectric measurements. The biological effect of stimulated SF hydrogels was evaluated on human neuroblastoma cell line (SH-5YSY) as a preliminary investigation to optimize the experimental set up for the future analysis with human neural stem cells (hNSCs) on BMS hydrogels. The SH-5YSY was selected to evaluate their survival on the hydrogel and observe a neuron-like behavior in order to obtain preliminary data.

2.2.2 Materials and Methods

Simulation. The distribution and the magnitude of the electric field across the stimulated fibroin hydrogel were modelled by finite element method using COMSOL Multiphysics. The 3-D model made of borosilicate glass (bottom ceiling), polystyrene (cell walls), fibroin hydrogel, and air (domain) were designed by a CAD software and imported into COMSOL. Electrostatic physics was selected in the solid module of the wizard in order to simulate the 3-D component of the electric displacement field (D), as electric polarization (P) and electric field (E). Materials were selected from the software library, of which the relative permittivity used in the electrostatic equations was reported in Tab. 4. Fibroin hydrogel is not available in the library and was manually added by inserting the proper electrical parameters. The fibroin hydrogel was electrically stimulated during its cross-linking which caused a shrinkage in the z-direction. This variation affects the spatial distribution of the electric field (D), hence the entire model was solved twice. Once for a hydrogel thickness of 6 mm (Geometry B), and once for 3.5 mm (Geometry A), thicknesses reached after the electrical stimulation. The voltage difference of 24 and 220 V is applied between the two electrodes on the polystyrene cell walls, corresponding to the terminal and the ground. The mesh used for the simulation was refined with a parametric sweep study, passing from a physics-controlled mesh to a user-controlled one. A custom maximum element size of 10 mm was refined by controlling a mesh refining factor (MRF) that allow the convergence fixing the maximum element size at 10/30 and a minimum element size of 0.8.

The average electric field inside the gel was used as a controlling output parameter for the sweep study, the suitable element size corresponded to the MRF leading to the convergence.

The electrostatic module of COMSOL will solve Gauss's law for the entire domain except for the two metallic strips, according to:

$$\nabla * \mathbf{D} = \nabla * (\epsilon_0 \mathbf{E} + \mathbf{P}) = \nabla * \epsilon_0 \epsilon_r \mathbf{E} = \rho_f$$

$$\mathbf{E} = -\nabla V$$

Where ρ_f is the number of free charges per unit volume and V the potential difference as applied between the terminal and the ground.

Table 4. Values of the selected dielectric materials.

	Air	Hydrogel	Polystyrene	Borosilicate glass
Relative permittivity [ϵ_r]	1	70	2.6	4.8

SF solution preparation. SF solution was prepared according to the reported method of section 2.1.2.

BMS solution preparation. The synthesis of the BMS is described in detail in Section 2.1.2. Briefly, the SF is modified by azide groups through diazonium coupling reaction and the Col(IV) is conjugated at pH 7,4 with DBCO-NHS compound at 4°C for 2 hours. The two precursors: Azide-SF and Col(IV)-DBCO was left to react spontaneously at RT. The laminin A chain motif IKVAV was conjugated to the carboxylic groups of the Azide-SF by using the EDC/NHS method. The final product is called BMS.

SF and BMS hydrogels preparation. A 3% SF or BMS solution was sonicated for 1 min at 50% of amplitude and poured in a 4 chambers Lab-Tek® Coverglass System with a rectangular glass on the bottom that facilitate the extraction of the hydrogels after gelation. The solution underwent electrical stimulation after the sonication treatment. An electrical stimulation of 50 Hz alternating current (AC) or direct current and 24 V or 220 V was supplied by two stainless steel bars stuck on the longer side of the rectangular 4-chamber systems. The system in toto was incubated at 37° C and the electric fields were imposed until gelation. The extracted hydrogels were cut by a biopsy punch of 6 mm in the perpendicular direction of the theoretical electric field lines direction (1st group: geometry A) and with a 4 mm one to cut cylinders parallel to the electric field lines direction (2nd group: geometry B). The results were considered comparable between the sample of the same group.

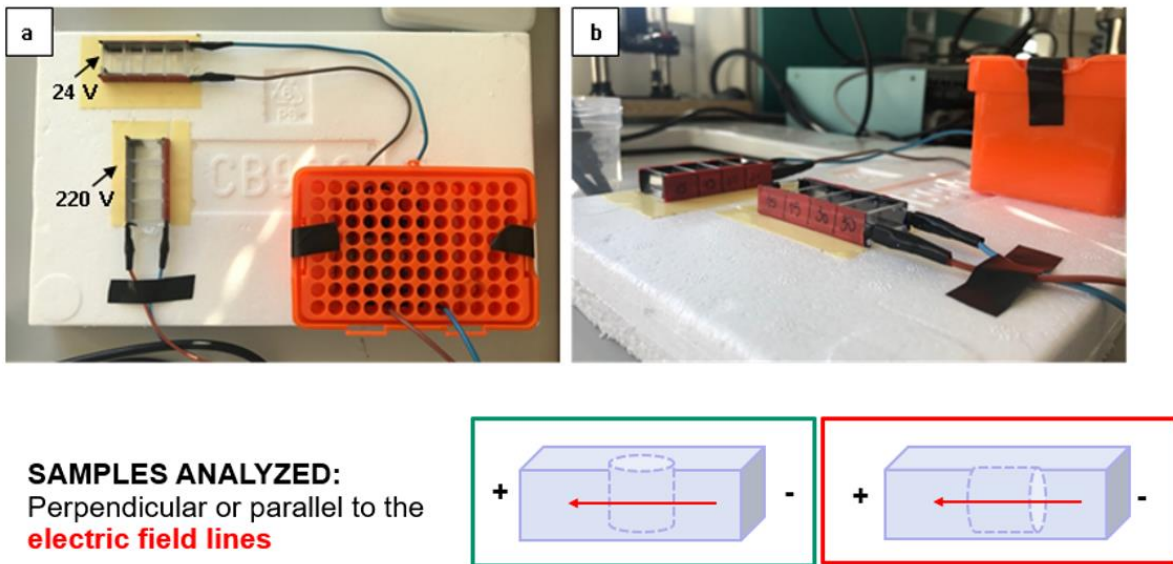


Figure 25. Set up for the SF solution stimulation at 220 V or 24 V. Geometry A (green box) and geometry B (red box).

Piezoelectric testing. The experimental set up is shown in [figure 26](#). Briefly, a compression machine (Bose Electroforce 3200) was modified applying two insulator supports of PMMA to the anchorings of the instrument. Two copper electrodes were fixed to each support. Each electrode is connected to a filter/amplifier circuit, thus the gain of the signal acquired results about 100 times higher than the original one considering a hydrogel resistivity of 100-1000 K Ω . The circuit is connected to the acquisition system, a Keithley DMM 6500 6 1/2 digit Multimeter. The sample was located between the two electrodes and the compression was performed at 0.1 Hz of 100 ms and 15 % displacement for five times in triplicates.

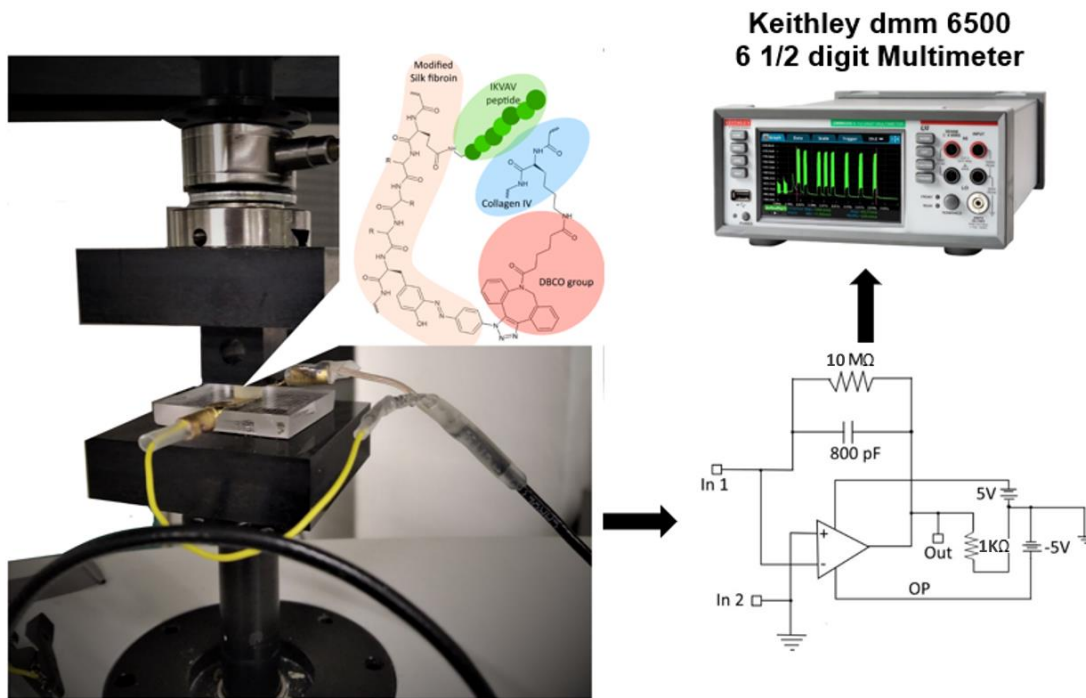


Figure 26. Dynamic Mechanical Analyzer combined with a multimeter for the piezoelectric measurements.

Fourier Transform Infrared Attenuated Total Reflection (FTIR-ATR) Spectroscopy Analysis

The modified and unmodified BMS hydrogels after electrical stimulation were freeze-dried and the secondary structures were analyzed by infrared spectroscopy using an instrument working in attenuated total internal reflection mode equipped with a zinc selenide crystal (ATR-FTIR, BRUKER TENSOR 27). Each spectrum was the mean of 64 acquisitions (in the region 4000 and 650 cm^{-1}) with a 4 cm^{-1} spectral resolution. Spectral analysis was performed using OriginPro 2017.

Thermogravimetric analysis (TGA). The TGA analysis was conducted in a Mettler TG50 thermobalance, testing about 100 mg of wet SF/BMS, SF/BMS 24 V and SF/BMS 220 V hydrogels with nitrogen flowing at 100 $\text{ml} \cdot \text{min}^{-1}$ and at a heating rate of 10 $\text{K} \cdot \text{min}^{-1}$ in the range 30–330 $^{\circ}\text{C}$.

Cell adhesion. The Lab-Tek® Coverglass Systems consist of 4 wells already sterile for cell culture. The stain steel bars were autoclaved and glued externally to the wells. Also, the glass localized at the bottom of each well was autoclaved. The sonicated 3% solution of SF was poured in each well up to reach the bar level and covered with the lid. All the system was put inside an incubator at 37 $^{\circ}\text{C}$ until SF gelation. The electrical stimulation system was removed and the cell density seeded of human neuroblastoma cells (SH-5YSY) was 0.2 $\cdot 10^6$ cell/mL cells per scaffold. The SH-5YSY cell line was chosen due to the possible application of stimulated SF hydrogel in SCI regeneration and their similarity with neural stem cells. In case of SH-5YSY death, the system will be considered unsuitable for a future use of neural stem cells. The culture medium of SH-5YSY consists of: DMEM 87%, Fetal Calf Serum 10%, Sodium pyruvate 1%, L-glutamine 2 mM 1%, Antibiotic/Antimycotic 1%. The samples were incubated at 37 $^{\circ}\text{C}$, 5% CO_2 for two time points (1-7 days). After each time point, the samples were washed with PBS and the cells were fixed with 4% paraformaldehyde in PBS for 30 minutes. The samples were washed again with PBS and permeabilized with 0.1% Triton-X100 in PBS for 30 minutes. After a further washing in PBS, the cells were then treated for 30 minutes in a dark environment, firstly, with rhodamine-phalloidin

to detect the cytoskeleton, and with DAPI to counterstain the nuclei of the cells. They were imaged using a Nikon TE2000-S fluorescent microscope (Melville, New York). Unmodified SF hydrogel were used as control.

2.2.3 Results and Discussion

The stimulation of the SF and BMS hydrogel with different electric fields influenced the rearrangement of the SF and BMS molecules promoting different electrical behavior.

The simulation highlights a maximum normal polarization vector of $1.7 \times 10^{-6} \text{ C/m}^2$ and an electric field of 2790 V/m for sample treated with 220 V and $1.6 \times 10^{-7} \text{ C/m}^2$ and 303 V/m for sample treated with 24 V. The simulation shows also an homogeneous electric field into the hydrogel (Figure 27) and negligible edge effects near the electrodes.

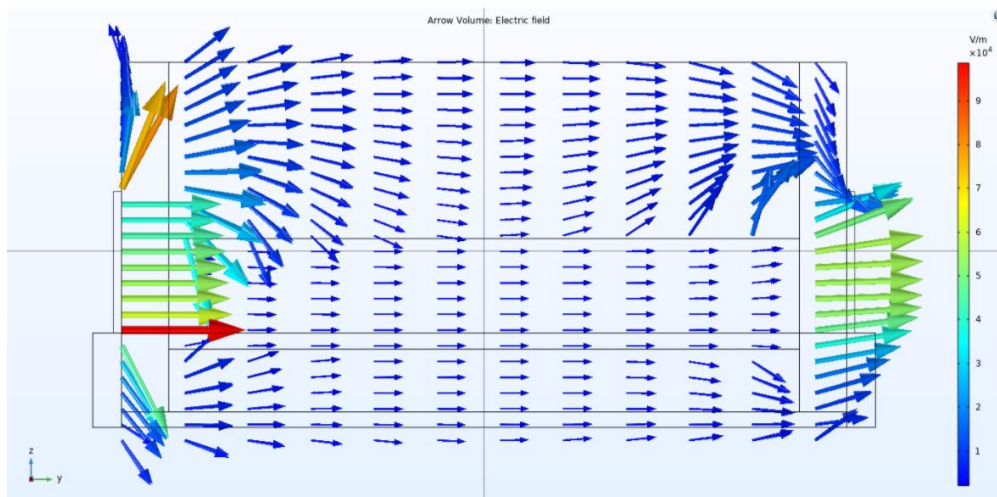


Figure 27. Electric field lines generated with a potential of 220 V.

The piezoelectric data acquired by using the modified set up of figure 28 reveal an increment of the piezoelectricity from 1.2 to 3.7 mV for the SF hydrogels formed at 24 V DC compared to the control

compressed with the geometry A (Figure 29a). The piezoelectricity of the SF control, which was compressed with the geometry B (Figure 29b). showed the highest value of voltage respect to the treated SF hydrogels. The BMS shows a different behavior from the SF: the untreated BMS reveals a value around 1.9 mV and 0.4-0.3 mV for the treated BMS hydrogels compressed with the geometry A, whereas around 8 mV for the treated BMS hydrogels with 220 V DC and around 2.7 mV for the untreated BMS for the geometry B. A possible explanation related to the piezoelectricity acquired is showed in figure 28, where is highlighted the rotation of the dipoles under the compression. From the results, the rotation of the SF dipoles seems to be easily permitted when the compression is performed with the geometry A more than the geometry B, whereas the BMS dipoles seems to be constrained mainly in the direction of the electric field applied.

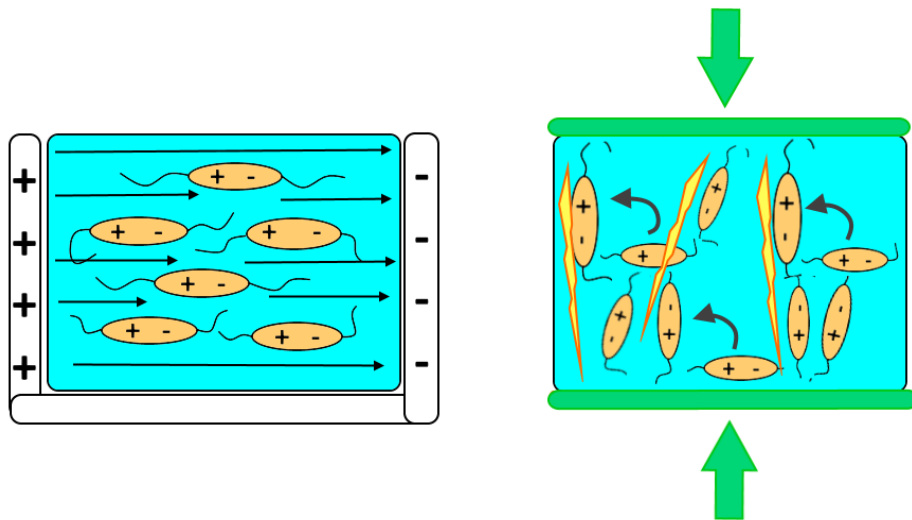


Figure 28. Dipoles orientation during the electric field application and gel formation (left) and dipoles rotation during the deformation. When the dipoles are oriented along the compression direction a potential generates.

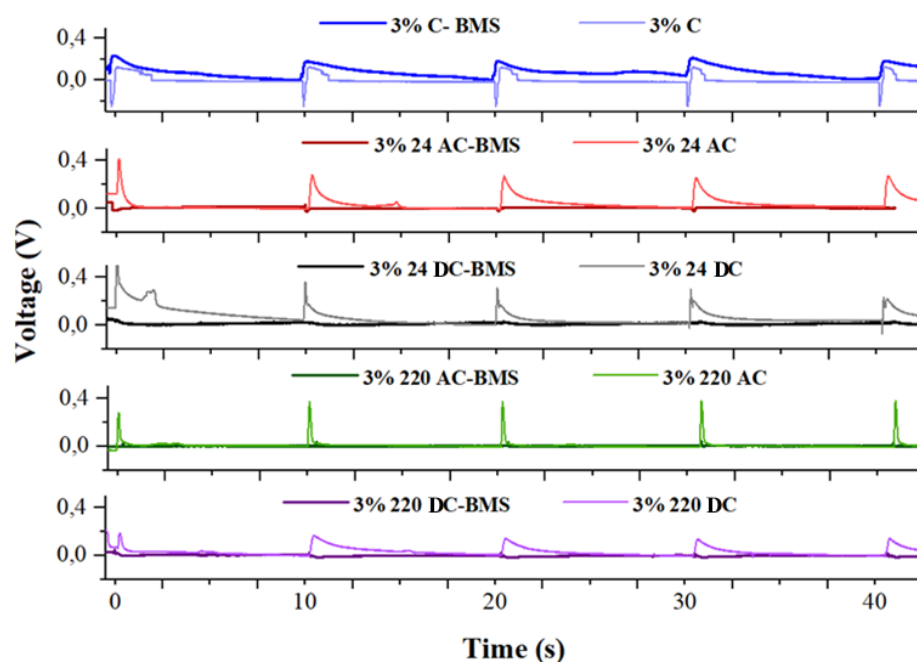
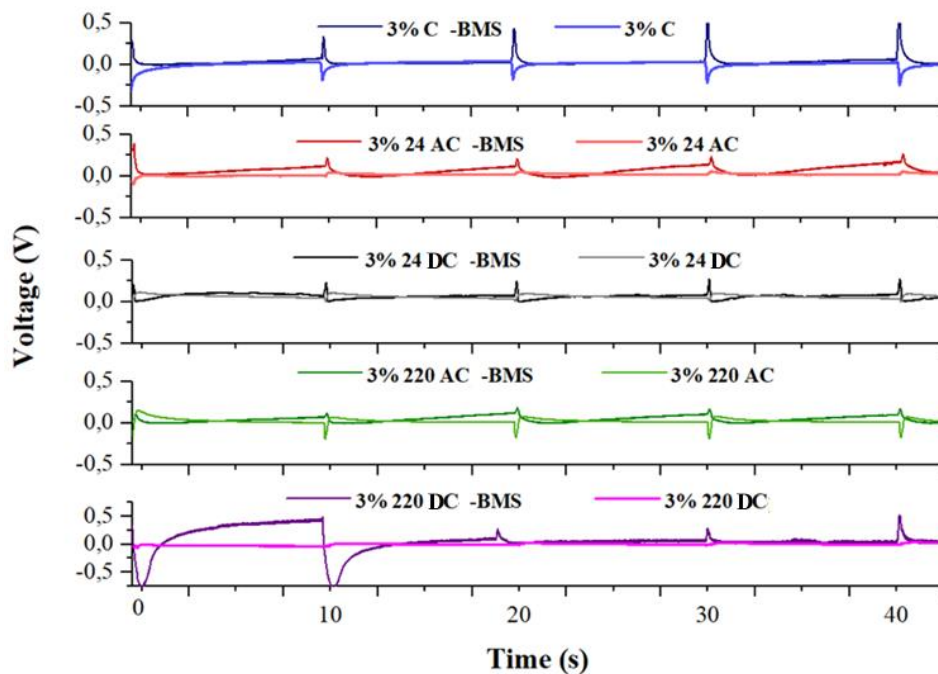
A**B**

Figure 29. Piezoelectricity of the BMS hydrogel. Geometry A (A) and Geometry B (B). (alternating current: AC, direct current: CC)

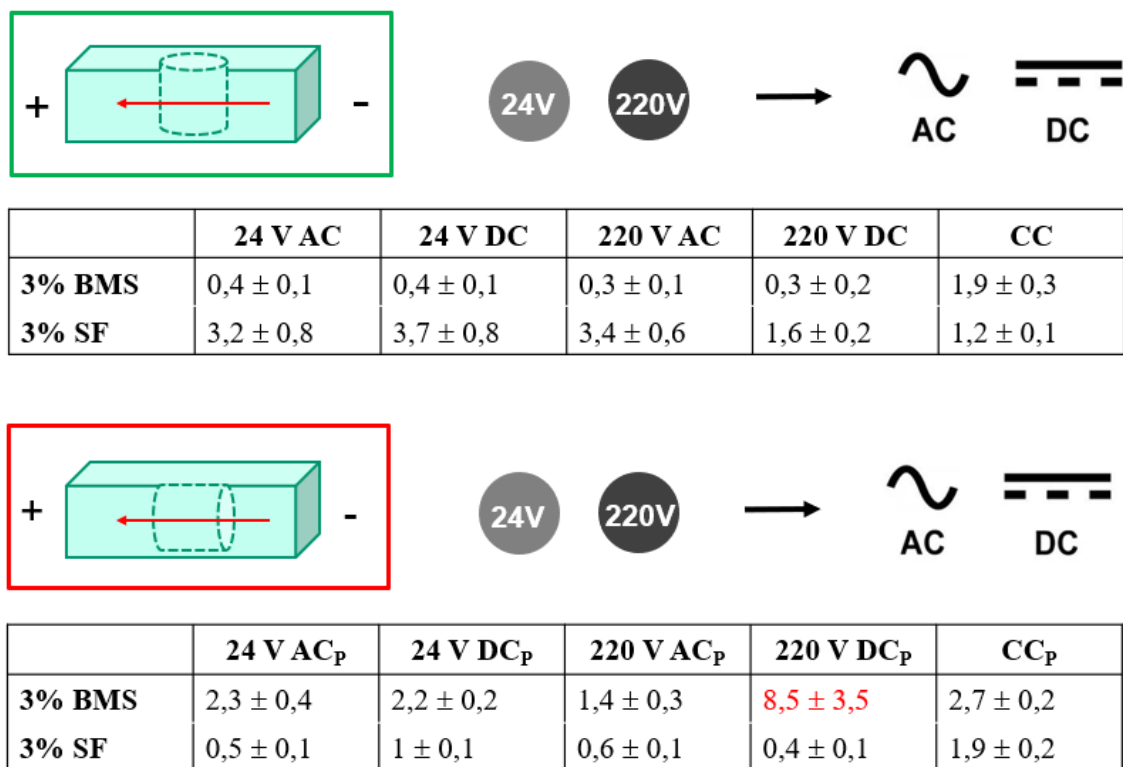


Figure 30. Summary of the BMS results. Geometry A (green box) and geometry B (red box).

A thermogravimetric analysis (TGA) curves (not showed) was also performed in order to verify the water content of the hydrogels, which can influence heavily the piezoelectric measurement. Indeed, the movement of the ions can be promoted if the water content is higher. The results indicate that the amount of water in treated and untreated hydrogels ranges around 95-96 wt%. This means that the water content remains univariable after the application of 24 V or 220 V. Also, the temperature measured by means of a thermocouple inside the SF/BMS solution during the stimulation revealed constant values around 25.5-27 °C.

In detail, the conformational changes were evaluated for BMS hydrogels treated with 220 V or 24 V. The deconvolution of ATR-FTIR peaks highlights that BMS hydrogels treated with 220 V DC showed

an increase of the β -sheet from 36% to 41.3 %, a decrease of α -helix from 24 % to 17% and an increase of β -turns from 11% to 17% for the amide I (1600-1700 cm^{-1}) (Figure 31). The BMS treated with 220 V DC showed, also, the highest piezoelectricity, thus, the initial hypothesis seems to be validated for the BMS hydrogels: higher β -sheets higher piezoelectricity. The other samples treated with alternating current seems to express a lower piezoelectricity differently to the controls might due to the decrease of the β -sheet from 37% to 32%, mainly on the amide II (1500-1600 cm^{-1}). The results are summarized in the Table 5.

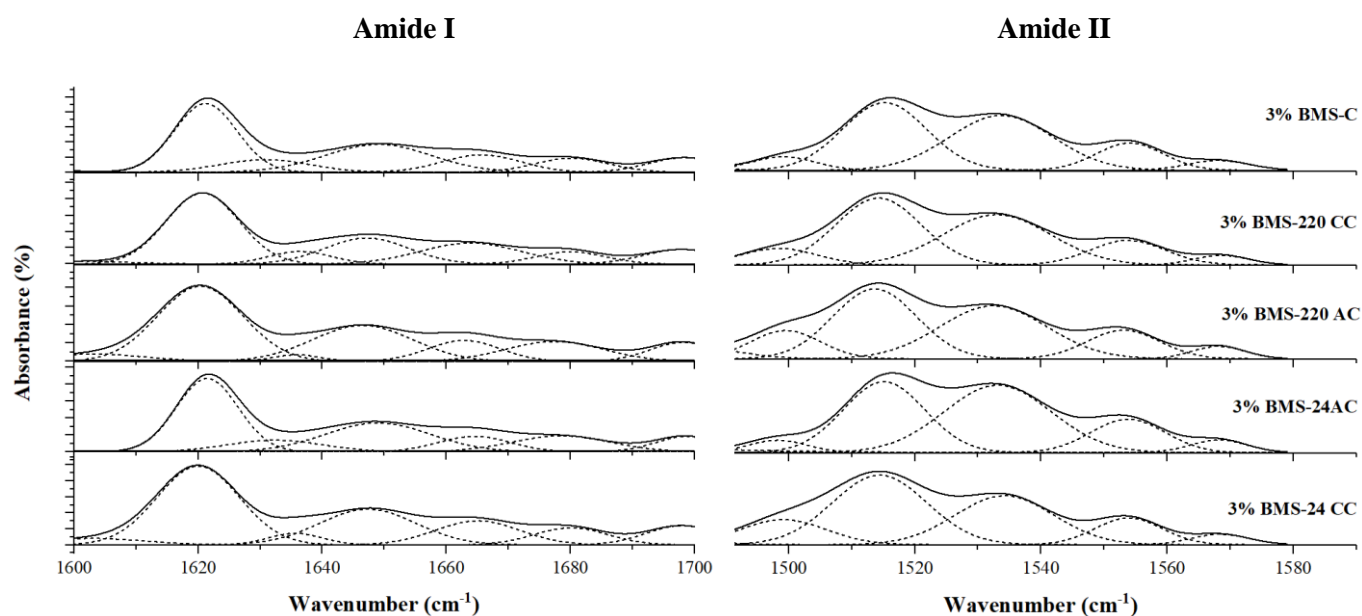


Figure 31. ATR-FTIR deconvoluted peaks of h-BMS treated with 24 V or 220 V in alternating (AC) or direct current (DC).

Table 5. Summary of the ATR-FTIR results for the amide I (A) and amide II (B) of BMS treated (24 AC/DC, 220 AC/DC) and untreated BMS (C).

A	1604 cm ⁻¹ side-chain absorption	1621 cm ⁻¹ β sheet Tyr-OH, ν(CC), δ(CH)	1630 cm ⁻¹ asymmetric stratching of C=O Gly	1648 cm ⁻¹ α helix Arg	1666 cm ⁻¹ β-turns Gln ν(C=O)	1682 cm ⁻¹ β-turns Gln, ν(C=O)	1699 cm ⁻¹ β sheet antiparallel
24 AC	0.6	36.8	8.9	24.8	9.1	12.7	7.7
24 DC	4.3	40.8	3.9	21.7	12.8	7.9	8.6
220 AC	4.8	40.6	1.9	22.7	9.5	12.2	8.1
220 DC	2.3	41.3	6.3	17.4	16.9	6.7	8.9
C	1.1	36,1	9,4	24,7	11,4	8,6	8,7

B	1499 cm ⁻¹ Tyr-O-, ν(CC), δ(CH)	1513 cm ⁻¹ β-sheet Tyr-OH; ν(CC), δ(CH)	1532 cm ⁻¹ ν(NH ₂)	1554 cm ⁻¹ β-sheet (asymmetric) ν C=O of Gly	1570 cm ⁻¹ side-chain absorption ν(C=C)
24 AC	4.1	32.6	40.7	14	3.9
24 DC	13.7	39.6	29.2	10.9	3.6
220 AC	11.3	33.6	32.6	12	3.8
220 DC	8.4	37.7	35.8	12.2	3.4
C	5,6	37,6	37,4	11,9	3,9

Some preliminary biological investigations were performed only on SF hydrogels to avoid waste of expensive materials used for the BMS synthesis or hNSCs expansion. By the way, the set up realized for the biological test was well sterilized and the treated hydrogels results a suitable substrate to seed the cells. The cell adhesion of SH-5YSY can be appreciated in the supporting materials. In general, the

results show a comparable round shape of the cells at day 1 for all the samples but the behavior starts to change mostly for the cells seeded on treated SF hydrogels with 220 Volt. The 220 V AC samples revealed a piezoelectricity of 3.4 mV, which was higher than SF and SF 24 V AC samples. The 220 V AC piezoelectricity might be the cause of the longer extension of the SH-5YSY cytoplasm at day 7. It might be that SF hydrogels treated with 220 V AC induce and help the differentiation of the SH-5YSY. The 24 V sample show apparently a better cell adhesion at day 7 respect to the other samples but this data should be supported by further biological evaluation (Supplementary material).

2.2.4 Conclusions

The BMS hydrogels express piezoelectric properties that might be useful for SC regeneration. Thanks to a local production of voltage, the BMS hydrogel could help to guide the neurons and increase the probability of survival. The presence of laminin peptide and Col-IV seems to increase the intrinsic piezoelectricity of the SF that cannot express a voltage higher than 3.4 mV. The compression of BMS hydrogels treated with different voltages should be applied also in presence of cells to verify the effect of the piezoelectricity on the axon elongation. Future improvements with other piezoelectric molecules might be important to reach the physiological condition of resting potential

Moreover, the present work underlines the increase of the piezoelectric properties in SF hydrogels stimulated with 220 V and the apparent directionality of the SH-5YSY cytoplasm along the electric field lines. This is probably due to the intrinsic orientation of the dipoles in hydrogels as assumed by the simulation.

An interesting aspect that could be analysed is the analysis of the piezoelectric values during creep and relaxation compression tests. Indeed, the area under the piezoelectric curves show a clear difference that suggest different viscoelastic behaviour. These preliminary results have suggested a question: can the silk fibroin-based hydrogel reach the resting membrane potential -28 to -63 mV of a human sensory neuron? To answer this question a trial of four different concentration of SF solution (3%, 5%, 7% and 9% w/v) was performed with the set-up described above. The results reported in Table 6 show an increase of voltage at 7% equal to 6.5 mV for SF hydrogel stimulated with alternating current and 24 V. Moreover, the SF hydrogel treated with different electric field showed a different mechanical behaviour respect to the control that in the future could be investigated. Indeed, the piezoelectricity of the control 7% and 9% (7%C and 9%C) were not evaluated because the 15 % of deformation caused the break of the samples analysed. On the contrary, break of treated samples was not observed, thus indicating a clear effect of the applied electrical field on the hydrogel structure and properties. By the way, the increase of the SF concentration might cause problems of hypoxia to the human neural stem cells (hNSCs) in case of their encapsulation.

The following paragraph will show the biological effect of a 3% w/v BMS hydrogel on hNSCs

2.3 Biological effect of BMS hydrogel on hNSC

In collaboration with Martina Giancane, Laryssa Alves Borba**

**CIMeC - Center for Mind/Brain Sciences, University of Trento, Italy*

2.3.1 Introduction

The bio-inspired multifunctionalized silk fibroin (BMS) hydrogel was seen to be a suitable substrate for the MRC5 adhesion, migration and proliferation mimicking the role of BMs. The chemical structure of the BMS was inspired to the nidogen interaction with Col-IV and laminin that are involved during the neural tissue remodeling and the nerve formation. The BMS hydrogel represents the second layer of the adhesive patch, a bioactive layer where the human neural stem cells (hNSCs) may survive and differentiate into neurons. Preliminary biological evaluations were performed on BMS hydrogel loaded with hNSCs, whose viability was evaluated with a live and dead assay. In order to implement the capability of the BMS in axon elongation, a chemoattractive protein was inserted in a specific region of the BMS hydrogel creating a signal gradient. In the introduction of this thesis, we have described the role of the Netrin-1, one of the four axon guidance family proteins in addition to Slit, Ephrin and Semaphorin, able to attract or repel the growth cones toward a specific direction.

Netrin-1 is continuously expressed in the adult nervous system and it is generally present adjacent to the lesion in case of SCI. The DCC (deleted in colorectal cancer) receptor of differentiated hNSC is responsible for mediating the attraction response of axons to netrins. Netrins are particularly affine to the DCC receptors (RDCCs) but the UNC5B (un-coordinated-5 homolog) receptor is preferred when the RDCCs are saturated, promoting axonal repulsion¹⁶⁹. The presence of DCC was demonstrated by

immunostaining on hNSCs and the netrin effect on cells encapsulated into BMS hydrogels was also evaluated by a live and dead assay in order to observe an improvement of the axonal elongation. In order to understand the concentration of netrin perceived by hNSCs in a specific region of the hydrogel, a diffusion test was performed functionalizing the Netrin with a fluorophore conjugated by a click chemistry reaction. The gradient of netrin diffused was evaluated by Image J software considering a concentration of 300 ng/mL from the starting point of diffusion.

2.3.2 Materials and Methods

Netrin diffusion. Netrin G1 (12313-H08H-20) was conjugated with Azide Fluor 545 by using a click chemistry reaction. Briefly, 6 μ L of Netrin are mixed in 1 mL of PBS pH 7.4 to reach a final concentration of 600 ng/mL. The solution was mixed with 5 μ L of DBCO-NHS (50 mg/mL) and left to react at 4°C for 2 h. The product was dialyzed in a Slide-A-Lyzer Cassette (Pierce), MWCO 3500 Da against distilled water for 1 day. The precursor Netrin-DBCO was left to react spontaneously with 5 μ L of Azide Fluor 545 (10 mg/mL) in a water solution for 30 minutes and dialyzed in a Slide-A-Lyzer Cassette (Pierce), MWCO 3500 Da against distilled water for another 1 day. The dye-netrin (600 ng/mL) was mixed with an aliquot of the BMS solution already sonicated at 50% for 1 min to reach a final netrin concentration of 300 ng/mL. A small hole of 2 mm in diameter was created in the BMS hydrogel and poured with the dye-netrin/BMS. The diffusion is monitored by using a confocal microscope (Nikon Eclipse Ti-E) exciting the dye at 545 nm.

Expansion and differentiation of hNSCs. The hNSCs (H9 hESC-Derived, N7800-100) need to adhere on a specific coating for the expansion, generally, the CELLStart gives the best performance. Briefly, the stock solution of CELLstart is diluted 1:100 in D-PBS with Ca²⁺ and Mg²⁺, 7 mL of the working solution is poured in a T25 flask and left to react for 1 h at 37°C. After this period, the CELLstart is

removed and the hNSC are seeded at a density of 1.0×10^5 cells per cm^2 . The culture medium for the hNSCs expansion consists in the following composition:

Components	Concentration	Amount
KnockOut™ D-MEM/F-12	1X	97 mL
GlutaMAX™-I Supplement	2 mM	1 mL
bFGF	20 ng/mL	2 μg
EGF	20 ng/mL	2 μg
StemProR Neural Supplement	2%	2 mL

When the hNSCs reach a confluence of 90%, the culture medium is removed and a pre-warmed StemPro Accutase is poured for the cell detachment. The cells are recovered by centrifugation and seeded on TCP 24 well plate treated with a double coating of poly-L-ornithine and laminin, suitable for the cell differentiation. After 48 h, the medium is changed with the same medium composition described in the table except for the presence of growth factor for a spontaneous differentiation (Invitrogen protocol).

Expansion of MRC5. MRC5 were cultured in the following medium composition: MEM (Minimum essential medium) 87%, fetal bovine serum 10%, sodium pyruvate 1%, L-glutamine 2 mM 1%, antibiotic/antimycotic 1%, non-essential amino acids 1%. Cells were cultured in T-75 cell culture flasks (Corning, New York) at standard culture conditions of 37°C, and 5% carbon dioxide. Cell adhesion and spreading were evaluated on 96 well plate in duplicate to observe any aspecific bond of the anti-DCC compared to the immunostaining performed on hNSCs.

Immunocytochemistry preliminary analysis. The TCP samples were washed by D-PBS containing Ca^{2+} and Mg^{2+} and fixed with 4% fresh PFA for 15 minutes, paying attention to maintain covered the

differentiated cell from the air. After washing, a blocking buffer (5% serum of the secondary antibody host species, 1% BSA, 0.1% Triton-X in D-PBS with Ca²⁺ and Mg²⁺) was poured and left to react for 30-60 minutes. After blocking buffer removal, cells were incubated overnight at 4°C with primary antibody (Rabbit pAb to DCC, ab196598) diluted in 5% serum. After washing, cells were incubated with fluorescence-labeled secondary antibody (A32740, Thermofisher) (5% serum in D-PBS with Ca²⁺ and Mg²⁺) in the dark at 37°C for 30–45 minutes. After washing, the cells were ~~also~~ stained with DAPI solution (3 ng/mL) for 5 minutes and Oregon Green for 45 minutes, and rinse with D-PBS. The control is represented by undifferentiated hNSCs and MRC5 fibroblast cell line to compared cells that not show DCC receptor. The MRC5 were expanded by using the culture medium described in Section 2.1.2.

Axons observation with cell viability assay. The viability of the hNSCs on TCP and encapsulated in hydrogels (maximum thickness of 1.5 mm) was investigated by live/dead assay (Life Technologies). Dead cells were stained by a propidium iodide (PI) solution (20 µg/ml in PBS) for 2 minutes at 37°C in the dark. Cells/hydrogel were washed in phosphate-buffered saline (PBS) and then incubated in calcein AM/PBS (2 µM) at 37 °C for 30 min. The cells were then washed three times in PBS and observed by confocal microscopy (Nikon Eclipse Ti-E). The Live and Dead assay allows the monitoring of the netrin effect on axon elongation of hNSCs.

2.3.3 Results and Discussion

The survival and behavior of the hNSCs encapsulated into BMS hydrogels were evaluated in order to verify the suitability of the substrate in hosting the hNSCs and promoting the elongation of the axons along a signal gradient.

The DCC receptors are attracted by the presence of netrin but repelled when the receptors are saturated. Thus, the behaviour of hNSCs was studied in presence of netrin considering its diffusion rate. Netrins were functionalized with a dye by means of a click chemistry reaction that ensures an efficiency near the 100 %. The sonicated solution of BMS was mixed with dye-netrin to a final concentration of 300 ng/mL that seems an optimal amount to attract the growth cone of hNSC towards the source of netrin ¹⁷⁰. The dye absorption (Azide fluor-545) at 546 nm allows the visualization of the netrin diffusion by confocal imaging. The confocal images reported in [figure 32](#) show a fast diffusion of netrins into the BMS hydrogel in presence of culture medium after 24 h. The diffusion rate was calculated to be 334.9 $\mu\text{m}/\text{h}$. Thus, the axons of differentiated hNSCs seems to be repelled near the source of netrin and directed towards a lower concentration of netrin ([Figure 35](#)). The netrin diffusion through the hydrogel was evaluated separately from the live and dead assay, which is used to visualize the hNSCs viability, to avoid a signal overlapping with the PI staining.

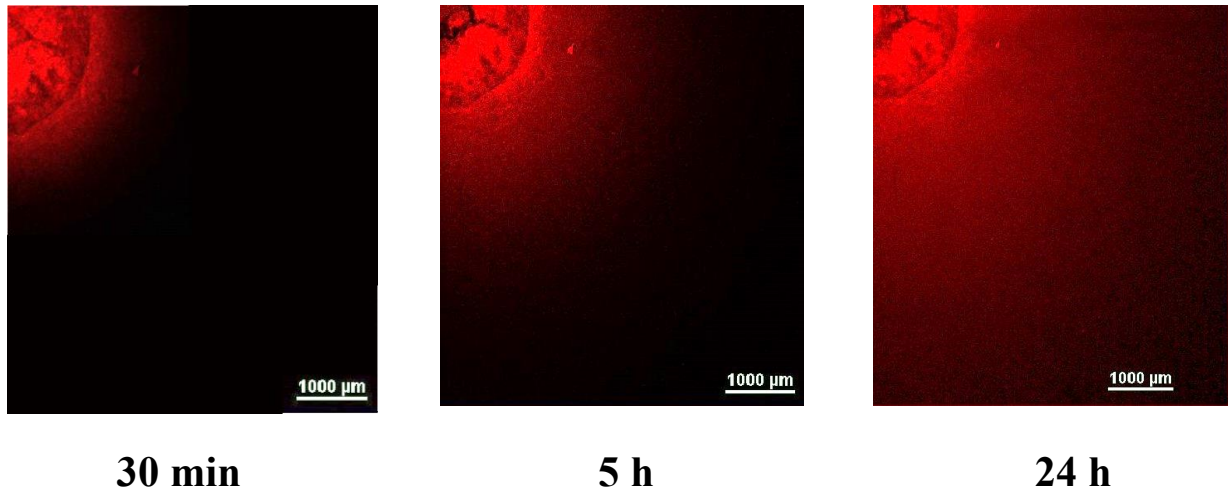


Figure 32. Dye-netrin diffusion.

The presence of RDCC in hNSCs were evaluated by Anti-DCC immunostaining that revealed the presence of the receptors already on undifferentiated hNSCs (day 0: day of changing medium from expansion to differentiative one). At day 3 the signal was seen to decrease near the nucleus (Figure 33), instead, it seems to increase near the growth cone (Figure 34). The MRC5 were used as negative control for checking the presence of false positive signals due to aspecific bond of the Anti-DCC.

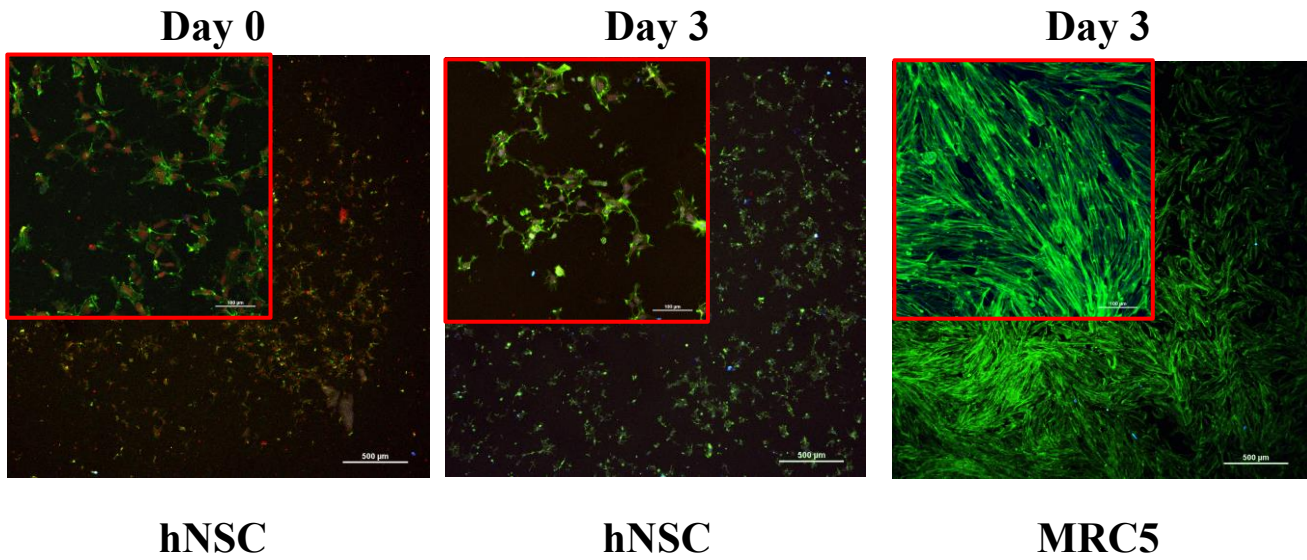


Figure 33. Anti DCC immunostaining highlights the presence of DCC receptor near the nucleus of undifferentiated hNSCs and a decrease of the signal in the differentiated stage. The staining on MRC5 reveals the absence of DCC receptor.

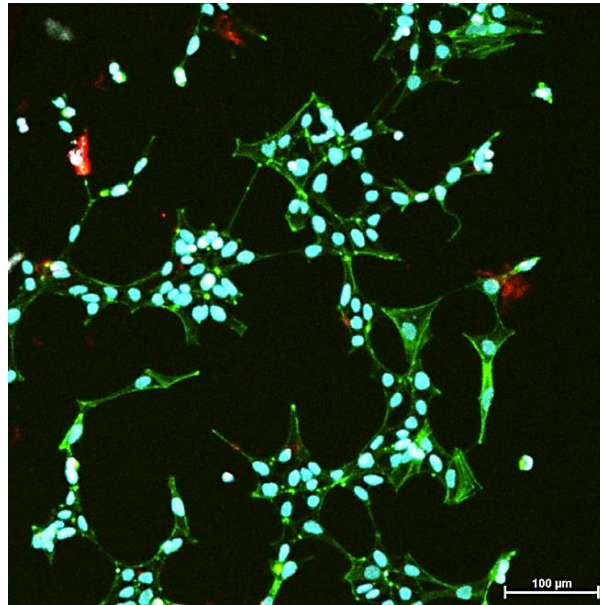
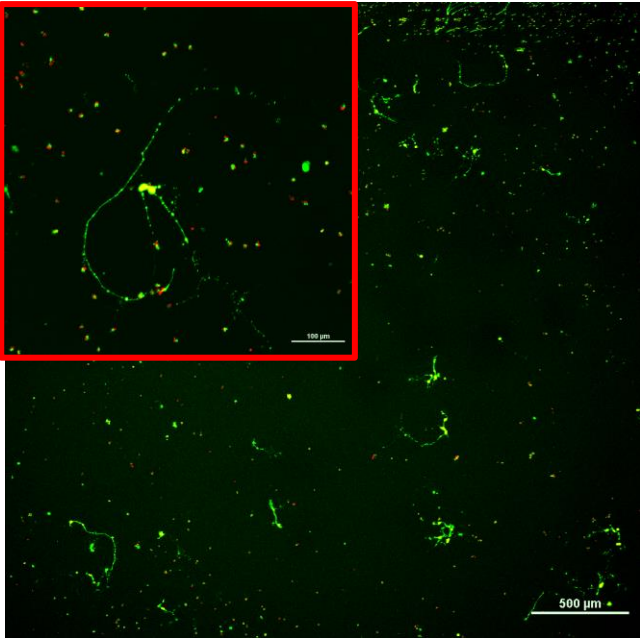


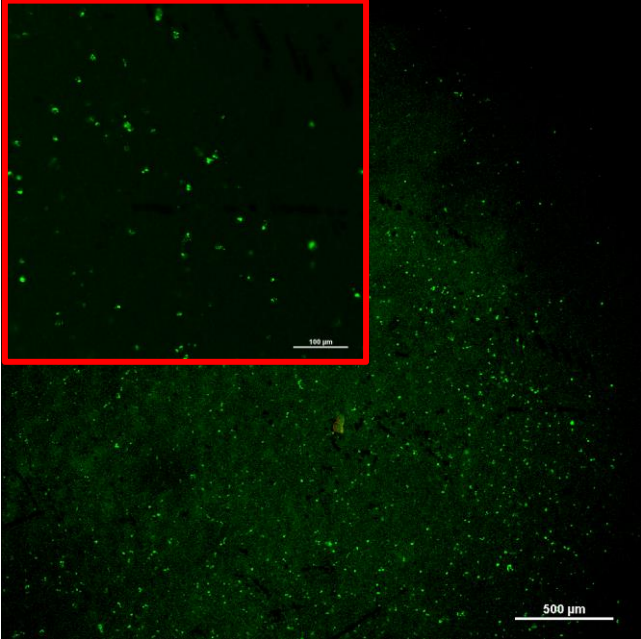
Figure 34. Anti-DCC staining on hNSCs 3 days after the addition of the differentiative medium change. The red signal is due to the presence of DCC receptor near the growth cone, the green staining refers to the Oregon Green staining for the cytoskeleton and the blue one to the DAPI that highlights the nucleus.

The viability of hNSCs was observed also on TCP where the axon elongation is clearly visible with the calcein staining after 5 days (Figure 35). Inside the hydrogel, the axons stained with the calcein are less visible than the TCP due to scattering and absorption phenomena. By the way, it is possible to distinguish axons elongation also through the BMS hydrogels.

TCP Day 5



BMS w/o Netrin Day 5



BMS with Netrin Day 5

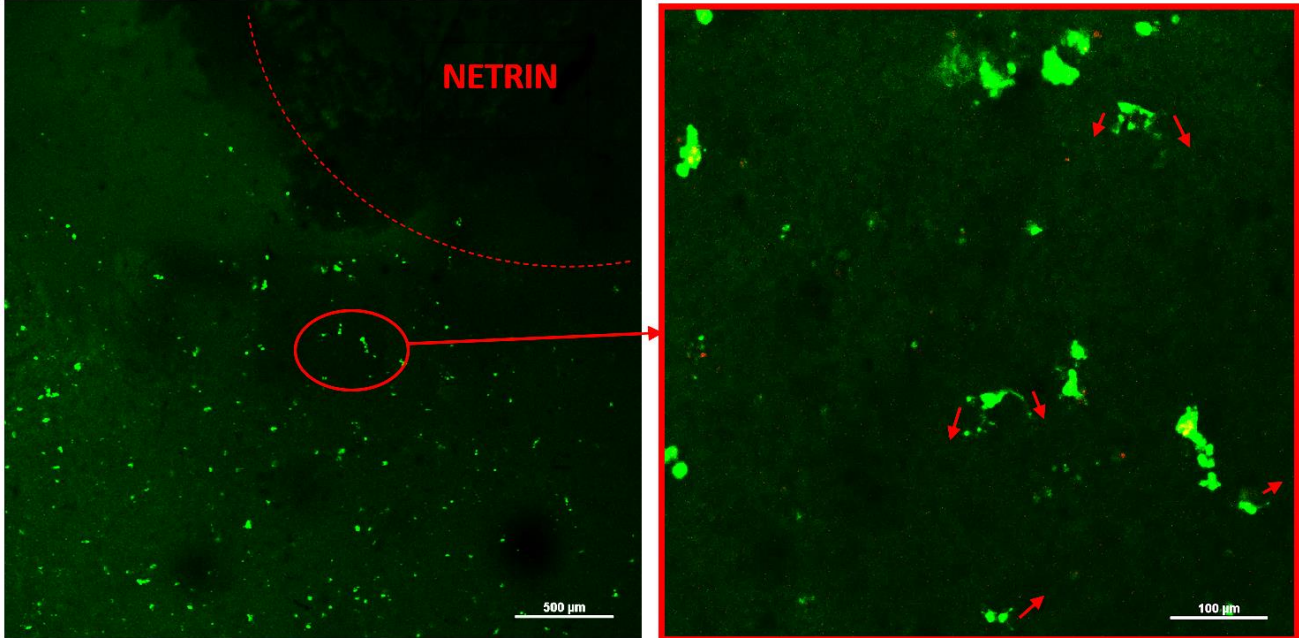


Figure 35. Live and Dead staining of hNSCs on TCP, hNSCs encapsulated into the BMS hydrogel with

and w/o the presence of netrin.

2.3.4 Conclusions

In this work, we have demonstrated that the BMS hydrogel is suitable for hNSCs encapsulation and the presence of netrin seems to help and promote the axon elongation more than the BMS w/o netrin. By the way, the experiment should be repeated by using a hydrogel thickness less than 500 μm to reduce the noise/signal ratio during the confocal analysis. Moreover, the functionalization of the BMS with netrin could be an option to reduce the netrin diffusion rate instead of a blend between BMS and netrin. Indeed, the use of the dye-netrin complex mixed with the BMS solution showed a homogeneous distribution after 24 h removing the driving force useful to guide the axon towards the source of netrin. Indeed, the attenuation of the netrin gradient caused axons elongation along random directions, thus, a stronger conjugation of netrins on BMS hydrogel is recommended.

The following chapter describes the use of BMS in alternative approaches for the SCI treatment.

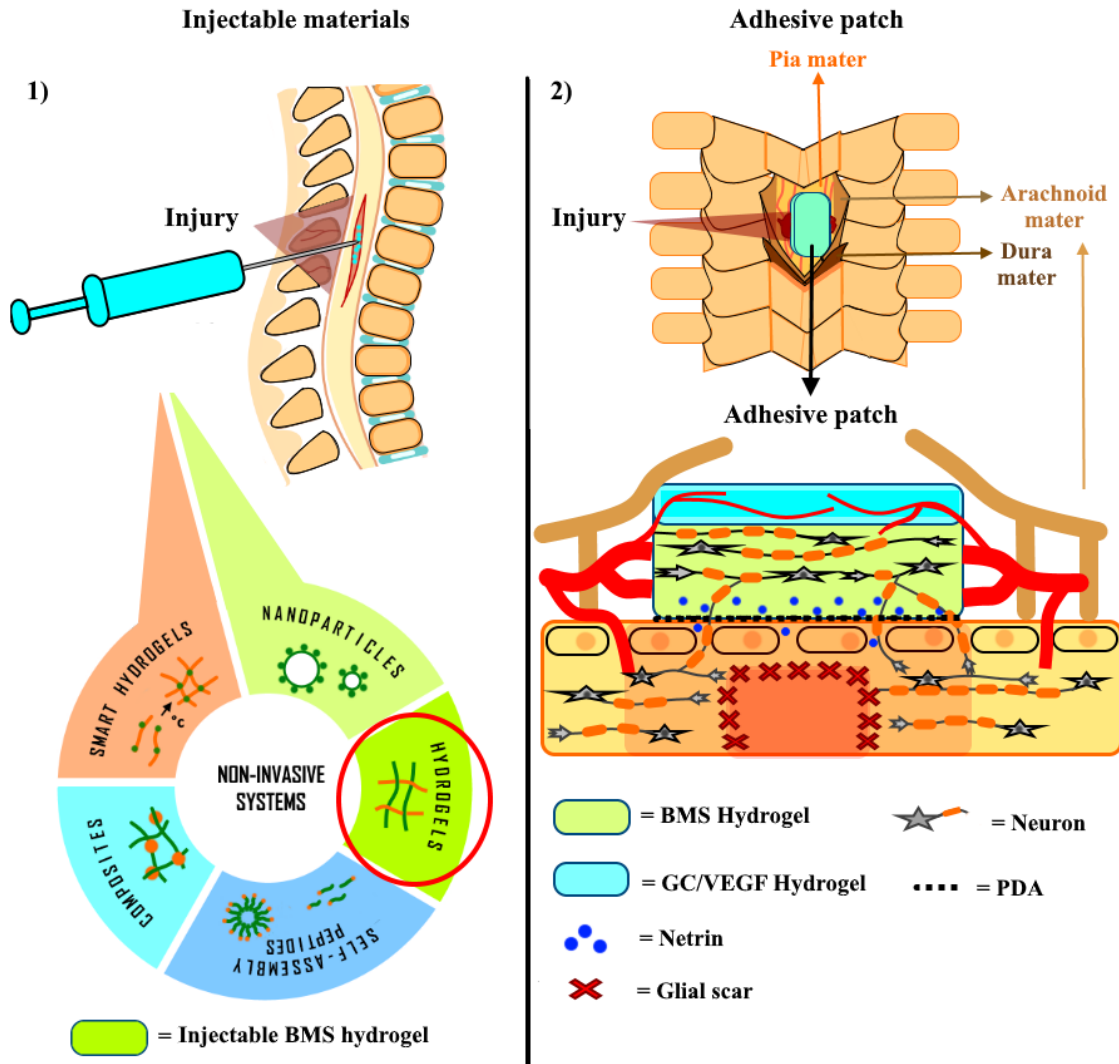
Chapter 3

BMS-based alternative approaches for spinal cord regeneration

Bioengineered scaffolds can create an enhancing environment for the spinal cord regeneration contributing to the neural repair. For example, agarose scaffolds were widely studied and templated into precise linear arrays in order to organize the growth of the axons and enhance the extension of descending or ascending axons into a lesion site ¹⁷¹. The implantation of agarose scaffolds provided for an invasive removal of the cyst with a continuous intraoperative neuroelectrophysiological monitoring during the surgery to avoid further damages to the tissue. NeuroRegen scaffolds, instead, are linearly ordered collagen scaffold functionalized with nerve regenerative molecules, that were tested clinically and transplanted into the spinal cord following scar tissue resection ¹⁷². The results showed a partial shallow sensory and autonomic nervous functional improvements, but no motor function recovery was observed. Many studies^{173,174}, are considering the key roles of the glial scar in the recovery of SCI rather than its removal. Indeed, under specific conditions the glial scar may serve as a bridge for axonal growth and the complex procedure for its removal could be avoided.

Researchers are pushing towards solutions avoiding further damages to the tissue. In particular, here we will present a minimal invasive solution based on BMS injectable scaffolds (Figure 36-1). On the other hands, a solution based on adhesive patches that avoid damages to the spinal cord while exposing the tissue after a laminectomy (Figure 36-2).

ALTERNATIVE APPROACHES FOR SCI REPAIR



Can the movement of the spinal cord generate a potential variation inside the hydrogel?

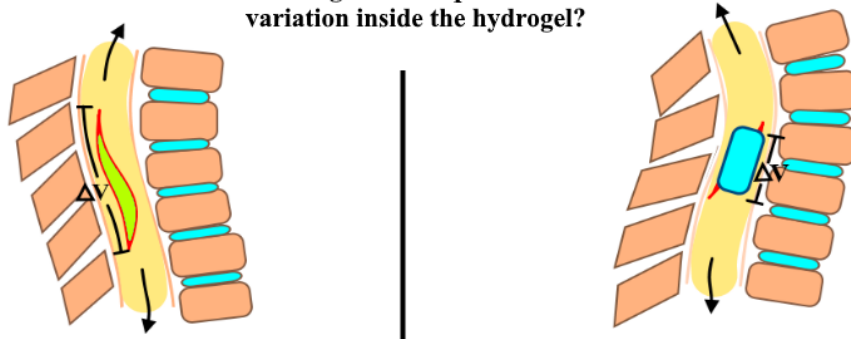


Figure 36. Schematical explanation of two different approaches for SCI repair.

3.1 Minimal invasive approach by using an injectable BMS hydrogel

Minimally invasive injectable biomaterials (MIIB)¹⁷⁰ can be precisely positioned in the lesion site, and eventually repetitively injected to obtain the complete regeneration of the tissue. The repetitive injection may reprogram the glial scar and/or create a persistent matrix that support the cell growth (Figure 11-1). The silk fibroin-based polymers are used to gel by the following physical cross-linking: self-assembly, ultrasonication, shearing, electric field action, temperature change, pH adjustment, use of organic solvents or use of surfactants¹⁷⁵. The ultrasonication was used to create the BMS hydrogels but it represents a method difficult to be controlled in term of gelation time. Recently a blend of two different silk fibroin solutions derived from *Bombyx mori* (BM) and non-mulberry silkworm *Antheraea assama* (AA)^{176, 177} was used to self-assembly at 37°C after their injection. It was observed that the gelation time decrease with the increase of the ratio BM/AA and it is characterized by three stages: pre gelation, gelation and hardening stage. The injection should be performed during the gelation stage and should take 15-30 min following the ratio of BM/AA reported by M. Kumar et al. Future investigations could be focused on biocompatible self-assembly that can be mixed with the BMS to allow the gelification after injection. The injection of BM/AA blend was demonstrated to have an excellent compatibility with endothelial cells supporting their viability and functions¹⁷⁷. Instead, a faster gelation of the SF-based polymer was also demonstrated mixing a stock solutions of SF (6% w/v) in water and variable ratios (10–40%) of biocompatible additive such as ethylene glycol (EG), and triethylene glycol (TEG), at room temperature. Also the mixed of SF/EG/TEG was demonstrated to be suitable for fibroblast cells viability¹⁷⁸. The described methods could be used to control the BMS gelation and its injectability for future application in spinal cord regeneration.

3.2 Adhesive patch

The MIIB limitations can be overcome by an alternative approach that avoided the cyst removal or further damages to the tissue. Indeed, MIIBs investigated up to now lack the capacity to stimulate electrically the neural tissue and a controllable 3D structure formation with different compositions. As we have reported several times, the electrical stimulation of the cells i) helps the survival and maintains the cells active^{50,51}, ii) promotes long-distance axonal elongation⁵², and iii) achieves oriented axons regeneration⁵³ for a natural tissue structure. Indeed, a potential is always present in the neural tissue, for example, the resting membrane potential of dorsal root ganglion cells is around -28 to -63 mV¹⁷⁹, the excitatory postsynaptic potential of the hippocampal CA1 region is around 12 mV, as well as the voltage measured after hyperpolarization (AHP) of around 5.4 mV in native conditions¹⁶⁸.

Thus, an adhesive patch based on a piezoelectric BMS represents an alternative approach that might be used as a bypass to restore the neuronal signal and avoid an external power supply, which might cause infections. The designed adhesive patch is a multilayer hydrogel with piezoelectric properties that acts as a bridge between the healthy parts surrounding the injury. The multilayer hydrogel consists of:

- i) a thin-layer of gelatin and fish collagen functionalized with vascular endothelial growth factor (VEGF);
- ii) a layer of a bio-inspired multi-functionalized silk fibroin (BMS) hydrogel with piezoelectric properties loaded with a chemoattractive protein (Netrin-1);
- iii) the third one made of a thin layer of polydopamine (PDA).

The first layer is mainly composed by collagen type 1 and 3, which represent the main components of the pia mater. This layer may induce the cells of the pia mater to populate the hydrogel and restore a vascularized layer for the gas and nutrients exchanges essential for the survival of the neurons. The BMS hydrogel, instead, consists of silk fibroins conjugated with collagen type IV (Col-IV) and laminin peptides IKVAV, which promote the cell adhesion and differentiation into neurons. Moreover, the

presence of a resting potential may help the cell survival and axon elongation. The second layer is also loaded with netrins, important for the sprouting of axons, which are located near the injury, towards the BMS hydrogel in order to restore a neural signal processing.

The third layer, instead, consists of an adhesive polymer called polydopamine (PDA) important for the patch fixation on the site damaged. Thus, the following paragraph will describe the first layer whereas the second one was characterized in depth in the previous sections. By the way, the combination of the layers was not investigated leaving the curiosity to make further analysis in the future.

3.2.1 A thin layer hydrogel of gelatin and fish collagen functionalized with VEGF for blood vessels formation

In collaboration with professor Gilson Khang laboratory*

* Department of Engineering of Chonbuk National University (Jeonju, South Korea)

3.2.1.1 Introduction

The first layer of the adhesive patch was realized starting to consider different natural polymer that could facilitate the integration of the multilayer hydrogel into the injured site. Water solutions of Col-I: fish collagen, SF: silk fibroin, pol: sodium alginate, GE: gelatin and HA: hyaluronic acid were mixed physically crosslinked to create hydrogels with or without the addition of EDC/NHS, by sonication, freeze/thaw, temperature or pH changes. The best composition was selected evaluating different parameters as indicated in the followings: production feasibility, cytotoxicity, metabolic activity and viability of corneal endothelial cells (CECs), selected because they have the same origin of the meninges (the corneal endothelium is derived from the neural crest¹⁸⁰. Indeed, CECs derive from the neural crest and could mimic the behavior of the cells of the pia mater. The best composition based on natural materials was functionalized covalently with vascular endothelial growth factor (VEGF) to induce the angiogenesis. A releasing ELISA test was performed to evaluate the conjugation efficiency of VEGF and the results were compared with the data acquired from a degradation test on the same material. The selected material represents the layer that can guarantee the gas and nutrients exchanges to the cells encapsulated into the adhesive patch preventing their survival. The selected material was submitted also to a preliminary *in vivo* evaluation, implanting the selected biomaterial in Sprague-Dawley rats under the skin. All the animal experiments were performed in accordance with the guidelines and approval of Chonbuk National University Animal Care Committee, Jeonju, Republic of Korea (CBNU 2016-50). The surgery proceeded under general anaesthesia (Dormitor/Alfaxan), and all attempts were made to

minimize animal suffering. A histological evaluation with H&E (hematoxylin and eosin) stain and anti-vWF (Anti-von Willebrand Factor) stain was also performed to verify the vessels formation and, eventually, an inflammatory response.

3.2.1.2 Materials and Methods

Hydrogels preparation. The following aqueous solutions were prepared as 2% w/v SF, 10% w/v Gelatin, 2% w/v Sodium Alginate (Pol) and 2% w/v for high and low molecular weight of hyaluronic acid (HA and LWHA). The combinations between these natural materials were performed just blending the stock solution with the ratio reported in the [Table 6](#). The SF based hydrogels were made by sonication, the GE based hydrogels were performed dissolving in water the porcine skin gelatin at 60 °C and cooling the temperature up to 25°C. The Pol based hydrogels were made preparing a disk of gelatin containing Calcium Chloride (200 mM) in a 10 cm Petri dish. The Pol solution was poured on the gelatin disk up to gelification. The HA hydrogels were performed with the following procedure: i) prepare a 2% w/v of HA in ddw and regulate the solution with HCl 1M to reach a pH 2, ii) dialyze the solution in ddw for 1 day, iii) the solution was poured in a 10 cm petri dish and iv) the sample was submitted to continuum freezing/thawing cycling up to gelation¹⁸¹. For Col-I and LWHA hydrogels cycling of freezing/thawing, temperature change or pH, and sonication did not promote any gelation thus Col-I based hydrogels were produced linking the Col-I with EDC/NHS to SF or GE or Pol.

The solutions of each material were sterilized with a 0.2 um filter and the gelation was conducted in sterile conditions in a biological hood.

Table 6. Design of experiment.

	Silk Fibroin (SF)	Gelatin (GE)	Collagen type I (Col-I)*	Hyaluronic acid (HA)	Low weight Hyaluronic acid (LWHA)	Polysaccharide (Pol)
Silk Fibroin (SF)	SF/SF	SF/GE (Ratio: 70/30 50/50 30/70 w/w)	SF/Col-I (Col-I: 2 mg/mL)	SF/HA (Ratio: 7/1 80/1 w/w)	SF/LWHA (Ratio: 100/1 w/w)	SF/Pol (Ratio: 70/30 50/50 30/70 w/w)
Gelatin (GE)		GE/GE	GE/Col-I (Col-I: 2 mg/mL)	GE/HA (Ratio: 7/1 80/1 w/w)	GE/LWHA (Ratio: 100/1 w/w)	GE/Pol (Ratio: 70/30 50/50 30/70 w/w)
Collagen type I (Col-I)*			Col-I/Col-I	Col-I/HA (Ratio: 7/1 80/1 w/w)	Col-I /LWHA (Col-I: 2 mg/mL)	Col-I /Pol (Col-I: 2 mg/mL)
Hyaluronic acid (HA)				HA/HA	HA /LWHA (Ratio: 70/30 50/50 30/70 w/w)	HA /Pol (Ratio: 7/1 80/1 w/w)
Low weight Hyaluronic acid (LWHA)					LWHA/LWHA	LWHA /Pol (Ratio: 100/1 w/w)
Polysaccharide (Pol)						Pol/Pol

CECs culturing. CECs were cultured on a cell culture dish for 1 day at 37 °C with a humidified 5% CO₂ incubator and the following medium composition: EBMTM-2 Basal Medium (CC-3156) and EGMTM-2 SingleQuotsTM Supplements (CC-4176). After 1 day, the medium was changed and again every 3 days up to 80% of confluence. At passage 1, the cells were used for the study.

Cell viability assay. MTT 3-(4,5-dimethylthiazol-2-yl)-2,5-diphenyltetrazolium bromide is reduced by NAD(P)H-dependent cellular oxidoreductase enzymes of viable cells to produce formazan, which has a

purple color. In each sample was added 100 uL of MTT working solution (5 mg/ml in phosphate buffered saline) after medium culture removal. After 3 hours of incubation at 37 °C the MTT was removed and 100 ul of DMSO was left to react overnight to allow the formation of purple formazan. Each solution was poured in a 96 well and a microplate reader was used to measure the absorbance at 570 nm.

Cell metabolic activity. (See protocol of section 2.1.2).

Live/dead cell assay. (See protocol of section 2.3.2). The CECs viability was performed on cylindrical hydrogels of the selected material (4 mm in diameter and 500 um of high) in duplicate.

In vitro VEGF release and degradation test. The selected material was functionalized with VEGF and cut in disks of 8 mm of diameter and 500 um of high and placed in a 48 well plate. Each disk was covered with 200 ul of PBS solution and incubated for 0-1-3-12-24-72-120-240 h at 37 °C. The suspension of each sample was collected for the enzyme linked immunosorbent assay (ELISA assay). The degradation test was performed on the same kind of sterilized samples. After the same period of time, the solution of each sample was collected and a sensitive thermogravimetric analysis (balance precision: 0.002 mg) was performed on each solution to evaluate the amount of material release after 10 days.

Immunohistochemistry. Cryosection preparation and staining was described in detail by Koshy et al.¹⁸². Briefly, samples were fixed in 4% PFA in DPBS at room temperature for 20 min. The gels were washed three times in DPBS and placed in a 30% (w/v) sucrose in DPBS solution overnight at 4 °C. Cryogels were then incubated at room temperature in a 15% (w/v) sucrose + 50% of Optimal Cutting Temperature (OCT) compound (Tissue-Tek) for 4 h, and then neat OCT for 4 h. Gels were frozen in OCT on dry ice. The frozen blocks were sectioned at -20 °C into 20 µm sections on a Leica CM1950 cryostat. The matrix was removed with baths of different percentage of ethanol (70, 80, 90, 100), with a Dako pen the board of the slice was confined. A drop of pepsin solution (1.5 mg/mL in distilled water) was poured on each

slice and left to react for 20 min. The slices were washed with distilled water for 1 minute and a drop of 3% of hydrogen peroxide solution was left to react on each sample. After 10 min, they were washed with water and a second one with citrate buffer (sodium citrate dihydrate 0.08 M, citric acid 0.01M in ddw) for 2 min. A pre-blocking solution was left to react for 15 min and a drop of primary antibody Anti-von Willebrand Factor (Thermofisher, AB7356) was poured overnight at 4°C. The primary antibody was recovered and the sample washed with water. The HRP-DAB was used for the IHC-select detection. Instead, H&E staining (haematoxylin and eosin) was used to show cytoplasm stained pink-orange and nuclei stained darkly, either blue or purple.

3.2.1.3 Results and Discussion

Cells cultivated on the hydrogel based on GE/Col-I showed the highest metabolic activity after 14 days (Figure 37). Also, the SF and SF/Col-I showed a good metabolic activity and viability (Figure 38) but SF-based hydrogels were partially degraded after 14 days and difficult to be handled. By the way, the functionalization with Col-I by using EDC/NHS method seems to stabilize the biomaterial based on SF or Ge. MTT and Alamar were performed only on SF, SF/Col-I, SF/pol, pol, GE, GE/HA and GE/Col-I hydrogels because the other ones showed different problems: inconsistent hydrogel formation, fast degradation after 1 day of incubation at 37 °C, absence of metabolic activity or viability after 3 days of incubation or no hydrogel formation. A summary of the results obtained from Alamar Blue, MTT assay and process production are reported in the Table X. The live and dead images of the cells seeded on the selected material, GE/Col-I (Figure 48), were obtained by using a Super Resolution Confocal Laser Scanning Microscope that highlights the homogeneous distribution and cell viability on Ge/Col-I hydrogels. Moreover, the cell shape suggests a strong adhesion on the substrate already at day 1.

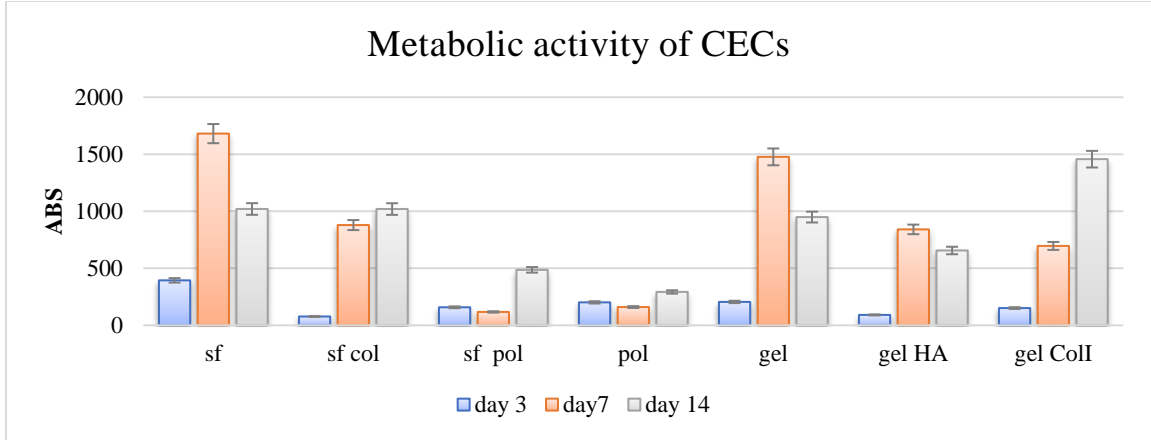


Figure 37. Alamar blue staining Cell metabolic activity evaluated by Alamar blue staining assay of a 2D hydrogel of the rabbit CECs after 3-7-14 days after seeding.

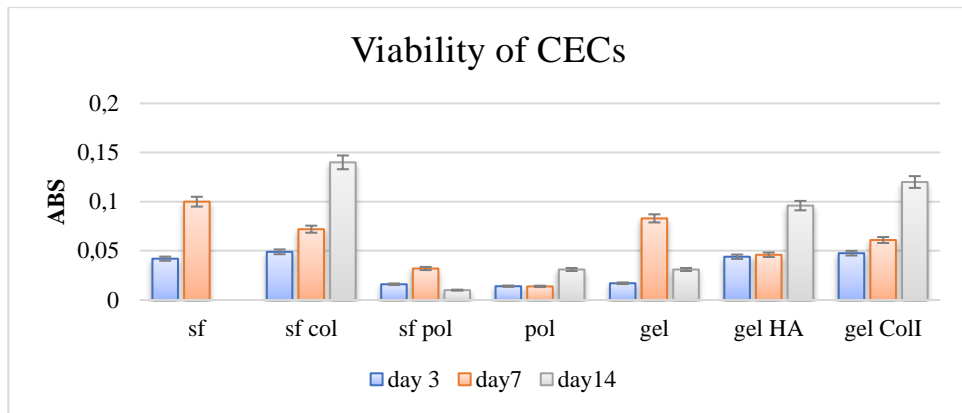
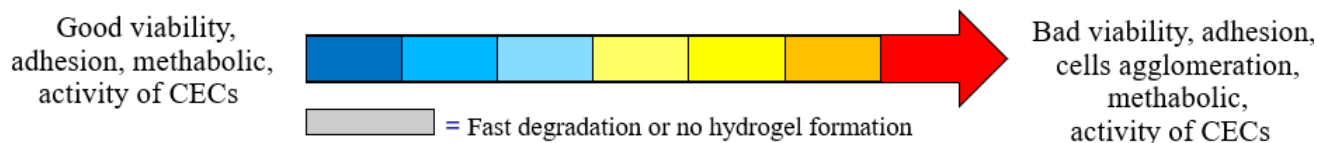


Figure 38. Cell viability evaluated by MTT staining assay of a 2D hydrogel of the rabbit CECs after 3-7-14 days after seeding.

Table 7. Summary of the results obtained for each natural material of the DOE.



DOE	Silk Fibroin (SF)	Gelatin from porcine skin (GE)	Fish Collagen (Col-I)	Hyaluronic acid (HA)	Low weight Hyaluronic acid (LWHA)	Sodium Alginate (Pol)
Silk Fibroin (SF)	SF/SF	SF/GE (Ratio: 70/30 50/50 30/70 w/w)	SF/Col-I (Ratio: 7/1 80/1 w/w)	SF/HA (Ratio: 7/1 80/1 w/w)	SF/LWHA (Ratio: 7/1 80/1 w/w)	SF/Pol (Ratio: 70/30 50/50 30/70 w/w)
Gelatin (GE) From porcine skin		GE/GE	GE/Col-I (Ratio: 7/1 80/1 w/w)	GE/HA (Ratio: 7/1 80/1 w/w)	GE/LWHA (Ratio: 7/1 80/1 w/w)	GE/Pol (Ratio: 70/30 50/50 30/70 w/w)
Fish Collagen (Col-I)			Col-I/Col-I	Col-I/HA (Ratio: 70/30 50/50 30/70 w/w)	Col-I /LWHA (Ratio: 7/1 80/1 w/w)	Col-I /Pol (Ratio: 7/1 80/1 w/w)
Hyaluronic acid (HA)				HA/HA	HA /LWHA (Ratio: 7/1 80/1 w/w)	HA /Pol (Ratio: 7/1 80/1 w/w)
Low weight Hyaluronic acid (LWHA)					LWHA/LWHA	LWHA /Pol (Ratio: 7/1 80/1 w/w)
Sodium Alginate (Pol)						Pol/Pol

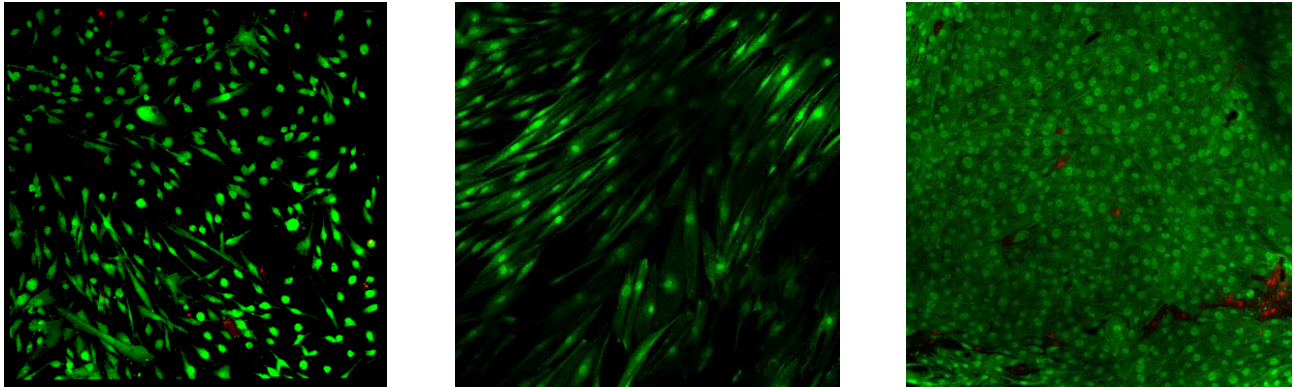


Figure 39. Live/dead staining of a 2D hydrogel of the rabbit CECs after 3-7-14 days.

The selected hydrogel of GE/Col-I was conjugated with 3 ng/mL of VEGF by EDC/NHS method. The VEGF release was evaluated in order to verify the conjugation between the growth factor and the material. Moreover, the release test gave the possibility to verify the presence of VEGF available into the material after 10 days of incubation (Figure 39), comparable with the *in vivo* test results. The VEGF release was compared also with the degradation test data of GE/Col-I samples to verify if the VEGF release is due to the material degradation or to a weak chemical conjugation. From the results highlighted in figure 49, the release of VEGF seems to follow the degradation of the material and the amount of VEGF release is around 0.12 ng/mL after 10 days.

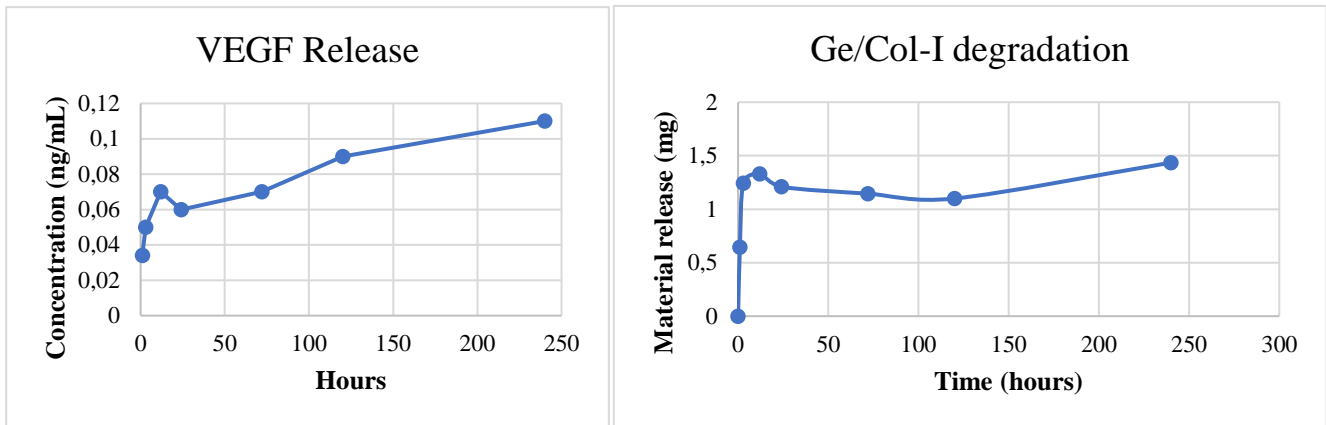


Figure 40. VEGF release (left) and degradation test (right).

The effect of VEGF is also visible by using the Anti-vWF stain in slices of Ge/Col-I/VEGF after 10 days of subcutaneous incubation in male rats compared to slices of Ge/Col-I without VEGF (Figure 41). However, shorter vessels are also present in Ge/Col-I sample showing a spontaneous vascularization induced by the material. From the H&E staining, a migration of adipose cells inside the hydrogel is observed but it is also visible an inflammatory reaction, probably due to the implantation procedure.

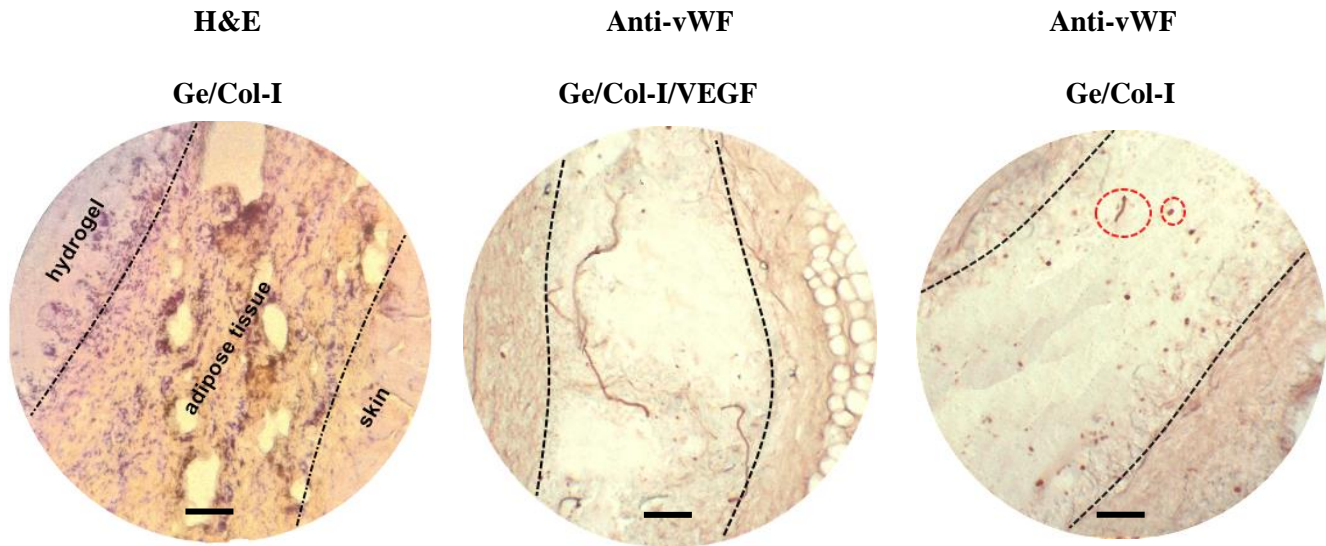


Figure 41. Immunohistochemical analysis by using H&E and Anti-vWF staining after 10 days of incubation of Ge/Col-I based material inserted subcutaneously in male rats. Scale bar of 200 μ m.

3.2.1.4 Conclusions

The biological evaluations performed on different natural material and their combination highlighted a preferential growth of CECs on GE/Col-I as well as on SF/Col-I hydrogels. By the way, the first ones were selected for a slow degradation respect to the SF based samples. Moreover, the release of VEGF conjugated with the selected material shows a trend similar to the degradation test performed on the same material suggesting the presence of a VEGF signal for the entire lifetime of the GE/Col-I hydrogel. Moreover, the *in vivo* results showed the presence of blood vessels, aim of this work. By the way, the data acquired has to be repeated to verify the reproducibility.

Chapter 4

Future perspectives

As mentioned before, vehicle crashes, followed by falls and cases of violence are the main causes of the spinal cord injury (SCI) that lead to permanent functional and sensory loss. A fast action to alleviate secondary injuries can improve the efficiency of the SCI treatment. The clinical procedure of neurorestoration regards, for example, active and passive movements, cell therapies, early rehabilitation, or electric stimulation^{183,14}. Instead, the clinical guidelines for the neuroprotection regard the administration of pharmacological therapy to avoid cellular apoptosis or necrosis and promoting neuronal survival¹⁸⁴. Nowadays, the treatments used to regenerate the tissue and restore the neural signal are generally invasive and moderately effective, however a combinatorial and interdisciplinary approach could lead to find new solution for the SCI treatment. Most of the treatments provide for large incisions with high risks to damage other tissues, pain for the patient and large costs for the healthcare system mainly for the hospital. Minimally invasive materials for the SCI treatment acquired great interest in the last decade because they provide for minimally invasive implantation procedures and present shape versatility. Many of these materials possess water retention, stiffness comparable to the human spinal cord and biocompatibility. They can be functionalized with different bioactive molecules to mimic the ECM and improve the cell adhesion on the material. This latter represents one of the main important factors for the cell survival that is neglected with the only cell therapy. Another important requirement seems to be the electrical stimulation, which maintains the cells active and helps their survival, promoting long-distance axonal elongation and achieving oriented axons regeneration for a natural tissue structure⁵².

The electrical stimulation is generally performed by using external power supply but infections are not negligible or by using a microelectrode array with a micro-stimulation system. This system shows risks during the invasive implantation and it can also cause problems such as muscle fatigue, stimulation spillover, a reversal of the recruitment pattern typically associated with voluntary muscle activation and in some cases lesion of the tissue due to the weight of the device in direct contact with the spinal cord. By the way, these kinds of systems show the best long-term solution to achieve limb reanimation¹⁸⁵. Nowadays, there is no biocompatible materials that can be implanted in a non-invasive manner and can avoid to be externally electrically supplied.

The BMS was designed to mimic the basement membrane for cells adhesion, migration, proliferation and differentiation of the hNSCs. The BMS hydrogel was demonstrated to be a suitable environment for neurons and exhibit piezoelectric properties under small deformation. These characteristics make it a promising candidate for further analysis and investigations.

In the future, it could be interesting to study the adhesive patch assembling all the components (BMS, Ge/Col-I, netrin and PDA) previously described and verify its performance with *in vivo* testing with and without the application of small deformation to induce piezoelectricity in the system. The secondary aspect to investigate could be the conditions of BMS injectability to allow the in-situ jellification. The injectability of BMS could allow its application in the body through minimally invasive procedure, which is the main characteristic to overcome for clinical complications. After the optimization of BMS injectability, we might observe the survival and behaviour of hNSCs with and without the application of the mechanical deformation. The challenge will be the study of BMS piezoelectricity as an injectable hydrogel.

Supplementary materials

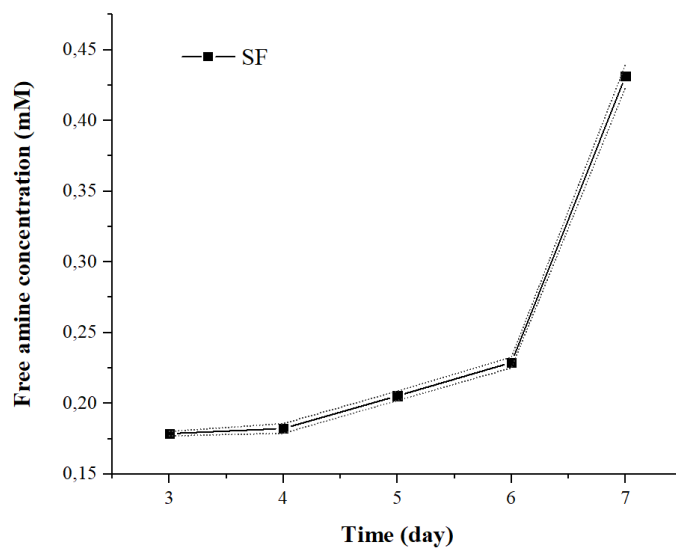


Figure S. 1. Measured evolution of the SF free amine groups after 7 days of dialysis.

	PDI	SIZE (nm)
D3	0,525	53,96
D4	0,61	79,27
D5	0,264	103,4
D6	0,281	114,7
D7	0,394	178,2

Table S. 1. DLS analysis of SF solution dialyzed from day 3 (D3) up to day 7 (D7). The analysis starts from D3 in accordance with the beginning of the conjugation reactions.

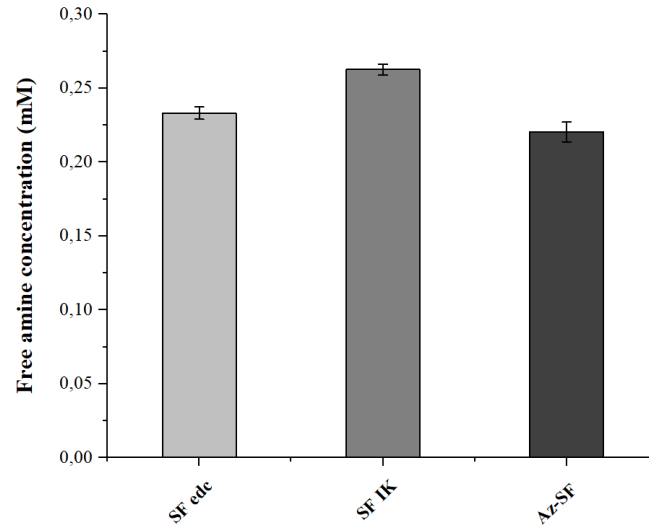


Figure S. 2. Silk fibroin FAC evolution after EDC/NHS adding (SF edc), after coupling reaction of IKVAV (SF IK) and after diazonium coupling to form Azide SF (Az-SF).

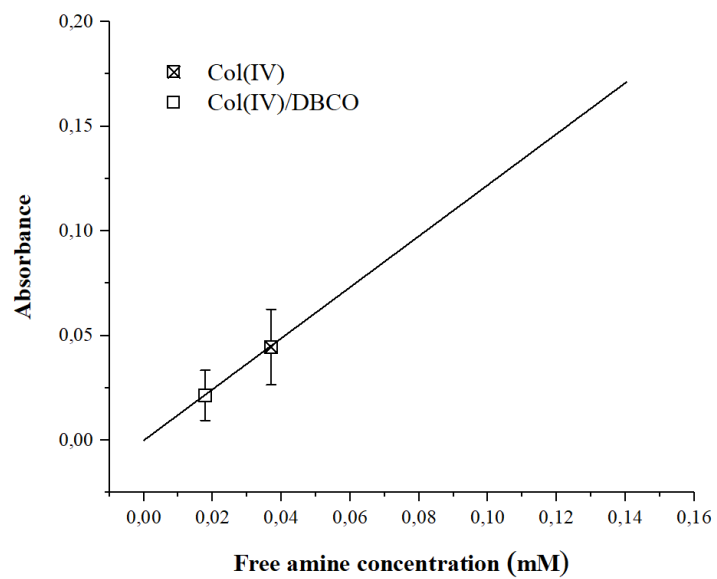


Figure S. 3. Efficiency of the coupling reaction between Col(IV) and DBCO groups.

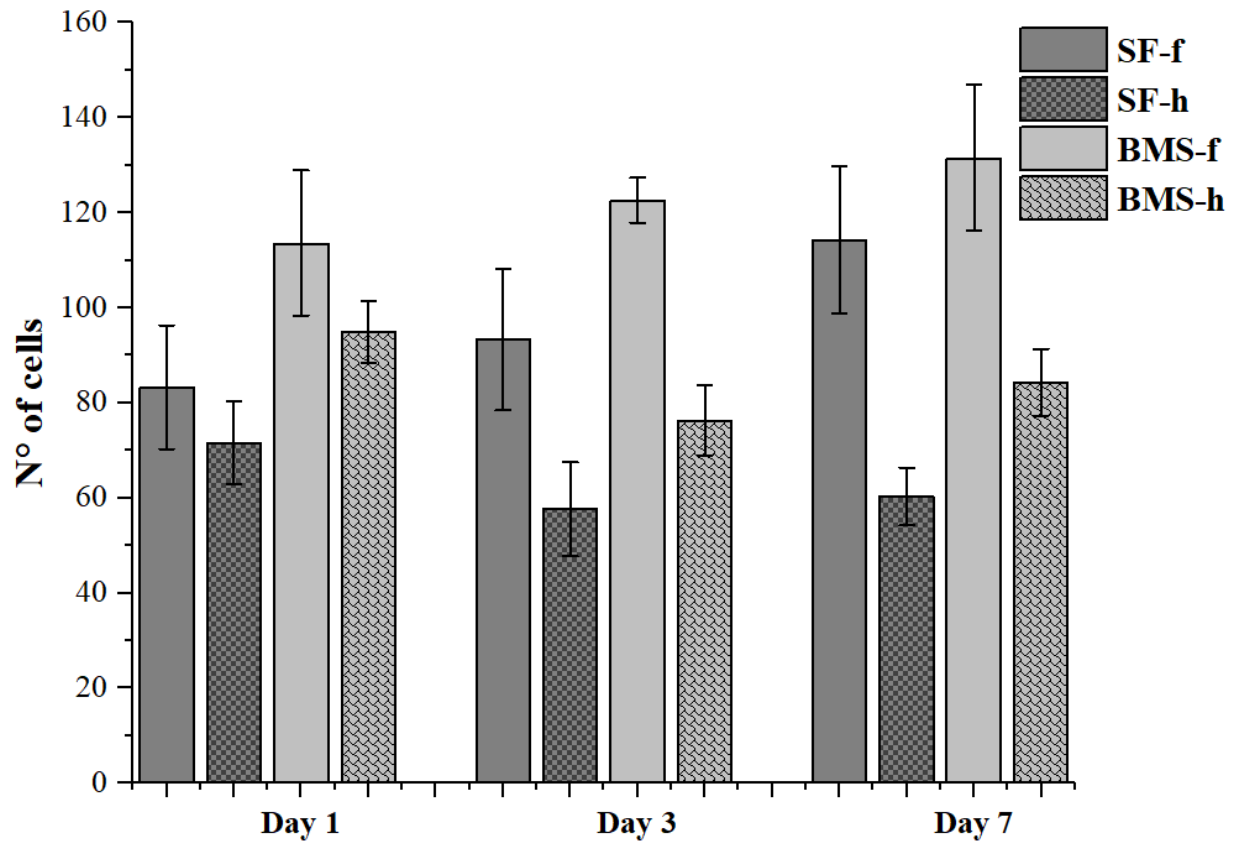
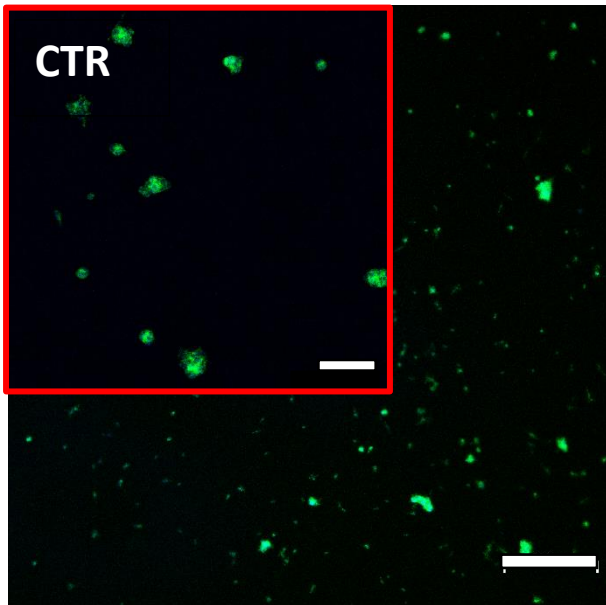
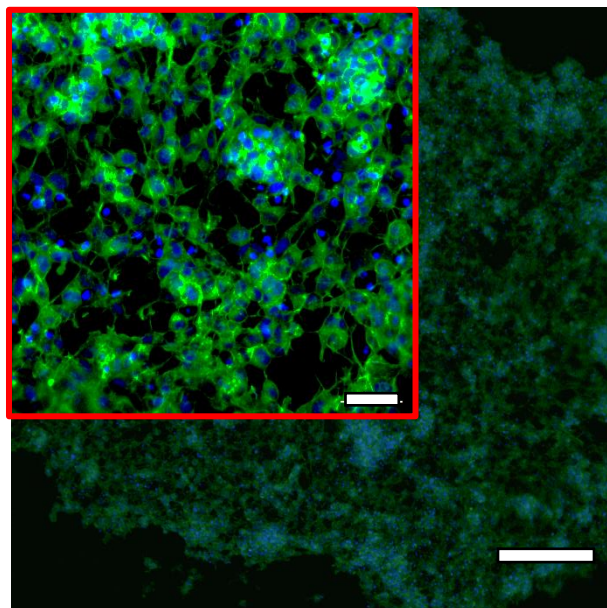
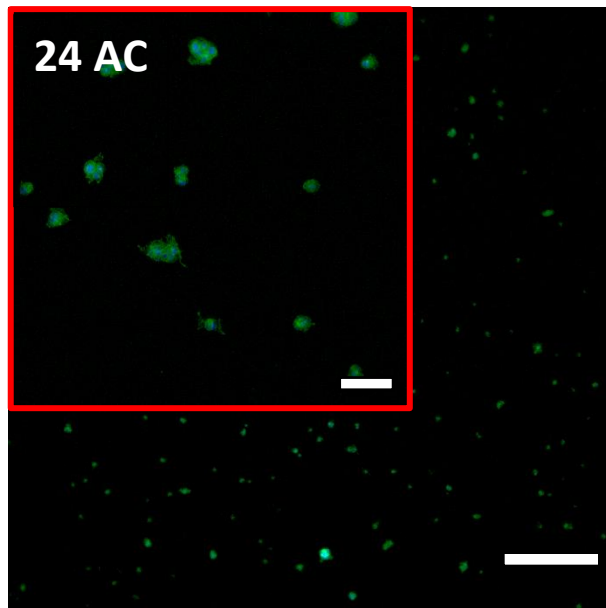
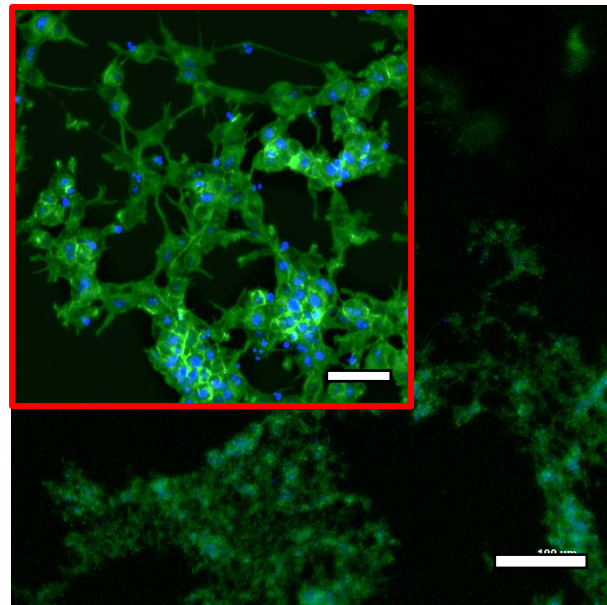


Figure S. 4. Evaluation of cells number analysing the confocal images of modified (BMS) and unmodified fibroin (SF) films (f) and hydrogels (h) at day 1-3-7. The differences among the cell number of the same sample typology are negligible.

DAY 1



DAY 7



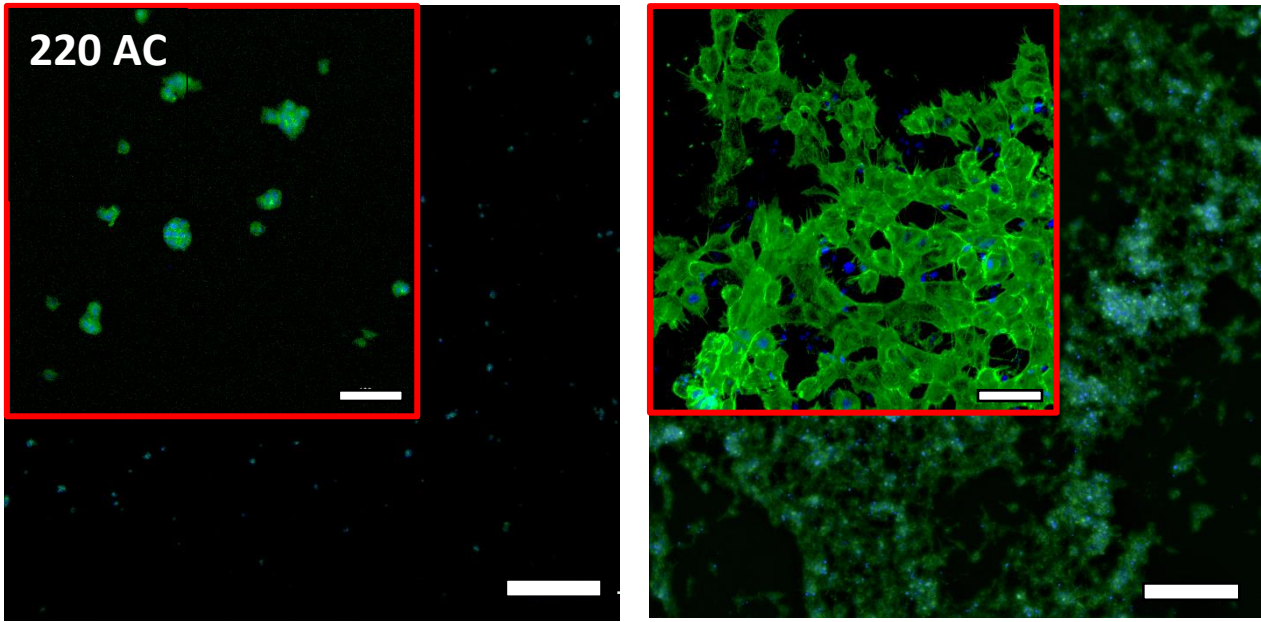


Figure S. 5. Cells adhesion of SH-5YSY after 7 days on SF hydrogels treated (24AC or 220 DC) or untreated. Scale bar 50 μm inside the red box and 500 μm for the low magnification.

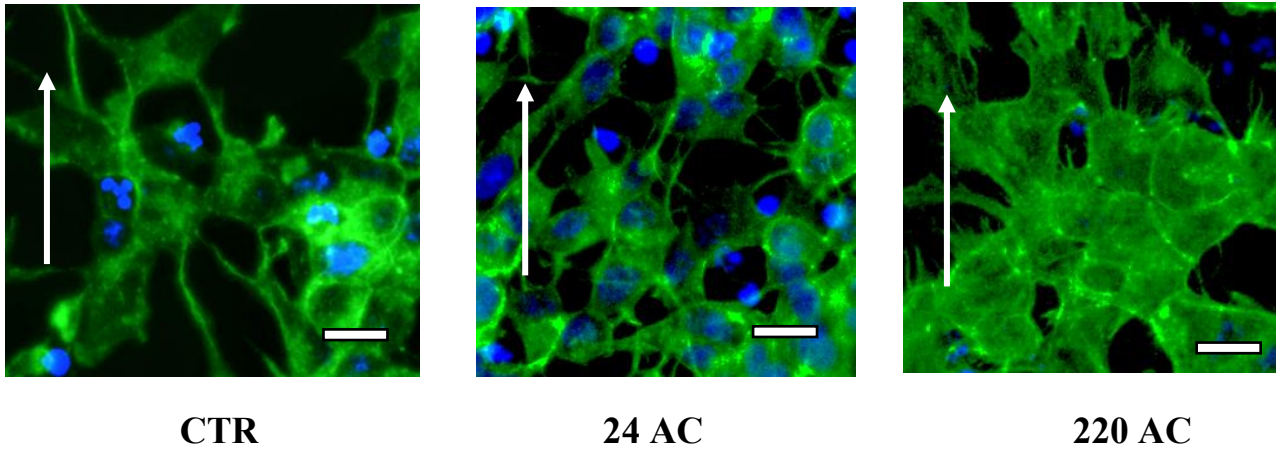


Figure S. 6. Magnification of the SH-5YSY after 7 days. Scale bar 20 μ m. Electric field lines direction (white arrow).

Table S. 2. Piezoelectricity values of treated and untreated SF at different concentrations. The values not reported regards samples that broke during the analysis.

Geometry A

	24 AC (V)	24 DC (V)	220AC (V)	220DC (V)	Control (V)
3% SF	2,7 ± 0,1	2,3 ± 0,2	3,4 ± 0,2	3,4 ± 0,4	1,6 ± 0,3
5% SF	3,3 ± 0,1	3,7 ± 0,2	4,8 ± 0,9	1,7 ± 0,3	3,3 ± 0,7
7% SF	6,5 ± 0,3	4,1 ± 0,3	3,5 ± 0,1	2,4 ± 0,3	/
9% SF	0,5 ± 0,1	0,8 ± 0,1	0,7 ± 0,2	0,6 ± 0,1	/

Geometry B

	24 AC (V)	24 DC (V)	220AC (V)	220DC (V)	C (V)
3% SF	1,7 ± 0,1	1,4 ± 0,2	2 ± 0,2	1,6 ± 0,4	3 ± 0,9
5% SF	2,4 ± 0,8	2,4 ± 0,6	2,3 ± 0,2	3 ± 0,7	2 ± 0,1
7% SF	1,1 ± 0,1	0,9 ± 0,1	1,5 ± 0,1	1 ± 0,1	3,7 ± 0,6
9% SF	/	/	/	0,8 ± 0,1	3 ± 0,1

Bibliography

- (1) Stifani, N. Motor Neurons and the Generation of Spinal Motor Neuron Diversity. *Front. Cell. Neurosci.* **2014**, *8* (OCT), 1–22. <https://doi.org/10.3389/fncel.2014.00293>.
- (2) Arrieta-Cruz, I.; Luna-López, A. *Geroscience*; 2018. https://doi.org/10.1007/978-3-319-95387-8_4.
- (3) Accogli, A.; Addour-Boudrahem, N.; Srour, M. *Neurogenesis, Neuronal Migration, and Axon Guidance*, 1st ed.; Elsevier B.V., 2020; Vol. 173. <https://doi.org/10.1016/B978-0-444-64150-2.00004-6>.
- (4) Yuskaitis, C. J.; Pomeroy, S. L. *131 - Development of the Nervous System*, Fifth Edit.; Elsevier Inc. <https://doi.org/10.1016/B978-0-323-35214-7.00131-1>.
- (5) Falk, J.; Castellani, V. Axon Guidance. **2013**, *2*, 69–88. <https://doi.org/10.1016/B978-0-12-397266-8.00012-0>.
- (6) Duband, J. L.; Thiery, J. P. Distribution of Laminin and Collagens during Avian Neural Crest Development. *Development* **1987**, *101* (3), 461–478.
- (7) Manuscript, A. NIH Public Access. **2013**, 77–92. <https://doi.org/10.1016/B978-0-444-53884-0.00019-1>.Postnatal.
- (8) Rothwell, J. Ascending and Descending Pathways of the Spinal Cord. **1994**.
- (9) Abbott, N. J. Inflammatory Mediators and Modulation of Blood-Brain Barrier Permeability. *Cell. Mol. Neurobiol.* **2000**, *20* (2), 131–147. <https://doi.org/10.1023/A:1007074420772>.
- (10) Adeeb, N.; Mortazavi, M. M.; Deep, A.; Griessenauer, C. J.; Watanabe, K.; Shoja, M. M.; Loukas, M.; Tubbs, R. S. The Pia Mater: A Comprehensive Review of Literature. *Child's Nerv. Syst.* **2013**, *29* (10), 1803–1810. <https://doi.org/10.1007/s00381-013-2044-5>.

- (11) Haines, D. E.; Mihailoff, G. A.; Yeziarski, R. P. *The Spinal Cord*, Fifth Edit.; Elsevier Inc., 2018. <https://doi.org/10.1016/B978-0-323-39632-5.00009-8>.
- (12) Jain, N. B.; Ayers, G. D.; Peterson, E. N.; Harris, M. B.; Morse, L.; O'Connor, K. C.; Garshick, E. Traumatic Spinal Cord Injury in the United States, 1993-2012. *J. Am. Med. Assoc.* **2015**, *313* (22), 2236–2243. <https://doi.org/10.1001/jama.2015.6250>.
- (13) Huang, H.; Young, W.; Skaper, S.; Chen, L.; Moviglia, G.; Saberi, H.; Al-Zoubi, Z.; Sharma, H. S.; Muresanu, D.; Sharma, A.; et al. Clinical Neurorestorative Therapeutic Guidelines for Spinal Cord Injury (IANR/CANR Version 2019). *J. Orthop. Transl.* **2020**, *20* (November 2019), 14–24. <https://doi.org/10.1016/j.jot.2019.10.006>.
- (14) Bonnet, M.; Alluin, O.; Trimaille, T.; Gignes, D.; Marqueste, T.; Decherchi, P. Delayed Injection of a Physically Cross-Linked PNIPAAm-g-PEG Hydrogel in Rat Contused Spinal Cord Improves Functional Recovery. *ACS Omega* **2020**, *5* (18), 10247–10259. <https://doi.org/10.1021/acsomega.9b03611>.
- (15) Kopp, M. A.; Liebscher, T.; Watzlawick, R.; Martus, P.; Laufer, S.; Blex, C.; Schindler, R.; Jungehulsing, G. J.; Knüppel, S.; Kreuzträger, M.; et al. SCISSOR - Spinal Cord Injury Study on Small Molecule-Derived Rho Inhibition: A Clinical Study Protocol. *BMJ Open* **2016**, *6* (7), 1–16. <https://doi.org/10.1136/bmjopen-2015-010651>.
- (16) *Biomaterials for Health: A Strategic Roadmap for Research and Innovation*.
- (17) James, N. D.; McMahon, S. B.; Field-Fote, E. C.; Bradbury, E. J. Neuromodulation in the Restoration of Function after Spinal Cord Injury. *Lancet Neurol.* **2018**, *17* (10), 905–917. [https://doi.org/10.1016/S1474-4422\(18\)30287-4](https://doi.org/10.1016/S1474-4422(18)30287-4).
- (18) Brimble, M. A.; Levi, M. S. A Review of Neuroprotective Agents. *Front. Med. Chem. - (Volume 3)* **2012**, 163–194. <https://doi.org/10.2174/978160805206610603010163>.

- (19) Borisoff, J. F.; Chan, C. C. M.; Hiebert, G. W.; Oschipok, L.; Robertson, G. S.; Zamboni, R.; Steeves, J. D.; Tetzlaff, W. Suppression of Rho-Kinase Activity Promotes Axonal Growth on Inhibitory CNS Substrates. *Mol. Cell. Neurosci.* **2003**, *22* (3), 405–416.
[https://doi.org/10.1016/S1044-7431\(02\)00032-5](https://doi.org/10.1016/S1044-7431(02)00032-5).
- (20) Wilcox, J. T.; Cadotte, D.; Fehlings, M. G. Spinal Cord Clinical Trials and the Role for Bioengineering. *Neurosci. Lett.* **2012**, *519* (2), 93–102.
<https://doi.org/10.1016/j.neulet.2012.02.028>.
- (21) Tetzlaff, W.; Okon, E. B.; Karimi-abdolrezaee, S.; Hill, C. E.; Sparling, J. S.; Plemel, J. R.; Plunet, W. T.; Tsai, E. C.; Baptiste, D.; Smithson, L. J.; et al. A Systematic Review of Cellular Transplantation Therapies for Spinal Cord Injury. *J. Neurotrauma* **2011**, *28* (8), 1611–1682.
<https://doi.org/https://doi.org/10.1089/neu.2009.1177>.
- (22) Wright, K. T.; El Masri, W.; Osman, A.; Chowdhury, J.; Johnson, W. E. B. Concise Review: Bone Marrow for the Treatment of Spinal Cord Injury: Mechanisms and Clinical Applications. *Stem Cells* **2011**, *29* (2), 169–178. <https://doi.org/10.1002/stem.570>.
- (23) Tsintou, M.; Dalamagkas, K.; Seifalian, A. M. Advances in Regenerative Therapies for Spinal Cord Injury: A Biomaterials Approach. *Neural Regen. Res.* **2015**, *10* (5), 726–742.
<https://doi.org/10.4103/1673-5374.156966>.
- (24) Cornelison, R. C.; Gonzalez-rothi, E. J.; Porvasnik, S. L.; Wellman, S. M.; Park, J. H.; Fuller, D. D.; Schmidt, C. E. Injectable Hydrogels of Optimized Acellular Nerve for Injection in the Injured Spinal Cord. *Biomed. Mater.* **2018**, *13* (3), 1–14.
<https://doi.org/https://doi.org/10.1088/1748-605X/aaab82>.
- (25) Higuchi, A.; Suresh Kumar, S.; Benelli, G.; Ling, Q. D.; Li, H. F.; Alarfaj, A. A.; Munusamy, M. A.; Sung, T. C.; Chang, Y.; Murugan, K. Biomaterials Used in Stem Cell Therapy for Spinal Cord Injury. *Prog. Mater. Sci.* **2019**, *103* (32), 374–424.
<https://doi.org/10.1016/j.pmatsci.2019.02.002>.

- (26) Führmann, T.; Anandakumaran, P. N.; Shoichet, M. S. Combinatorial Therapies After Spinal Cord Injury: How Can Biomaterials Help? *Advanced Healthcare Materials*. 2017, p 1601130. <https://doi.org/10.1002/adhm.201601130>.
- (27) Tuladhar, A.; Obermeyer, J. M.; Payne, S. L.; Siu, R. C. W.; Zand, S.; Morshead, C. M.; Shoichet, M. S. Injectable Hydrogel Enables Local and Sustained Co-Delivery to the Brain: Two Clinically Approved Biomolecules, Cyclosporine and Erythropoietin, Accelerate Functional Recovery in Rat Model of Stroke. *Biomaterials* **2020**, *235*, 119794. <https://doi.org/10.1016/j.biomaterials.2020.119794>.
- (28) Macaya, D.; Spector, M. Injectable Hydrogel Materials for Spinal Cord Regeneration: A Review. *Biomed. Mater.* **2012**, *7* (1), 012001. <https://doi.org/10.1088/1748-6041/7/1/012001>.
- (29) Khaing, Z. Z.; Ehsanipour, A.; Hofstetter, C. P.; Seidlits, S. K. Injectable Hydrogels for Spinal Cord Repair: A Focus on Swelling and Intraspinal Pressure. *Cells, Tissues, Organs*. S. Karger AG October 1, 2016, pp 67–84. <https://doi.org/10.1159/000446697>.
- (30) Okada, S. The Pathophysiological Role of Acute Inflammation after Spinal Cord Injury. *Inflamm. Regen.* **2016**, *36* (1), 20. <https://doi.org/10.1186/s41232-016-0026-1>.
- (31) Orr, M. B.; Gensel, J. C. Spinal Cord Injury Scarring and Inflammation: Therapies Targeting Glial and Inflammatory Responses. *Neurotherapeutics* **2018**, *15* (3), 541–553. <https://doi.org/10.1007/s13311-018-0631-6>.
- (32) Lee, H.; McKeon, R. J.; Bellamkonda, R. V. Sustained Delivery of Thermostabilized ChABC Enhances Axonal Sprouting and Functional Recovery after Spinal Cord Injury. *Proc. Natl. Acad. Sci.* **2010**, *107* (8), 3340–3345. <https://doi.org/10.1073/pnas.0905437106>.
- (33) Tran, A. P.; Warren, P. M.; Silver, J. The Biology of Regeneration Failure and Success after Spinal Cord Injury. *Physiol. Rev.* **2018**, *98* (2), 881–917. <https://doi.org/10.1152/physrev.00017.2017>.

- (34) Azizi, M.; Farahmandghavi, F.; Joghataei, M. T.; Zandi, M.; Imani, M.; Bakhtiari, M.; Omidian, H. ChABC-Loaded PLGA Nanoparticles: A Comprehensive Study on Biocompatibility, Functional Recovery, and Axonal Regeneration in Animal Model of Spinal Cord Injury. *Int. J. Pharm.* **2020**, *577*, 119037. <https://doi.org/10.1016/j.ijpharm.2020.119037>.
- (35) Shechter, R.; Miller, O.; Yovel, G.; Rosenzweig, N.; London, A.; Ruckh, J.; Kim, K. W.; Klein, E.; Kalchenko, V.; Bendel, P.; et al. Recruitment of Beneficial M2 Macrophages to Injured Spinal Cord Is Orchestrated by Remote Brain Choroid Plexus. *Immunity* **2013**, *38* (3), 555–569. <https://doi.org/10.1016/j.immuni.2013.02.012>.
- (36) Solár, P.; Zamani, A.; Kubíčková, L.; Dubový, P.; Joukal, M. Choroid Plexus and the Blood-Cerebrospinal Fluid Barrier in Disease. *Fluids Barriers CNS* **2020**, *17*, 1–29. <https://doi.org/10.1186/s12987-020-00196-2>.
- (37) Ransohoff, R. M.; Kivisäkk, P.; Kidd, G. Three or More Routes for Leukocyte Migration into the Central Nervous System. *Nat. Rev. Immunol.* **2003**, *3* (7), 569–581. <https://doi.org/10.1038/nri1130>.
- (38) Arnold, L.; Henry, A.; Poron, F.; Baba-Amer, Y.; Van Rooijen, N.; Plonquet, A.; Gherardi, R. K.; Chazaud, B. Inflammatory Monocytes Recruited after Skeletal Muscle Injury Switch into Antiinflammatory Macrophages to Support Myogenesis. *J. Exp. Med.* **2007**, *204* (5), 1057–1069. <https://doi.org/10.1084/jem.20070075>.
- (39) Filli, L.; Engmann, A. K.; Zörner, B.; Weinmann, O.; Moraitis, T.; Gullo, M.; Kasper, H.; Schneider, R.; Schwab, M. E. Bridging the Gap: A Reticulo-Propriospinal Detour Bypassing an Incomplete Spinal Cord Injury. *J. Neurosci.* **2014**, *34* (40), 13399–13410. <https://doi.org/10.1523/JNEUROSCI.0701-14.2014>.
- (40) Beattie, M. S.; Bresnahan, J. C.; Komon, ‡ J; Tovar, C. A.; Van Meter, M.; Anderson, D. K.; Faden, A. I.; Hsu, C. Y.; Noble, L. J.; Salzman, S.; et al. Endogenous Repair after Spinal Cord Contusion Injuries in the Rat. *Exp. Neurol.* **1997**, *148* (2), 453–463.

<https://doi.org/10.1006/exnr.1997.6695>.

- (41) Wang, Q.; He, Y.; Zhao, Y.; Xie, H.; Lin, Q.; He, Z.; Wang, X.; Li, J.; Zhang, H.; Wang, C.; et al. A Thermosensitive Heparin-Poloxamer Hydrogel Bridges AFGF to Treat Spinal Cord Injury. *ACS Appl. Mater. Interfaces* **2017**, *9* (8), 6725–6745.
<https://doi.org/10.1021/acsami.6b13155>.
- (42) Hu, H. Z.; Granger, N.; Balakrishna Pai, S.; Bellamkonda, R. V.; Jeffery, N. D. Therapeutic Efficacy of Microtube-Embedded Chondroitinase ABC in a Canine Clinical Model of Spinal Cord Injury. *Brain* **2018**, *141* (4), 1017–1027. <https://doi.org/10.1093/brain/awy007>.
- (43) Hassannejad, Z.; Zadegan, A. S.; Vaccaro, A. R.; Rahimi-Movaghar, V.; Sabzevari, O. Biofunctionalized Peptide-Based Hydrogel as an Injectable Scaffold for BDNF Delivery Can Improve Regeneration after Spinal Cord Injury. *Injury* **2019**, *50* (2), 278–285.
<https://doi.org/10.1016/j.injury.2018.12.027>.
- (44) Cigognini, D.; Silva, D.; Paloppi, S.; Gelain, F. Evaluation of Mechanical Properties and Therapeutic Effect of Injectable Self-Assembling Hydrogels for Spinal Cord Injury. *J. Biomed. Nanotechnol.* **2014**, *10* (2), 309–323. <https://doi.org/10.1166/jbn.2014.1759>.
- (45) Tysseling, V. M.; Sahni, V.; Pashuck, E. T.; Birch, D.; Hebert, A.; Czeisler, C.; Stupp, S. I.; Kessler, J. A. Self-Assembling Peptide Amphiphile Promotes Plasticity of Serotonergic Fibers Following Spinal Cord Injury. *J. Neurosci. Res.* **2010**, *88* (14), 3161–3170.
<https://doi.org/10.1002/jnr.22472>.
- (46) Sever-Bahcekapili, M.; Yilmaz, C.; Demirel, A.; Kilinc, M. C.; Dogan, I.; Caglar, Y. S.; Guler, M. O.; Tekinay, A. B. Neuroactive Peptide Nanofibers for Regeneration of Spinal Cord after Injury. *Macromol. Biosci.* **2020**, 1–9. <https://doi.org/10.1002/mabi.202000234>.
- (47) Macaya, D.; Spector, M. Injectable Hydrogel Materials for Spinal Cord Regeneration: A Review. *Biomed. Mater.* **2012**, *7* (1).
<https://doi.org/10.1088/1748-6041/7/1/012001>.

- (48) Neurofibres <https://cordis.europa.eu/project/id/732344>.
- (49) Joo, M. C.; Jang, C. H.; Park, J. T.; Choi, S. W.; Ro, S.; Kim, M. S.; Lee, M. Y. Effect of Electrical Stimulation on Neural Regeneration via the P38-RhoA and ERK1/2-Bcl-2 Pathways in Spinal Cord-Injured Rats. *Neural Regen. Res.* **2018**, *13* (2), 340. <https://doi.org/10.4103/1673-5374.226404>.
- (50) Vara, H.; Collazos-Castro, J. E. Enhanced Spinal Cord Microstimulation Using Conducting Polymer-Coated Carbon Microfibers. *Acta Biomater.* **2019**, *90*, 71–86. <https://doi.org/10.1016/j.actbio.2019.03.037>.
- (51) Lee, K. H.; Chung, K.; Chung, J. M.; Coggeshall, R. E. Correlation of Cell Body Size, Axon Size, and Signal Conduction Velocity for Individually Labelled Dorsal Root Ganglion Cells in the Cat. *J. Comp. Neurol.* **1986**, *243* (3), 335–346. <https://doi.org/10.1002/cne.902430305>.
- (52) Vara, H.; Collazos-Castro, J. E. Biofunctionalized Conducting Polymer/Carbon Microfiber Electrodes for Ultrasensitive Neural Recordings. *ACS Appl. Mater. Interfaces* **2015**, *7* (48), 27016–27026. <https://doi.org/10.1021/acsami.5b09594>.
- (53) Zhuang, P.; Sun, A. X.; An, J.; Chua, C. K.; Chew, S. Y. 3D Neural Tissue Models: From Spheroids to Bioprinting. *Biomaterials* **2018**, *154*, 113–133. <https://doi.org/10.1016/j.biomaterials.2017.10.002>.
- (54) Führmann, T.; Tam, R. Y.; Ballarin, B.; Coles, B.; Elliott Donaghue, I.; van der Kooy, D.; Nagy, A.; Tator, C. H.; Morshead, C. M.; Shoichet, M. S. Injectable Hydrogel Promotes Early Survival of Induced Pluripotent Stem Cell-Derived Oligodendrocytes and Attenuates Longterm Teratoma Formation in a Spinal Cord Injury Model. *Biomaterials* **2016**, *83*, 23–36. <https://doi.org/10.1016/j.biomaterials.2015.12.032>.
- (55) Vismara, I.; Papa, S.; Veneruso, V.; Mauri, E.; Mariani, A.; Paola, M. De; Roberta, A.; Rossetti, A.; Sponchioni, M.; Moscatelli, D.; et al. Selective Modulation of A1 Astrocytes by Drug-Loaded Nano-Structured Gel in Spinal Cord Injury. *ACS Nano* **2020**, *14* (1), 360–371.

<https://doi.org/10.1021/acsnano.9b05579>.

- (56) Wang, C.; Gong, Z.; Huang, X.; Wang, J.; Xia, K.; Ying, L.; Shu, J.; Yu, C.; Zhou, X.; Li, F.; et al. An Injectable Heparin-Laponite Hydrogel Bridge FGF4 for Spinal Cord Injury by Stabilizing Microtubule and Improving Mitochondrial Function. *Theranostics* **2019**, *9* (23), 7016–7032. <https://doi.org/10.7150/thno.37601>.
- (57) Hong, L. T. A.; Kim, Y. M.; Park, H. H.; Hwang, D. H.; Cui, Y.; Lee, E. M.; Yahn, S.; Lee, J. K.; Song, S. C.; Kim, B. G. An Injectable Hydrogel Enhances Tissue Repair after Spinal Cord Injury by Promoting Extracellular Matrix Remodeling. *Nat. Commun.* **2017**, *8* (1), 1–14. <https://doi.org/10.1038/s41467-017-00583-8>.
- (58) Boido, M.; Ghibaudi, M.; Gentile, P.; Favaro, E.; Fusaro, R.; Tondaturo, C. Chitosan-Based Hydrogel to Support the Paracrine Activity of Mesenchymal Stem Cells in Spinal Cord Injury Treatment. *Sci. Rep.* **2019**, *9* (1), 1–16. <https://doi.org/10.1038/s41598-019-42848-w>.
- (59) Li, X. L.; Wu, M.; Gu, L.; Ren, Y. T.; Mu, M.; Wang, Y. L.; Gao, X.; Li, J. L.; Tong, A. P.; Zhu, H. Y.; et al. A Single Dose of Thermal-Sensitive Biodegradable Hybrid Hydrogel Promotes Functional Recovery after Spinal Cord Injury. *Appl. Mater. Today* **2019**, *14*, 66–75. <https://doi.org/10.1016/j.apmt.2018.10.007>.
- (60) Elliott Donaghue, I.; Tator, C. H.; Shoichet, M. S. Sustained Delivery of Bioactive Neurotrophin-3 to the Injured Spinal Cord. *Biomater. Sci.* **2015**, *3* (1), 65–72. <https://doi.org/10.1039/c4bm00311j>.
- (61) Kang, C. E.; Baumann, M. D.; Tator, C. H.; Shoichet, M. S. Localized and Sustained Delivery of Fibroblast Growth Factor-2 from a Nanoparticle-Hydrogel Composite for Treatment of Spinal Cord Injury. *Cells Tissues Organs* **2012**, *197* (1), 55–63. <https://doi.org/10.1159/000339589>.
- (62) Ansorena, E.; De Berdt, P.; Ucakar, B.; Simón-Yarza, T.; Jacobs, D.; Schakman, O.; Jankovski, A.; Deumens, R.; Blanco-Prieto, M. J.; Pr at, V.; et al. Injectable Alginate Hydrogel Loaded with GDNF Promotes

Functional Recovery in a Hemisection Model of Spinal Cord Injury. *Int. J. Pharm.* **2013**, *455* (1–2), 148–158.
<https://doi.org/10.1016/j.ijpharm.2013.07.045>.

- (63) Jain, A.; McKeon, R. J.; Brady-Kalnay, S. M.; Bellamkonda, R. V. Sustained Delivery of Activated Rho GTPases and BDNF Promotes Axon Growth in CSPG-Rich Regions Following Spinal Cord Injury. *PLoS One* **2011**, *6* (1), e16135.
<https://doi.org/10.1371/journal.pone.0016135>.
- (64) Chen, S.; Liu, S.; Zhang, L.; Han, Q.; Liu, H.; Shen, J.; Lia, G.; Zhanga, L.; Yang, Y. Construction of Injectable Silk Fibroin/Polydopamine Hydrogel for Treatment of Spinal Cord Injury. *Chem. Eng. J.* **2020**, *399*, 125795. <https://doi.org/10.1016/j.cej.2020.125795>.
- (65) Li, X.; Zhang, C.; Haggerty, A. E.; Yan, J.; Lan, M.; Seu, M.; Yang, M.; Marlow, M. M.; Maldonado-Iasunción, I.; Cho, B.; et al. The Effect of a Nanofiber-Hydrogel Composite on Neural Tissue Repair and Regeneration in the Contused Spinal Cord. *Biomaterials* **2020**, *245* (March), 119978. <https://doi.org/10.1016/j.biomaterials.2020.119978>.
- (66) Wang, C.; Yue, H.; Feng, Q.; Xu, B.; Bian, L.; Shi, P. Injectable Nanoreinforced Shape-Memory Hydrogel System for Regenerating Spinal Cord Tissue from Traumatic Injury. *ACS Appl. Mater. Interfaces* **2018**, *10* (35), 29299–29307. <https://doi.org/10.1021/acsami.8b08929>.
- (67) Khaing, Z. Z.; Agrawal, N. K.; Park, J. H.; Xin, S.; Plumton, G. C.; Lee, K. H.; Huang, Y.; Niemerski, A. L.; Schmidt, C. E.; Grau, J. W. Localized and Sustained Release of Brain-Derived Neurotrophic Factor from Injectable Hydrogel/Microparticle Composites Fosters Spinal Learning after Spinal Cord Injury. *J. Mater. Chem. B* **2016**, *4* (47), 7560–7571. <https://doi.org/10.1039/C6TB01602B>.
- (68) Nazemi, Z.; Nourbakhsh, M. S.; Kiani, S.; Heydari, Y.; Ashtianie, M. K.; Hamed, D.; Baharvand, H. Co-Delivery of Minocycline and Paclitaxel from Injectable Hydrogel for Treatment of Spinal Cord Injury. *J. Control. Release* **2020**, *321*, 145–158.
<https://doi.org/10.1016/j.jconrel.2020.02.009>.

- (69) Marquardt, L. M.; Doulames, V. M.; Wang, A. T.; Dubbin, K.; Suhar, R. A.; Kratochvil, M. J.; Medress, Z. A.; Plant, G. W.; Heilshorn, S. C. Designer , Injectable Gels to Prevent Transplanted Schwann Cell Loss during Spinal Cord Injury Therapy. *Sci. Adv.* **2020**, *6* (14), eaaz1039. <https://doi.org/10.1126/sciadv.aaz1039>.
- (70) Tavakol, S.; Saber, R.; Hoveizi, E.; Tavakol, B.; Aligholi, H.; Ai, J.; Rezayat, S. M. Self-Assembling Peptide Nanofiber Containing Long Motif of Laminin Induces Neural Differentiation, Tubulin Polymerization, and Neurogenesis: In Vitro, Ex Vivo, and In Vivo Studies. *Mol. Neurobiol.* **2016**, *53* (8), 5288–5299. <https://doi.org/10.1007/s12035-015-9448-z>.
- (71) Zweckberger, K.; Liu, Y.; Wang, J.; Forgione, N.; Fehlings, M. G. Synergetic Use of Neural Precursor Cells and Self-Assembling Peptides in Experimental Cervical Spinal Cord Injury. *J. Vis. Exp.* **2015**, *96*, e52105. <https://doi.org/10.3791/52105>.
- (72) Ye, J.; Qin, Y.; Wu, Y.; Wang, P.; Tang, Y.; Huang, L.; Ma, M.; Zeng, Y.; Shen, H. Using Primate Neural Stem Cells Cultured in Self-Assembling Peptide Nanofiber Scaffolds to Repair Injured Spinal Cords in Rats. *Spinal Cord* **2016**, *54*, 933–941. <https://doi.org/10.1038/sc.2016.36>.
- (73) Tran, K. A.; Partyka, P. P.; Jin, Y.; Bouyer, J.; Fischer, I.; Galie, P. A. Vascularization of Self-Assembled Peptide Scaffolds for Spinal Cord Injury Repair. *Acta Biomater.* **2020**, *104*, 76–84. <https://doi.org/10.1016/j.actbio.2019.12.033>.
- (74) Cigognini, D.; Satta, A.; Colleoni, B.; Silva, D.; Donega, M. Evaluation of Early and Late Effects into the Acute Spinal Cord Injury of an Injectable Functionalized Self- Assembling Scaffold. *PLoS One* **2011**, *6* (5), e19782. <https://doi.org/10.1371/journal.pone.0019782>.
- (75) Sun, Y.; Li, W.; Wu, X.; Zhang, N.; Zhang, Y.; Ouyang, S.; Song, X.; Fang, X.; Seeram, R.; Xue, W.; et al. Functional Self-Assembling Peptide Nano Fiber Hydrogels Designed for Nerve Degeneration. *ACS Appl. Mater. Interfaces* **2016**, *8* (3), 2348–2359.

<https://doi.org/10.1021/acsami.5b11473>.

- (76) Zhang, Y.; Li, L.; Mu, J.; Chen, J.; Feng, S.; Gao, J. Implantation of a Functional TEMPO-Hydrogel Induces Recovery from Rat Spinal Cord Transection through Promoting Nerve Regeneration and Protecting Bladder Tissue. *Biomater. Sci.* **2020**, *8* (6), 1695–1701. <https://doi.org/10.1039/c9bm01530b>.
- (77) Gupta, D.; Tator, C. H.; Shoichet, M. S. Fast-Gelling Injectable Blend of Hyaluronan and Methylcellulose for Intrathecal, Localized Delivery to the Injured Spinal Cord. *Biomaterials* **2006**, *27* (11), 2370–2379. <https://doi.org/10.1016/j.biomaterials.2005.11.015>.
- (78) Lee, B. H.; Lee, Y. M.; Sohn, Y. S.; Song, S. C. A Thermosensitive Poly(Organophosphazene) Gel. *Macromolecules* **2002**, *35* (10), 3876–3879. <https://doi.org/10.1021/ma012093q>.
- (79) Liang, Y.; Zhao, X.; Hu, T.; Han, Y.; Guo, B. Mussel-Inspired, Antibacterial, Conductive, Antioxidant, Injectable Composite Hydrogel Wound Dressing to Promote the Regeneration of Infected Skin. *J. Colloid Interface Sci.* **2019**, *556*, 514–528. <https://doi.org/10.1016/j.jcis.2019.08.083>.
- (80) Van Vlierberghe, S.; Dubruel, P.; Schacht, E. Biopolymer-Based Hydrogels as Scaffolds for Tissue Engineering Applications: A Review. *Biomacromolecules* **2011**, *12* (5), 1387–1408. <https://doi.org/10.1021/bm200083n>.
- (81) Klouda, L. Thermoresponsive Hydrogels in Biomedical Applications A Seven-Year Update. *Eur. J. Pharm. Biopharm.* **2015**, *97*, 338–349. <https://doi.org/10.1016/j.ejpb.2015.05.017>.
- (82) Comolli, N.; Neuhuber, B.; Fischer, I.; Lowman, A. In Vitro Analysis of PNIPAAm-PEG, a Novel, Injectable Scaffold for Spinal Cord Repair. *Acta Biomater.* **2009**, *5* (4), 1046–1055. <https://doi.org/10.1016/j.actbio.2008.10.008>.
- (83) Cai, L.; Dewi, R. E.; Heilshorn, S. C. Injectable Hydrogels with in Situ Double Network Formation Enhance Retention of Transplanted Stem

Cells. *Adv. Funct. Mater.* **2015**, *25* (9), 1344–1351.
<https://doi.org/10.1002/adfm.201403631>.

- (84) Zhang, C.; Morozova, A.; Baklaushev, V.; Gubsky, I.; Pa, M.; Gabashvily, A.; Guowen, W.; Lili, L.; Haixiao, W.; Xin, W.; et al. Nanoparticles Guided Precise Transplantation of Varying Numbers of Mesenchymal Stem Cells into Post-Traumatic Syring in Spinal Cord Injury Rat. *Bull. Russ. State Med. Univ.* **2018**, *6*, 49–56.
<https://doi.org/10.24075/brsmu.2018.084>.
- (85) Li, X.; Cho, B.; Martin, R.; Seu, M.; Zhang, C.; Zhou, Z.; Choi, J. S.; Jiang, X.; Chen, L.; Walia, G.; et al. Nanofiber-Hydrogel Composite–Mediated Angiogenesis for Soft Tissue Reconstruction. *Sci. Transl. Med.* **2019**, *11* (490), 1–12.
<https://doi.org/10.1126/scitranslmed.aau6210>.
- (86) Silva, G. A.; Czeisler, C.; Niece, K. L.; Beniash, E.; Harrington, D. A.; Kessler, J. A.; Stupp, S. I. Selective Differentiation of Neural Progenitor Cells by High-Epitope Density Nanofibers. *Science* (80-.). **2004**, *303* (5662), 1352–1355. <https://doi.org/10.1126/science.1093783>.
- (87) Tysseling-Mattiace, V. M.; Sahni, V.; Niece, K. L.; Birch, D.; Czeisler, C.; Fehlings, M. G.; Stupp, S. I.; Kessler, J. A. Self-Assembling Nanofibers Inhibit Glial Scar Formation and Promote Axon Elongation after Spinal Cord Injury. *J. Neurosci.* **2008**, *28* (14), 3814–3823.
<https://doi.org/10.1523/JNEUROSCI.0143-08.2008>.
- (88) Gelain, F.; Bottai, D.; Vescovi, A.; Zhang, S. Designer Self-Assembling Peptide Nanofiber Scaffolds for Adult Mouse Neural Stem Cell 3-Dimensional Cultures. *PLoS One* **2006**, *1* (1), e119.
<https://doi.org/10.1371/journal.pone.0000119>.
- (89) Zhang, Z. X.; Zheng, Q. X.; Wu, Y. C.; Hao, D. J. Compatibility of Neural Stem Cells with Functionalized Selfassembling Peptide Scaffold in Vitro. *Biotechnol. Bioprocess Eng.* **2010**, *15* (4), 545–551.
<https://doi.org/10.1007/s12257-009-3076-2>.
- (90) Cheriyan, T.; Ryan, D. J.; Weinreb, J. H.; Cheriyan, J.; Paul, J. C.;

Lafage, V.; Kirsch, T.; Errico, T. J. Spinal Cord Injury Models: A Review. *Spinal Cord* **2014**, *52* (8), 588–595.
<https://doi.org/10.1038/sc.2014.91>.

- (91) Krishna, V.; Andrews, H.; Jin, X.; Yu, J.; Varma, A.; Wen, X.; Kindy, M. A Contusion Model of Severe Spinal Cord Injury in Rats. *J. Vis. Exp.* **2013**, No. 78, e50111. <https://doi.org/10.3791/50111>.
- (92) Gruner, J. A. A Monitored Contusion Model of Spinal Cord Injury in the Rat. *J. Neurotrauma* **1992**, *9* (2), 123–128.
<https://doi.org/10.1089/neu.1992.9.123>.
- (93) Banik, N. L.; Powers, J. M.; Hogan, E. L. The Effects of Spinal Cord Trauma on Myelin. *J. Neuropathol. Exp. Neurol.* **1980**, *39* (3), 232–244.
<https://doi.org/doi.org/10.1097/00005072-198005000-00002>.
- (94) Blight, A. R.; Decrescito, V. Morphometric Analysis of Experimental Spinal Cord Injury in the Cat: The Relation of Injury Intensity to Survival of Myelinated Axons. *Neuroscience* **1986**, *19* (1), 321–341.
[https://doi.org/10.1016/0306-4522\(86\)90025-4](https://doi.org/10.1016/0306-4522(86)90025-4).
- (95) Young, W. Spinal Cord Contusion Models. In *Progress in Brain Research*; 2002; Vol. 137, pp 231–255. [https://doi.org/10.1016/S0079-6123\(02\)37019-5](https://doi.org/10.1016/S0079-6123(02)37019-5).
- (96) Qin, W.; Zhang, M.; Piao, Y.; Guo, D.; Zhu, Z.; Tian, X.; Li, K.; Yu, C. Wallerian Degeneration in Central Nervous System: Dynamic Associations between Diffusion Indices and Their Underlying Pathology. *PLoS One* **2012**, *7* (7), e41441.
<https://doi.org/10.1371/journal.pone.0041441>.
- (97) Paterniti, I.; Esposito, E.; Cuzzocrea, S. An in Vivo Compression Model of Spinal Cord Injury. In *Neurotrophic Factors*; Humana Press: New York, NY, 2018; pp 379–384. https://doi.org/10.1007/978-1-4939-7571-6_29.
- (98) Li, X.; Liu, D.; Xiao, Z.; Zhao, Y.; Han, S.; Chen, B.; Dai, J. Scaffold-Facilitated Locomotor Improvement Post Complete Spinal Cord Injury: Motor Axon Regeneration versus Endogenous Neuronal Relay

Formation. *Biomaterials* **2019**, *197*, 20–31.
<https://doi.org/10.1016/j.biomaterials.2019.01.012>.

- (99) Ahmed, R. U.; Alam, M.; Zheng, Y. P. Experimental Spinal Cord Injury and Behavioral Tests in Laboratory Rats. *Heliyon* **2019**, *5* (3), e01324.
<https://doi.org/10.1016/j.heliyon.2019.e01324>.
- (100) Slovinska, L.; Blasko, J.; Nagyova, M.; Szekiova, E.; Cizkova, D. In Vitro Models of Spinal Cord Injury. In *Recovery of Motor Function Following Spinal Cord Injury*; IntechOpen, Ed.; InTech, 2016.
<https://doi.org/10.5772/63459>.
- (101) Ganz, J.; Shor, E.; Guo, S.; Sheinin, A.; Arie, I.; Michaelievski, I.; Pitaru, S.; Offen, D.; Levenberg, S. Implantation of 3D Constructs Embedded with Oral Mucosa-Derived Cells Induces Functional Recovery in Rats with Complete Spinal Cord Transection. *Front. Neurosci.* **2017**, *11*, 589. <https://doi.org/10.3389/fnins.2017.00589>.
- (102) Fouad, K.; Hurd, C.; Magnuson, D. S. K. Functional Testing in Animal Models of Spinal Cord Injury: Not as Straight Forward as One Would Think. *Front. Integr. Neurosci.* **2013**, *7*, 85.
<https://doi.org/10.3389/fnint.2013.00085>.
- (103) Pandamooz, S.; Salehi, M. S.; Zibaii, M. I.; Safari, A.; Nabiuni, M.; Ahmadiani, A.; Dargahi, L. Modeling Traumatic Injury in Organotypic Spinal Cord Slice Culture Obtained from Adult Rat. *Tissue Cell* **2019**, *56*, 90–97. <https://doi.org/10.1016/j.tice.2019.01.002>.
- (104) Tadie, M.; Liu, S.; Robert, R.; Guiheneuc, P.; Pereon, Y.; Perrouin-Verbe, B.; Mathe, J. F. Partial Return of Motor Function in Paralyzed Legs after Surgical Bypass of the Lesion Site by Nerve Autografts Three Years after Spinal Cord Injury. *J. Neurotrauma* **2002**, *19* (8), 909–916. <https://doi.org/10.1089/089771502320317069>.
- (105) Ko, K. R.; Frampton, J. P. Developments in 3D Neural Cell Culture Models: The Future of Neurotherapeutics Testing? *Expert Rev. Neurother.* **2016**, *16* (7), 739–741.
<https://doi.org/10.1586/14737175.2016.1166053>.

- (106) Krassioukov, A. V.; Ackery, A.; Schwartz, G.; Adamchik, Y.; Liu, Y.; Fehlings, M. G. An in Vitro Model of Neurotrauma in Organotypic Spinal Cord Cultures from Adult Mice. *Brain Res. Protoc.* **2002**, *10* (2), 60–68. [https://doi.org/10.1016/S1385-299X\(02\)00180-0](https://doi.org/10.1016/S1385-299X(02)00180-0).
- (107) Donnelly, F. Regulatory Science Regulatory Science as a Means to Respond to EU Healthcare Challenges and Global Market Needs. *J. Regul. Sci.* **2016**, *4* (4), 21–28. <https://doi.org/https://doi.org/10.21423/jrs-v04n04p021>.
- (108) Chiu, C.-W.; Cheng, H.; Hsieh, S.-L. Contusion Spinal Cord Injury Rat Model. *Bio-Protocol* **2017**, *7* (12), 1–8. <https://doi.org/10.21769/bioprotoc.2337>.
- (109) Inoue, S.; Tanaka, K.; Arisaka, F.; Kimura, S.; Ohtomo, K.; Mizuno, S. Silk Fibroin of Bombyx Mori Is Secreted, Assembling a High Molecular Mass Elementary Unit Consisting of H-Chain, L-Chain, and P25, with a 6:6:1 Molar Ratio. *J. Biol. Chem.* **2000**, *275* (51), 40517–40528. <https://doi.org/10.1074/jbc.M006897200>.
- (110) Floren, M.; Migliaresi, C.; Motta, A. Processing Techniques and Applications of Silk Hydrogels in Bioengineering. *J. Funct. Biomater.* **2016**, *7* (3), 26. <https://doi.org/10.3390/jfb7030026>.
- (111) Servoli, E.; Maniglio, D.; Motta, A.; Predazzer, R.; Migliaresi, C. Surface Properties of Silk Fibroin Films and Their Interaction with Fibroblasts. *Macromol. Biosci.* **2005**, *5* (12), 1175–1183. <https://doi.org/10.1002/mabi.200500137>.
- (112) Sun, W.; Incitti, T.; Migliaresi, C.; Quattrone, A.; Casarosa, S.; Motta, A. Viability and Neuronal Differentiation of Neural Stem Cells Encapsulated in Silk Fibroin Hydrogel Functionalized with an IKVAV Peptide. *J. Tissue Eng. Regen. Med.* **2017**, *11* (5), 1532–1541. <https://doi.org/10.1002/term.2053>.
- (113) Partlow, B. P.; Tabatabai, A. P.; Leisk, G. G.; Cebe, P.; Blair, D. L.; Kaplan, D. L. Silk Fibroin Degradation Related to Rheological and Mechanical Properties. *Macromol. Biosci.* **2016**, *16* (5), 666–675.

<https://doi.org/10.1002/mabi.201500370>.

- (114) Sekiguchi, R.; Yamada, K. M. *Basement Membranes in Development and Disease*, 1st ed.; Elsevier Inc., 2018; Vol. 130. <https://doi.org/10.1016/bs.ctdb.2018.02.005>.
- (115) Cruz-Acuña, R.; García, A. J. Synthetic Hydrogels Mimicking Basement Membrane Matrices to Promote Cell-Matrix Interactions. *Matrix Biol.* **2017**, 57–58, 324–333. <https://doi.org/10.1016/j.matbio.2016.06.002>.
- (116) Lebleu, V. S.; Macdonald, B.; Kalluri, R. Experimental Biology and Medicine Structure and Function of Basement Membranes. **2007**. <https://doi.org/10.3181/0703-MR-72>.
- (117) Mak, K. M.; Mei, R. Basement Membrane Type IV Collagen and Laminin: An Overview of Their Biology and Value as Fibrosis Biomarkers of Liver Disease. *Anat. Rec.* **2017**, 300 (8), 1371–1390. <https://doi.org/10.1002/ar.23567>.
- (118) Hippocampus, C. N. S.; Zhao, C.; Toni, N.; Gage, F. H. Chapter 38 - Synaptogenesis in the Adult CNS - Hippocampus. **2013**, 2, 723–738. <https://doi.org/10.1016/B978-0-12-397266-8.00004-1>.
- (119) Baines, R. a; Seugnet, L.; Thompson, A.; Salvaterra, P. M.; Bate, M. Regulation of Synaptic Connectivity: Levels of Fasciclin II Influence Synaptic Growth in the Drosophila CNS. *J. Neurosci.* **2002**, 22 (15), 6587–6595. <https://doi.org/20026681>.
- (120) Cholas, R. H.; Hsu, H. P.; Spector, M. The Reparative Response to Cross-Linked Collagen-Based Scaffolds in a Rat Spinal Cord Gap Model. *Biomaterials* **2012**, 33 (7), 2050–2059. <https://doi.org/10.1016/j.biomaterials.2011.11.028>.
- (121) Cao, J.; Sun, C.; Zhao, H.; Xiao, Z.; Chen, B.; Gao, J.; Zheng, T.; Wu, W.; Wu, S.; Wang, J.; et al. The Use of Laminin Modified Linear Ordered Collagen Scaffolds Loaded with Laminin-Binding Ciliary Neurotrophic Factor for Sciatic Nerve Regeneration in Rats. *Biomaterials* **2011**, 32 (16), 3939–3948.

<https://doi.org/10.1016/j.biomaterials.2011.02.020>.

- (122) Yao, L.; Damodaran, G.; Nikolskaya, N.; Gorman, A. M.; Windebank, A.; Pandit, A. The Effect of Laminin Peptide Gradient in Enzymatically Cross-Linked Collagen Scaffolds on Neurite Growth. **2009**. <https://doi.org/10.1002/jbm.a.32359>.
- (123) Lein, P. J.; Higgins, D.; Turner, D. C.; Flier, L. A.; Terranova, V. P. The NC1 Domain of Type IV Collagen Promotes Axonal Growth in Sympathetic Neurons through Interaction with the $\text{A1}\beta$ 1 integrin. *J. Cell Biol.* **1991**, *113* (2), 417–428. <https://doi.org/10.1083/jcb.113.2.417>.
- (124) Zeng, Z. S.; Cohen, A. M.; Guillem, J. G. Loss of Basement Membrane Type IV Collagen Is Associated with Increased Expression of Metalloproteinases 2 and 9 (MMP-2 and MMP-9) during Human Colorectal Tumorigenesis. *Carcinogenesis* **1999**, *20* (5), 749–755. <https://doi.org/10.1093/carcin/20.5.749>.
- (125) Sashina, E. S.; Bochek, A. M.; Novoselov, N. P.; Kirichenko, D. A. Structure and Solubility of Natural Silk Fibroin. *Russ. J. Appl. Chem.* **2006**, *79* (6), 869–876. <https://doi.org/10.1134/S1070427206060012>.
- (126) Zhao, H.; Heusler, E.; Jones, G.; Li, L.; Werner, V.; Germershaus, O.; Ritzer, J.; Luehmann, T.; Meinel, L. Decoration of Silk Fibroin by Click Chemistry for Biomedical Application. *J. Struct. Biol.* **2014**, *186* (3), 420–430. <https://doi.org/10.1016/j.jsb.2014.02.009>.
- (127) Raggio, R.; Bonani, W.; Callone, E.; Dirè, S.; Gambari, L.; Grassi, F.; Motta, A. Silk Fibroin Porous Scaffolds Loaded with a Slow-Releasing Hydrogen Sulfide Agent (GYY4137) for Applications of Tissue Engineering. *ACS Biomater. Sci. Eng.* **2018**, *4* (8), 2956–2966. <https://doi.org/10.1021/acsbiomaterials.8b00212>.
- (128) Greg T. Hermanson. *Bioconjugate Techniques 2nd Edition*; 2008; Vol. 91.
- (129) Com, U. TNBSA Reagent for Amine Detection TNBSA 5% Solution. **2008**, No. 1982, 1–2.

- (130) Thermo Fisher Scientific Inc. INSTRUCTIONS TNBSA (2,4,6-Trinitrobenzene Sulfonic Acid). **2008**, 1–2.
- (131) Wang, X.; Kluge, J. A.; Leisk, G. G.; Kaplan, D. L. Sonication-Induced Gelation of Silk Fibroin for Cell Encapsulation. *Biomaterials* **2008**, 29 (8), 1054–1064.
<https://doi.org/10.1016/j.biomaterials.2007.11.003>.
- (132) R: The R Project for Statistical Computing <https://www.r-project.org/> (accessed Sep 24, 2019).
- (133) Asakura, T.; Suita, K.; Kameda, T.; Afonin, S.; Ulrich, A. S. Structural Role of Tyrosine in Bombyx Mori Silk Fibroin, Studied by Solid-State NMR and Molecular Mechanics on a Model Peptide Prepared as Silk I and II. *Magn. Reson. Chem.* **2004**, 42 (2), 258–266.
<https://doi.org/10.1002/mrc.1337>.
- (134) Venâncio, T.; Oliveira, L. M.; Pawlak, T.; Ellena, J.; Boechat, N.; Brown, S. P. The Use of Variable Temperature ¹³C Solid-State MAS NMR and GIPAW DFT Calculations to Explore the Dynamics of Diethylcarbamazine Citrate. *Magn. Reson. Chem.* **2019**, 57 (5), 200–210. <https://doi.org/10.1002/mrc.4790>.
- (135) Darsy, G.; Bouzat, F.; Muñoz, M.; Lucas, R.; Foucaud, S.; Diogo, C. C.; Babonneau, F.; Leconte, Y.; Maître, A. Monitoring a Polycycloaddition by the Combination of Dynamic Rheology and FTIR Spectroscopy. *Polymer (Guildf)*. **2015**, 79, 283–289.
<https://doi.org/10.1016/j.polymer.2015.10.030>.
- (136) Callone, E.; Dirè, S.; Hu, X.; Motta, A. Processing Influence on Molecular Assembling and Structural Conformations in Silk Fibroin: Elucidation by Solid-State NMR. *ACS Biomater. Sci. Eng.* **2016**, 2 (5), 758–767. <https://doi.org/10.1021/acsbiomaterials.5b00507>.
- (137) Tang, X.; Qiao, X.; Miller, R.; Sun, K. Effect of Ionic Strength on the Interfacial Viscoelasticity and Stability of Silk Fibroin at the Oil/Water Interface. *J. Sci. Food Agric.* **2016**, 96 (15), 4918–4928.
<https://doi.org/10.1002/jsfa.7829>.

- (138) Paquin, F.; Rivnay, J.; Salleo, A.; Stingelin, N.; Silva, C. Multi-Phase Semicrystalline Microstructures Drive Exciton Dissociation in Neat Plastic Semiconductors. *J. Mater. Chem. C* **2015**, *3* (207890), 10715–10722. <https://doi.org/10.1039/b000000x>.
- (139) Vanea, E.; Simon, V. XPS Study of Protein Adsorption onto Nanocrystalline Aluminosilicate Microparticles. *Appl. Surf. Sci.* **2011**, *257* (6), 2346–2352. <https://doi.org/10.1016/j.apsusc.2010.09.101>.
- (140) Browne, M. M.; Lubarsky, G. V.; Davidson, M. R.; Bradley, R. H. Protein Adsorption onto Polystyrene Surfaces Studied by XPS and AFM. *Surf. Sci.* **2004**, *553* (1–3), 155–167. <https://doi.org/10.1016/j.susc.2004.01.046>.
- (141) Coates, M.; Elamari, H.; Girard, C.; Griveau, S.; Nyokong, T.; Bedioui, F. 4-Azidoaniline-Based Electropolymer as a Building Block for Functionalisation of Conductive Surfaces. *J. Electroanal. Chem.* **2012**, *670*, 79–84. <https://doi.org/10.1016/j.jelechem.2012.01.001>.
- (142) Lee, H. J.; Fernandes-Cunha, G. M.; Putra, I.; Koh, W. G.; Myung, D. Tethering Growth Factors to Collagen Surfaces Using Copper-Free Click Chemistry: Surface Characterization and in Vitro Biological Response. *ACS Appl. Mater. Interfaces* **2017**, *9* (28), 23389–23399. <https://doi.org/10.1021/acsami.7b05262>.
- (143) Fortgang, P.; Tite, T.; Barnier, V.; Zehani, N.; Maddi, C.; Lagarde, F.; Loir, A.; Ja, N.; Donnet, C.; Garrelie, F.; et al. Robust Electrografting on Self-Organized 3D Graphene Electrodes. **2016**. <https://doi.org/10.1021/acsami.5b10647>.
- (144) Silva, R.; Singh, R.; Sarker, B.; Papageorgiou, D. G.; Juhasz, J. A.; Roether, J. A.; Cicha, I.; Kaschta, J.; Schubert, D. W.; Chrissafis, K.; et al. Soft-Matrices Based on Silk Fibroin and Alginate for Tissue Engineering. *Int. J. Biol. Macromol.* **2016**, *93*, 1420–1431. <https://doi.org/10.1016/j.ijbiomac.2016.04.045>.
- (145) Matsumoto, A.; Chen, J.; Collette, A. L.; Kim, U. J.; Altman, G. H.; Cebe, P.; Kaplan, D. L. Mechanisms of Silk Fibroin Sol-Gel

Transitions. *J. Phys. Chem. B* **2006**, *110* (43), 21630–21638.
<https://doi.org/10.1021/jp056350v>.

- (146) Rajabi, M.; Firouzi, M.; Hassannejad, Z.; Haririan, I.; Zahedi, P. Fabrication and Characterization of Electrospun Laminin-Functionalized Silk Fibroin/Poly(Ethylene Oxide) Nanofibrous Scaffolds for Peripheral Nerve Regeneration. *J. Biomed. Mater. Res. - Part B Appl. Biomater.* **2018**, *106* (4), 1595–1604. <https://doi.org/10.1002/jbm.b.33968>.
- (147) Asakura, T.; Suita, K.; Kameda, T.; Afonin, S.; Ulrich, A. S. Structural Role of Tyrosine in Bombyx Mori Silk Fibroin, Studied by Solid-State NMR and Molecular Mechanics on a Model Peptide Prepared as Silk I and II. *Magn. Reson. Chem.* **2004**, *42* (2), 258–266. <https://doi.org/10.1002/mrc.1337>.
- (148) Xu, Y.; Lu, Y.; Dai, X.; Dong, B. The Influence of Organic-Binding Metals on the Biogas Conversion of Sewage Sludge. *Water Res.* **2017**, *126*, 329–341. <https://doi.org/10.1016/j.watres.2017.09.046>.
- (149) Qin, Z.; Buehler, M. J. Molecular Dynamics Simulation of the α -Helix to β -Sheet Transition in Coiled Protein Filaments: Evidence for a Critical Filament Length Scale. *Phys. Rev. Lett.* **2010**, *104* (19), 1–4. <https://doi.org/10.1103/PhysRevLett.104.198304>.
- (150) Litvinov, R. I.; Faizullin, D. A.; Zuev, Y. F.; Weisel, J. W. The α -Helix to β -Sheet Transition in Stretched and Compressed Hydrated Fibrin Clots. *Biophys. J.* **2012**, *103* (5), 1020–1027. <https://doi.org/10.1016/j.bpj.2012.07.046>.
- (151) Magoshi, J.; Magoshi, Y.; Nakamura, S.; Kasai, N.; Kakudo, M. Physical Properties and Structure of Silk. Thermal Behavior of Silk Fibroin in the Random-Coil Conformation. *J Polym Sci Polym Phys Ed* **1977**, *15* (9), 1675–1683. <https://doi.org/10.1002/pol.1977.180150915>.
- (152) Motta, A.; Fambri, L.; Migliaresi, C. Regenerated Silk Fibroin Films: Thermal and Dynamic Mechanical Analysis. *Macromol. Chem. Phys.* **2002**, *203* (10–11), 1658–1665. [https://doi.org/10.1002/1521-3935\(200207\)203:10/11<1658::AID-MACP1658>3.0.CO;2-3](https://doi.org/10.1002/1521-3935(200207)203:10/11<1658::AID-MACP1658>3.0.CO;2-3).

- (153) Hu, M.; Azeloglu, E. U.; Ron, A.; Tran-Ba, K. H.; Calizo, R. C.; Tavassoly, I.; Bhattacharya, S.; Jayaraman, G.; Chen, Y.; Rabinovich, V.; et al. A Biomimetic Gelatin-Based Platform Elicits a pro-Differentiation Effect on Podocytes through Mechanotransduction. *Sci. Rep.* **2017**, *7* (February), 1–13. <https://doi.org/10.1038/srep43934>.
- (154) Zange, R.; Kissel, T. Comparative in Vitro Biocompatibility Testing of Polycyanoacrylates and Poly(D,L-Lactide-Co-Glycolide) Using Different Mouse Fibroblast (L929) Biocompatibility Test Models. *Eur. J. Pharm. Biopharm.* **1997**, *44* (2), 149–157. [https://doi.org/10.1016/S0939-6411\(97\)00082-9](https://doi.org/10.1016/S0939-6411(97)00082-9).
- (155) Haugh, M. G.; Murphy, C. M.; McKiernan, R. C.; Altenbuchner, C.; O'Brien, F. J. Crosslinking and Mechanical Properties Significantly Influence Cell Attachment, Proliferation, and Migration within Collagen Glycosaminoglycan Scaffolds. *Tissue Eng. - Part A* **2011**, *17* (9–10), 1201–1208. <https://doi.org/10.1089/ten.tea.2010.0590>.
- (156) Pina, S.; Ribeiro, V. P.; Marques, C. F.; Maia, F. R.; Silva, T. H.; Reis, R. L.; Oliveira, J. M. Regenerative Medicine Applications. *Materials (Basel)*. **2019**, *12* (11), 1824.
- (157) Manuscript, A. LAW ”: A CRITICAL REVIEW. **2010**, *31* (7), 733–741. <https://doi.org/10.1016/j.medengphy.2009.02.006.RELEVANCE>.
- (158) Tandon, B.; Blaker, J. J.; Cartmell, S. H. Piezoelectric Materials as Stimulatory Biomedical Materials and Scaffolds for Bone Repair. *Acta Biomater.* **2018**, *73*, 1–20. <https://doi.org/10.1016/j.actbio.2018.04.026>.
- (159) Yucel, T.; Cebe, P.; Kaplan, D. L. Structural Origins of Silk Piezoelectricity. *Adv. Funct. Mater.* **2011**, *21* (4), 779–785. <https://doi.org/10.1002/adfm.201002077>.
- (160) Fukada, E. Piezoelectric Properties of Biological Polymers. *Q. Rev. Biophys.* **1983**, *16* (1), 59–87. <https://doi.org/10.1017/S0033583500004923>.

- (161) Hu, X.; Shmelev, K.; Sun, L.; Gil, E. S.; Park, S. H.; Cebe, P.; Kaplan, D. L. Regulation of Silk Material Structure by Temperature-Controlled Water Vapor Annealing. *Biomacromolecules* **2011**, *12* (5), 1686–1696. <https://doi.org/10.1021/bm200062a>.
- (162) Valentini, L.; Bittolo Bon, S.; Pugno, N. M. Ice-Regenerated Flame Retardant and Robust Film of: Bombyx Mori Silk Fibroin and POSS Nano-Cages. *RSC Adv.* **2018**, *8* (17), 9063–9069. <https://doi.org/10.1039/c7ra13708g>.
- (163) Servoli, E.; Maniglio, D.; Motta, A.; Migliaresi, C. Folding and Assembly of Fibroin Driven by an AC Electric Field: Effects on Film Properties. *Macromol. Biosci.* **2008**, *8* (9), 827–835. <https://doi.org/10.1002/mabi.200800057>.
- (164) Royo-Gascon, N.; Winger, M.; Scheinbeim, J. I.; Firestein, B. L.; Craelius, W. Piezoelectric Substrates Promote Neurite Growth in Rat Spinal Cord Neurons. *Ann. Biomed. Eng.* **2013**, *41* (1), 112–122. <https://doi.org/10.1007/s10439-012-0628-y>.
- (165) Rouabhia, M.; Park, H.; Meng, S.; Derbali, H.; Zhang, Z. Electrical Stimulation Promotes Wound Healing by Enhancing Dermal Fibroblast Activity and Promoting Myofibroblast Transdifferentiation. *PLoS One* **2013**, *8* (8). <https://doi.org/10.1371/journal.pone.0071660>.
- (166) Mousavi, S. J.; Doweidar, M. H. Encapsulated Piezoelectric Nanoparticle–Hydrogel Smart Material to Remotely Regulate Cell Differentiation and Proliferation: A Finite Element Model. *Comput. Mech.* **2019**, *63* (3), 471–489. <https://doi.org/10.1007/s00466-018-1604-7>.
- (167) Zweier. 基因的改变 NIH Public Access. *Bone* **2014**, *23* (1), 1–7. <https://doi.org/10.1016/j.biomaterials.2009.04.018.Stimulation>.
- (168) Disterhoft, J. F.; Coulter, D. A.; Alkon, D. L. Conditioning-Specific Membrane Changes of Rabbit Hippocampal Neurons Measured in Vitro. *Proc. Natl. Acad. Sci. U. S. A.* **1986**, *83* (8), 2733–2737. <https://doi.org/10.1073/pnas.83.8.2733>.

- (169) Meijers, R.; Smock, R. G.; Zhang, Y.; Wang, J. H. Netrin Synergizes Signaling and Adhesion through DCC. *Trends Biochem. Sci.* **2020**, *45* (1), 6–12. <https://doi.org/10.1016/j.tibs.2019.10.005>.
- (170) Xu, Z.; Fang, P.; Xu, B.; Lu, Y.; Xiong, J.; Gao, F.; Wang, X.; Fan, J.; Shi, P. High-Throughput Three-Dimensional Chemotactic Assays Reveal Steepness-Dependent Complexity in Neuronal Sensation to Molecular Gradients. *Nat. Commun.* **2018**, *9* (1). <https://doi.org/10.1038/s41467-018-07186-x>.
- (171) Gao, M.; Lu, P.; Bednark, B.; Lynam, D.; Conner, J. M.; Sakamoto, J.; Tuszynski, M. H. Templated Agarose Scaffolds for the Support of Motor Axon Regeneration into Sites of Complete Spinal Cord Transection. *Biomaterials* **2013**, *34* (5), 1529–1536. <https://doi.org/10.1016/j.biomaterials.2012.10.070>.
- (172) Chen, W.; Zhang, Y.; Yang, S.; Sun, J.; Qiu, H.; Hu, X.; Niu, X.; Xiao, Z.; Zhao, Y.; Zhou, Y.; et al. NeuroRegen Scaffolds Combined with Autologous Bone Marrow Mononuclear Cells for the Repair of Acute Complete Spinal Cord Injury: A 3-Year Clinical Study. *Cell Transplant.* **2020**, *29*, 1–11. <https://doi.org/10.1177/0963689720950637>.
- (173) Yang, T.; Dai, Y. J.; Chen, G.; Cui, S. Sen. Dissecting the Dual Role of the Glial Scar and Scar-Forming Astrocytes in Spinal Cord Injury. *Front. Cell. Neurosci.* **2020**, *14* (April). <https://doi.org/10.3389/fncel.2020.00078>.
- (174) Linnerbauer, M.; Rothhammer, V. Protective Functions of Reactive Astrocytes Following Central Nervous System Insult. *Front. Immunol.* **2020**, *11* (September), 1–18. <https://doi.org/10.3389/fimmu.2020.573256>.
- (175) Zheng, H.; Zuo, B. Functional Silk Fibroin Hydrogels: Preparation, Properties and Applications. *J. Mater. Chem. B* **2021**, *9* (5), 1238–1258. <https://doi.org/10.1039/d0tb02099k>.
- (176) Chouhan, D.; Lohe, T. u.; Samudrala, P. K.; Mandal, B. B. In Situ Forming Injectable Silk Fibroin Hydrogel Promotes Skin Regeneration

in Full Thickness Burn Wounds. *Adv. Healthc. Mater.* **2018**, 7 (24), 1–15. <https://doi.org/10.1002/adhm.201801092>.

- (177) Kumar, M.; Gupta, P.; Bhattacharjee, S.; Nandi, S. K.; Mandal, B. B. Immunomodulatory Injectable Silk Hydrogels Maintaining Functional Islets and Promoting Anti-Inflammatory M2 Macrophage Polarization. *Biomaterials* **2018**, 187, 1–17. <https://doi.org/10.1016/j.biomaterials.2018.09.037>.
- (178) Maity, B.; Samanta, S.; Sarkar, S.; Alam, S.; Govindaraju, T. Injectable Silk Fibroin-Based Hydrogel for Sustained Insulin Delivery in Diabetic Rats. *ACS Appl. Bio Mater.* **2020**, 3 (6), 3544–3552. <https://doi.org/10.1021/acsabm.0c00152>.
- (179) Lee, K. H.; Chung, K.; Chung, J. M.; Coggeshall, R. E. Cell Body Size, Axon Size, and Signal Conduction Velocity. *J. Comp. Neurol.* **1986**, 246, 335–346.
- (180) Bahn, C. F.; Falls, H. F.; Varley, G. A.; Meyer, R. F.; Edelhauser, H. F.; Bourne, W. M. Classification of Corneal Endothelial Disorders Based on Neural Crest Origin. *Ophthalmology* **1984**, 91 (6), 558–563. [https://doi.org/10.1016/S0161-6420\(84\)34249-X](https://doi.org/10.1016/S0161-6420(84)34249-X).
- (181) Hong, L.; Shen, M.; Fang, J.; Wang, Y.; Bao, Z.; Bu, S.; Zhu, Y. Hyaluronic Acid (HA)-Based Hydrogels for Full-Thickness Wound Repairing and Skin Regeneration. *J. Mater. Sci. Mater. Med.* **2018**, 29 (9). <https://doi.org/10.1007/s10856-018-6158-x>.
- (182) Koshy, S. T.; Ferrante, T. C.; Lewin, S. A.; Mooney, D. J. Injectable, Porous, and Cell-Responsive Gelatin Cryogels. *Biomaterials* **2014**, 35 (8), 2477–2487. <https://doi.org/10.1016/j.biomaterials.2013.11.044>.
- (183) Huang, H.; Young, W.; Skaper, S.; Chen, L.; Moviglia, G.; Saberi, H.; Al-Zoubi, Z.; Sharma, H. S.; Muresanu, D.; Sharma, A.; et al. Clinical Neurorestorative Therapeutic Guidelines for Spinal Cord Injury (IANR/CANR Version 2019). *J. Orthop. Transl.* **2020**, 20 (October 2019), 14–24. <https://doi.org/10.1016/j.jot.2019.10.006>.

- (184) Santi, S.; Corridori, I.; Pugno, N. M.; Motta, A.; Migliaresi, C. Injectable Scaffold-Systems for the Regeneration of Spinal Cord: Advances of the Past Decade. *ACS Biomater. Sci. Eng.* **2021**. <https://doi.org/10.1021/acsbiomaterials.0c01779>.
- (185) Lobel, D. A.; Lee, K. H. Brain Machine Interface and Limb Reanimation Technologies: Restoring Function after Spinal Cord Injury through Development of a Bypass System. *Mayo Clin. Proc.* **2014**, *89* (5), 708–714. <https://doi.org/10.1016/j.mayocp.2014.02.003>.

Scientific Production

Santi, S.; Corridori, I.; Pugno, N. M.; Motta, A.; Migliaresi, C. Injectable Scaffold-Systems for the Regeneration of Spinal Cord: Advances of the Past Decade. *ACS Biomater. Sci. Eng.* **2021**.

<https://doi.org/10.1021/acsbiomaterials.0c01779>.

Santi, Mancini, Dirè, Callone, Speranza, Pugno, Migliaresi, Motta, A bio-inspired multi-functionalized silk fibroin (BMS). *ACS Biomater. Sci. Eng.* 2021, 7, 2, 507–516.

<https://doi.org/10.1021/acsbiomaterials.0c01567>

Participation to congresses and schools

Participation with poster presentation on the topic “synthesis of a multifunctionalized silk fibroin” to the 3rd TICME Conference 2019 Silk Conference in Trento on 12-15 June 2019

Participation with oral presentation on the topic “Piezoelectricity of a Bio-Inspired Multifunctionalized Silk Fibroin” to the tissue engineering and regenerative medicine post graduate research symposium (termsympo 2021) in Malaysia on 28th of July.

Acknowledgements

I would like to thank my supervisors, my colleagues, my friends and my family for the support. In these years, I learnt to live and work efficiently, spending the rest of the time for experiences that increased my interpersonal skills and my knowledge outside the work place. During the PhD, I met people of different cultures that have conveyed me their values, style of life and passions. I learnt that the research is 80% of failure and 20% of success at the beginning of any project. Depending on the strength of the goal the percentage of success increase, the secret has been the optimism also in the bad moments and the knowledge behind the error. I increased my creativity to solve the problems that I faced, sometimes in an unconventional way, feeling wrong. I learnt to trust on myself more than before. I understood better the future that I would like to have and the future that absolutely I will deny.

Permissions

Injectable Scaffold-Systems for the Regeneration of Spinal Cord: Advances of the Past Decade



Author: Sofia Santi, Ilaria Corridori, Nicola M. Pugno, et al
Publication: ACS Biomaterials Science & Engineering
Publisher: American Chemical Society
Date: Mar 1, 2021

Copyright © 2021, American Chemical Society

PERMISSION/LICENSE IS GRANTED FOR YOUR ORDER AT NO CHARGE

This type of permission/license, instead of the standard Terms & Conditions, is sent to you because no fee is being charged for your order. Please note the following:

- Permission is granted for your request in both print and electronic formats, and translations.
 - If figures and/or tables were requested, they may be adapted or used in part.
 - Please print this page for your records and send a copy of it to your publisher/graduate school.
 - Appropriate credit for the requested material should be given as follows: "Reprinted (adapted) with permission from (COMPLETE REFERENCE CITATION). Copyright (YEAR) American Chemical Society." Insert appropriate information in place of the capitalized words.
 - One-time permission is granted only for the use specified in your request. No additional uses are granted (such as derivative works or other editions). For any other uses, please submit a new request.
- If credit is given to another source for the material you requested, permission must be obtained from that source.

A Bio-inspired Multifunctionalized Silk Fibroin



Author: Sofia Santi, Ines Mancini, Sandra Dirè, et al
Publication: ACS Biomaterials Science & Engineering
Publisher: American Chemical Society
Date: Feb 1, 2021

Copyright © 2021, American Chemical Society

PERMISSION/LICENSE IS GRANTED FOR YOUR ORDER AT NO CHARGE

This type of permission/license, instead of the standard Terms & Conditions, is sent to you because no fee is being charged for your order. Please note the following:

- Permission is granted for your request in both print and electronic formats, and translations.
 - If figures and/or tables were requested, they may be adapted or used in part.
 - Please print this page for your records and send a copy of it to your publisher/graduate school.
 - Appropriate credit for the requested material should be given as follows: "Reprinted (adapted) with permission from (COMPLETE REFERENCE CITATION). Copyright (YEAR) American Chemical Society." Insert appropriate information in place of the capitalized words.
 - One-time permission is granted only for the use specified in your request. No additional uses are granted (such as derivative works or other editions). For any other uses, please submit a new request.
- If credit is given to another source for the material you requested, permission must be obtained from that source.